Analytical and experimental analysis of the permanent deformation after collisions

by

Hamid Ghaednia

A dissertation submitted to the Graduate Faculty of
Auburn University
in partial fulfillment of the
requirements for the Degree of
Doctor of Philosophy

Auburn, Alabama
December 16, 2017

Keywords: Contact, Collision, Permanent deformation, Oblique impact, Normal impact

Approved by

Dan B. Marghitu, Chair, Professor of Mechanical Engineering
Robert L. Jackson, Co-Chair Professor of Mechanical Engineering
Brian S. Thurow, Associate Professor of Aerospace Engineering
Joseph Ragan, Lecturer of Mechanical Engineering

Abstract

This work studied the normal and oblique impact of elastic-plastic metals. The focus of this work was to investigate the relations between the permanent deformations after the collisions and the motion of the impacting objects. The direct solution of the equations of motion during collision using various contact models have been studied.

For the first step, to predict the contact force between two elastic-plastic objects, the quasi-static contact of a hemisphere with a half space was modeled with the finite element method. More than 400 different material combinations were modeled. And for the first time in the field, a comprehensive formulation was developed to predict the contact properties of two deformable objects in contact. The results from this study were later used to directly solve the equations of motion of a round end rod normally colliding an elastic plastic flat. The impact was divided into two main phases, compression and restitution. Using this, a new expression for the permanent deformations after collision was presented. It was shown in this work that by using the experimental measurement of the permanent deformations after collision, one can predict the motion of the objects during the collision more accurately.

The same approach was taken for the direct solution of oblique impact of a round end rod with a flat. A comprehensive review of the current contact models and their implementation for oblique impact problems was done. The simulation results were compared to the experimental results for the coefficient of restitution and the permanent deformation after the collision for two impact angles. It was shown that the numerical prediction of the oblique impact matches the experimental results in terms of the motion analysis but not for the plastic deformations. The deformation results from the experiments show significantly smaller values, which implies that the normal contact force during the oblique impact should decrease in comparison to the normal collision. To address this phenomena a semi-analytical

semi-experimental model was developed that was calculating the impact duration, and the average normal force during the collision. The new model showed that the impact duration during the oblique impact increases significantly while the normal contact force is orders of magnitude larger than the numerical predictions. Finally, we showed that the permanent deformation patterns after the collision can be used to predict the impact parameters much more accurately. The permanent deformation patterns also show interesting insights about the tangential contact forces during collision that need to be studied more in the future.

Acknowledgments

I would like to acknowledge everyone who assisted me throughout my doctoral studies over the years. First I would like to thank and dedicate all my success to my parents. Their support and encouragement has always been the main reason of my success not only for this dissertation but for my whole life. Special thanks to my older brothers and sisters, Dr. Hossein Ghaednia, Dr. Aida Mollaeian, Dr. Hamed Ghaednia, Dr. Khazar Mollaeian and Dr. Keyvan Mollaeian, whom their continuous support made this dissertation possible.

I would like to acknowledge my advisor, Prof. Marghitu for his full time support and guidance, which made my graduate studies at Auburn university a very pleasant experience. I would also like to thank my co-advisor, Prof. Jackson for his enthusiastic support during my PhD studies. I would like to specially thank Dr. Carrano, and his team for their assistance with the optical profilometeries. I would like to thank my friends and lab mates who helped me through all the experiments and studies, Dr. Ozdes Cermik, Mr. Hossein Talebinezhad, Mr. Ali Khoshkhoo, Mr. Mohammad N. Ansari, Dr. Kamran Kardel, Mr. Michael Berryhill, Ms. Shahrzad Saffari, Mr. Yang Xu, Ms. Jing Zaho, Mr. Memduh Arsalan, and Mr. Ahmet Ahkan. And last but not least my committee members for all their guidance through the process.

Table of Contents

List of Figures

List of Tables

Chapter 1

Introduction and literature review

Impact is one of the most important multi scale phenomena in mechanical engineering design, tribology, robotics, bio-mechanics etc. There have been tremendous a number of studies during the last few centuries aimed at understanding and predicting the motion of the objects during collision, and the damages that are inflicted during this phenomena, the impact duration and the contact force. However, because of the complexity of a collision problem, there is no closed form solution for such a problem, and the existing effort to solve collision include several simplifying assumptions, that are basically altering the problem in the conceptual levels. Therefore, even though this problem is one of the oldest problems in the mechanical engineering, there is still a huge amount of improvements that can be implemented by the researchers to help the design engineers.

The study of free body collision started with Galileo Galilei, where refers to the collision of two falling objects as the force of precession, Galileo never solved the problem. In the seventeenth century Wallis considered the plastic deformation occurring during impact for the first time and Wren and Huygens investigated elastic impact based on the conservation of momentum. In 1687, Sir Isaac Newton defined the coefficient of restitution, e, as the ratio of the velocity after impact and the velocity before rebound in his work Principia Mathematica [85]. In 1724, Maclaurin [76] studied the collision of two rigid bodies with an elastic element in between, and divided the impact duration into two phases, compression and restitution. Poisson [87] considered the coefficient of restitution to be the ratio of the restitution and compression impulses at the contact point.

The study of collision can be probably divided into two main groups, rigid body collision, and the direct solution of the equations of motion during collision [104, 99, 103, 11, 40, 9, 10,

12]. Rigid body collision treats the collision as a mathematically discontinuous phenomena. There are several assumptions in this approach: the impact is assumed to be instantaneous, the deformations are being neglected, and the displacements during the collision have been considered to be very small and negligible. This approach leads to several contradictions when it comes to the friction forces during the collision [11, 100]. If the initial relative tangential velocities of the objects involved in the collision is high then the slip scenario will persist throughout the impact, and such a problem presents no fundamental difficulties. However, when the initial conditions of a collision problem yields to the elimination of slip during the collision, then the stick or slip reversal phenomena happens which results in the conceptual problems, such as the increase in the kinetic energy of the system, if the Newtonian coefficient of restitution to be considered. Stronge referred to the paradoxes in planar impact in 1991 [100]. He showed an increase in the kinematic energy during eccentric impact for some conditions of point contact. The example of such a problem is given by Kane and Levinson [64] for the case of the double pendulum. The central collision problems shows no such problem, stated by Stronge [99]. Mason and Wang [80] also reviewed this inconsistency, in the study of the sliding of a rod in a 2D environment. They proposed a solution based on Routh's analysis of rigid body impact, but the solution is not comprehensive, since it does not take into account the unknown bound of the kinetic coefficient, R. The main problem is coming from the misunderstanding of the traction during collision [11].

There are three definitions of restitution in rigid body impact: kinematic coefficient of restitution, e, defined by Newton (it is the most used parameter in impact mechanics), kinetic coefficient, R, defined by Poisson, and the energetic coefficient of restitution, E^2, which was the solution of Stronge to the paradox he referred to in [100]. The equations for these three parameters are:

$$e = \frac{v_{fn}}{v_{in}}, \qquad R = \frac{P_{fn}}{P_{in}}, \qquad E^2 = \frac{E_r}{E_c} \tag{1.1}$$

where, v_{fn} and v_{in} are the final and initial normal relative velocities, P_{rn} and P_{cn} are the impulses during the restitution and compression phases and the E_r and E_c are the internal energy of deformation released during the restitution and the corresponding energy gain during the compression, respectively. Stronge's definition of the energetic coefficient of restitution has two main advantages, first, the definition itself limits the coefficient to be $0 \leq E^2 \leq 1$, and second is that E^2 is independent of the tangential impulse, this is what signifies E^2 compare to e and R, which are not independent of friction force. For the special case of the central impact, one can relate the energetic coefficients to the kinetic and kinematic coefficients as $E^2 = eR$. It has to be noted here that one of the assumptions that was considered by previous studies was the independence of these coefficients to the initial normal relative velocity. This has been proven wrong many times in the more recent works [35, 39, 13, 14, 60, 20, 46, 27]. Also, these definitions were based on collision of the very hard materials such as metal to metal, which usually yields to very small impact duration (approximately 10^{-5} s), and as a result makes the assumptions of small deformation and displacements during collision acceptable to some extent. On the other hand when the collision of softer materials such as rubber are considered, these theories are not applicable as the longer impact duration (approximately 10^{-2} s) allows the relatively large displacement of the objects during the collision.

The impact of softer materials have been mostly studied for sport related objects, such as golf ball [79], soccer ball [88, 90], tennis ball [21, 44] and baseball [92]. Garwin [30] considered perfectly elastic collision of a super ball on a rigid surface. The model was very basic and did not consider the effect of friction. Later, Brody [17] studied the oblique impact of a tennis ball considering Newtonian mechanics. He did neglect the deformations on the ball and considered a constant kinematic coefficient of restitution. Brody concluded that if the angle of the impact relative to the horizontal surface is small, then the assumption of full slip is applicable; however for high friction forces and large impact angles, the ball is sliding at the beginning and then starts rolling when the relative tangential velocity at the contact

point reaches zero. The rolling then will continue until the end of the collision. Rolling here was defined as the rotation of the ball without a change in the angular velocity. The more recent works by Cross [20, 22, 23, 24, 25, 26] studies the effect of friction for the rigid body impact approach in more detail. Here we are calling these models rigid body impact since the deformations of the colliding bodies, especially the effect of deformations on the moment of inertia, have not been included in the equations of motion. One should note that the conceptual friction forces or regimes that have been interpreted in the models are based on the deformations on the objects to some extent. Cross defined the tangential coefficient of restitution, which actually helps the understanding of the slip-stick or grip phases during the collision. However, one should consider that the definition of tangential coefficient of restitution for something like a rod comparing to a sphere, adds several complexities to the problem, due to the dependency of the tangential coefficient of restitution to the size of the rod.

One of the very interesting phenomena that was seen by Cross [26] was that right before the impact ends, the angular velocity of the ball decreases. Cross could also capture the same phenomena by measuring the tangential force during collision of a tennis ball with a force plate. He saw a fluctuation in the tangential force that could result in the decrease in the angular velocity right before the impact ends for some special cases. One of the problems in Cross's measurement was neglecting the deformations of the ball during collision. Cross introduced a new mechanism, called grip during the collision, which allows the multiple reversal of the friction force direction during the impact. Unfortunately, Cross does not provide an analytical model to satisfy this behavior of the friction force and the study is mainly observational. Maw et al. [81] also studied this reversal of the friction force during collision of a sphere with a half space. While these models are studying the friction forces, the normal force has been understudied for collision of soft materials.

A majority of these studies use spring-damper equations to consider the viscoelastic behavior of the system [27, 46, 44]. The main problem with the spring damper or Kelvin-Voigt models is the paradoxes at the initiation of the contact where the contact force does not start from zero, and at the end of the impact, the contact force ends with a negative value which is logically unaccepted. Even though the spring-damper models are oversimplifying the contact between colliding objects, they have the advantage of easy integration while solving the equations of motion. The paradoxes mentioned above can be also addressed by setting the damping coefficient as a function of the deformation. This was implemented by Kardel et al. [66, 65] for modeling the behavior of 3D printed polymers under dynamic forces. It has to be noted that there are several more studies available in the field of rigid body impact that we are not mentioning here since the focus of this work is on the consideration of the deformations during collision, which is applicable for elastic-plastic materials, such as metals.

The second approach to solving a collision problem is the direct solution of the equations of motion during impact. This approach is more realistic since the deformations, displacements and impact duration have not been neglected in the solution, and yields to a more realistic prediction of such a problem, but also adds much complexity to the problem. It is obvious that the contact force during collision is the most important factor in such a solution as the integration of the equations of motion depends highly on the contact force. Therefore using an accurate contact model is of a significant importance. In the next part of this chapter we focus on the development of these contact models mainly for metals.

Concepts of contact mechanics are critically important and implemented towards a wide variety of applications in different length scales [63, 105, 52]. For instance, consider the applications in the rubber industry and contact of proteins [96] in large and small scales, respectively. The mathematical formulation of contact mechanics is constructed upon continuum mechanics in the context of both linear and nonlinear theories of elasticity. Even though the analytical studies on the nonlinear contact of solids is limited due to the complexity of

the problem, some recent developments using non-trivial reference configurations to study the induced residual stresses in nonlinear solids are addressing some of these complexities [41, 43, 42].

Contact mechanics is considered as one of the most important elements of tribology, from the nano-scale to macro-scale. It is critically important in bearings [36], electrical contacts [38], gears, tires road contact, biomechanical systems, impact mechanics [77, 31, 35, 34, 39, 66, 60, 13, 14], joint structure, nano lubrication [32, 33], and rough surface contact [119, 120, 118, 125, 94, 113, 19, 124, 61, 117]. There are only 4 review papers published in this field that are at least 16 years old, but still are great sources of the progress in the field [1, 4, 6, 7]. The most related review paper to this study is presented by Bhushan [6], which focuses on the single asperity contact. Bhushan [7] also published a review paper on the elastic-plastic rough surface contact. Other two reviews by Barber and Ciavarella [4], and Adam and Nosonovsky [1] are concentrated on the contact with friction, and adhesion. In this study we focus on the single asperity frictionless contact, which is probably the most conceptual problem in contact mechanics. The reason being that for macro scale problems in which the elastic-plastic deformations of the objects is much larger than the roughness of the contacting surfaces (such as majority of the impact problems), the single asperity contact can be directly used in the simulations.

1.1 Elastic contact

The contact of bodies can be divided into the elastic, elastic-plastic and perfectly plastic phases. For the elastic contact of two spheres a closed form analytical solution is provided by Hertz [48], which aroused considerable interest during the past century. In the Hertzian theory the spherical surfaces have been approximated by a parabola. The pressure distribution that satisfied the displacements in contact proposed as:

$$p = p_0 \left[1 - \left(\frac{r}{a}\right)^2\right]^{1/2} \tag{1.2}$$

where p_0 is the maximum pressure in the contact area, r is the radial distance from the center of the contact area and a is the radius of the contact area. This yields the following displacement field on each of the spheres:

$$u_z = \frac{1-\nu^2}{E}\frac{\pi p_0}{4a}(2a^2 - r^2), \qquad r \leq a \tag{1.3}$$

finally by using the boundary conditions [63] and the proposed stress distribution Eq. (4.1) the contact characteristic can be formulated as:

$$a = \left(\frac{3PR}{4E^*}\right)^{1/3} \tag{1.4}$$

$$\delta = \left(\frac{9P^2}{16RE^{*2}}\right)^{1/3} \tag{1.5}$$

$$p_0 = \frac{3P}{2\pi a^2} \tag{1.6}$$

where E' and R are:

$$E'^{-1} = \frac{1-\nu_1^2}{E_1} + \frac{1-\nu_2^2}{E_2}, \tag{1.7}$$

$$R^{-1} = \frac{1}{R_1} + \frac{1}{R_2} \tag{1.8}$$

Hertzian theory [48] can be used for elastic contacts, but in most cases, specially for metals, the materials reach the yield stress during a contact. When the contact force reaches a critical value, the stress state will start to cause yielding within the sphere and the elastic-plastic phase will start until the contact reaches the fully plastic phase. Since the fully plastic regime is the other limit of the elastic-plastic phase, it will be examined next.

1.2 Fully plastic contact

The contact reaches the fully plastic regime at high loads when the whole contact area reaches plastic deformation. For the fully plastic contact the analytical solution is only

possible with simplifying assumptions, such as neglecting the effect of sink-in and pile-up. The contact at this point should be divided into two groups based on the material properties. Jackson and Kogut [58] categorized the contact into flattening and indentation groups, in which flattening refers to the contact of a deformable sphere with a flat and the indentation group considers the indentation of a deformable flat by a rigid sphere. Recently Ghaednia et al. [37] studied the elastic-plastic contact of a sphere and a flat, where they considered the deformation on both objects. They provide a comprehensive formulation that predicts the transition between these two groups. The details of their model is presented in Chapter 2 of this study. Olsson and Larsson [86] also studied the contact of two dissimilar elastic-plastic spheres with different material properties. They mostly concentrated on the effect of the radius of curvature on the contact properties.

The indentation of a flat by a hemisphere (Fig. 1.1) has been studied by many researchers for over a century [63, 37, 13, 14, 71, 122, 72, 73, 74, 3, 2, 8, 82, 91, 105, 106, 107, 123, 89, 110, 127, 126, 127, 111, 112, 115]. In Fig. 1.1, δ is the penetration, a is the real contact radius, a' is the radius of truncated contact area, which ideally would be equal to the real contact area if no pile-up and sink-in was happening around the contact region, and R is the radius of the sphere. In the reality however, there is no ideally rigid body and therefore there is a need for a criteria in which the contact can be approximately defined as indentation. Tabor showed [105] that if the yield strength of the sphere is more than 2.5 times the yield strength of the flat, the deformations on the sphere will be elastic for a normal hardness test, and this deformation does not affect the test significantly. Recently, Rodriguez et al. [93] showed that elastic deformations on the sphere can cause up to 12 % error in the measurements. It has also been verified by Ghaednia et al. [37] that if the yield strength of the sphere is 1.7 times larger than the yield strength of the flat, the contact can be specified as indentation.

The study of indentation contact initiated to develop models for the Brinell [15] and Meyer [84] hardness tests. In 1900, Brinell [15] developed a new hardness test in order to determine the properties of materials. Later in 1908, Meyer [84] studied the different hardness

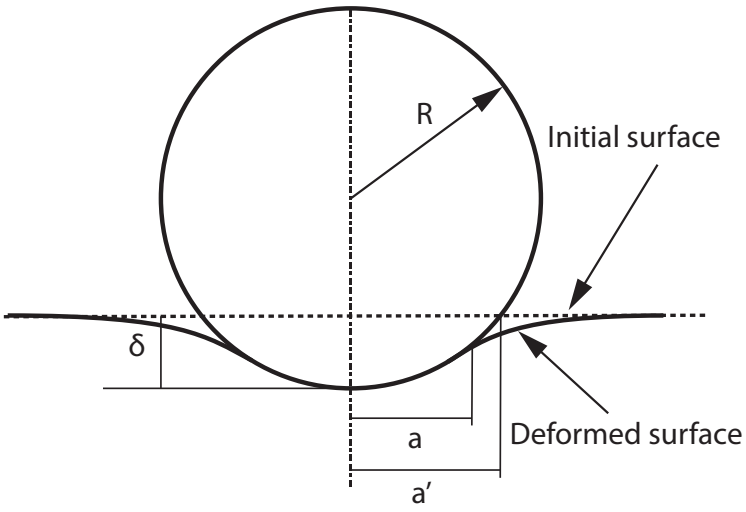

Figure 1.1: In the indentation models the sphere is rigid and the flat is deforming.

tests and defined the Meyer hardness. In 1948, Tabor [105] introduced the simple theory of static and dynamic hardness. Later in [106], he performed a vast number of experiments on the hardness of metals. Tabor's work is probably one of the best references for many mechanical indentation applications to this day [49].

The average pressure, $\bar{p}$, is defined by Meyer as the contact force divided by the projected area of contact in the direction of the indentation, $F/\pi a^2$, where F is the contact force and a is the radius of contact. Alternatively Brinell suggested that hardness to be the contact force divided by the total surface area of the contact.

Conventionally from the experimental results of Brinell test by Tabor, the popular value of $\bar{p}/S_y = 2.84$ was accepted for the average normal pressure or hardness of fully plastic contacts without the strain hardening. To reduce the effect of strain hardening to the minimum, Tabor used work hardened materials in all of his tests. In 1944, Ishlinskii [50] provided a new way of drawing the slip lines that helped to provide an analytical model for the contact of a rigid sphere and a fully plastic flat. This was also verified theoretically by Ishlinskii [50] that the hardness value varies between 2.61 and 2.84 and does not significantly depend on the indentation depth. This however has been shown in the recent studies not to be correct.

Based on the work of Ye and Komvopoulos [122], Kogut and Komvopoulos [71] showed that the average pressure in an elastic-plastic contact reaches a maximum value that is less than $2.84S_y$. They studied the dependence of the maximum average pressure on the material properties. The following formula was proposed:

$$\frac{\bar{p}}{S_y} = 0.201 \ln\left(\frac{E'}{S_y}\right) + 1.685 \tag{1.9}$$

where E' is the reduced or effective modulus of elasticity.

On the other hand, the study of indentation of a rigid body on an elastic-plastic flat with and without strain hardening by Mesarovic and Fleck [82] showed that as the indentation increases the average pressure decreases from the Tabor's value, $2.84S_y$. The effect of strain hardening also was shown to counter this effect in some cases. This was probably the first observation of this effect. Later Yu and Blanchard [123] presented the same effect and provided the following equation:

$$\frac{\bar{p}}{S_y} = \frac{2}{\sqrt{3}}\left(2.845 - 0.4921\,\frac{a}{R}\right) \tag{1.10}$$

Alcala and Esque-de los Ojos [2] also studied the similar effect for indentation without strain hardening. They provided the following equation:

$$\frac{\bar{p}}{S_y} = 3.044 - 1.885\,\frac{a}{R} \tag{1.11}$$

A recent paper by Olsson and Larsson [86] also captures the variation of the normal average pressure in the fully plastic regime by fitting the finite element results from [82]:

$$\frac{\bar{p}}{S_y} = 3\left[1 - 0.0461\left\{\ln\left(\frac{a}{R}\right) - \ln(LD)\right\}^{2.214}\right] \tag{1.12}$$

Recently, Jackson et al. [53] presented an analytical solution based on the slip-line theory and calculated the relation between the average pressure and the radius of contact

for the indentation of a perfectly plastic flat by a rigid sphere. Jackson et al. [53] presented the following equation for the average pressure or the hardness during an indentation contact:

$$\frac{\bar{p}}{S_y} = \frac{4}{3\sqrt{3}} \left(\frac{a}{R}\right)^{-2} \left[\frac{1}{3}\left(\frac{a}{R}\right)^{3} - \left(1 + \cos^{-1}\left(\frac{a}{R}\right)\right)\left(1 - \left(\frac{a}{R}\right)^{2}\right)^{3/2} - \frac{a}{R} + \frac{\pi}{2} + 1\right] \tag{1.13}$$

The comparison of Eqs. (1.10, 1.11, 1.12, 1.13) with FEM is shown in Fig. 1.2. All of these equations are developed for indentation contact. It has to be noted that the FEM results in Fig. 1.2 are not representing a perfectly plastic material, but are close to a fully plastic case.

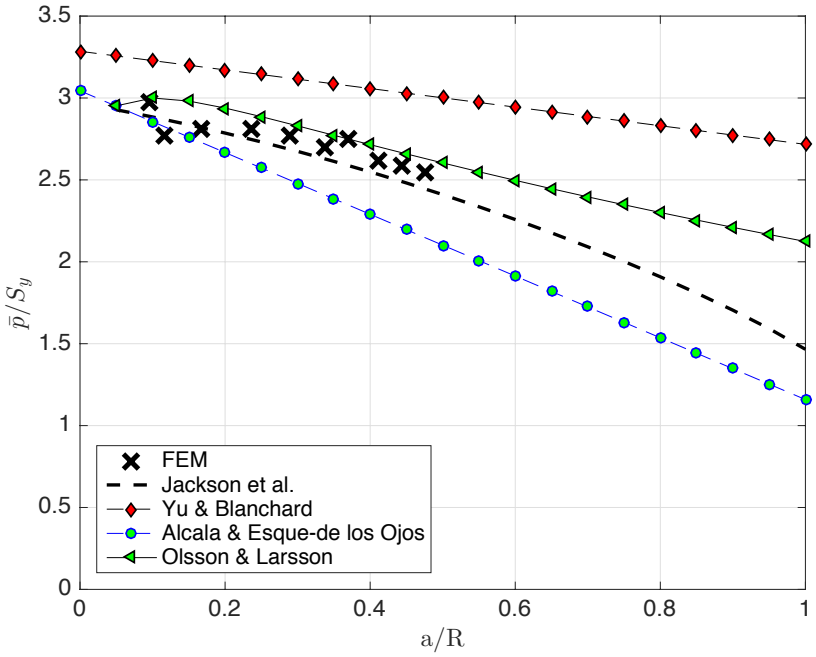

Figure 1.2: Comparison between Eqs. (1.10, 1.11, 1.12, 1.13) and FEM results for indentation models.

Jackson and Green [54] showed that this is correct for flattening cases as well. They proposed the following equation for the hardness in the fully plastic regime:

$$\frac{\bar{p}}{S_y} = 2.84\left[1 - \exp\left\{-0.82\left(\frac{a}{R}\right)^{-0.7}\right\}\right] \tag{1.14}$$

Later they presented an improved fit , [60]:

$$\frac{\bar{p}}{S_y} = 2.84 - 0.92\left[1 - \cos(\pi\frac{a}{R})\right] \tag{1.15}$$

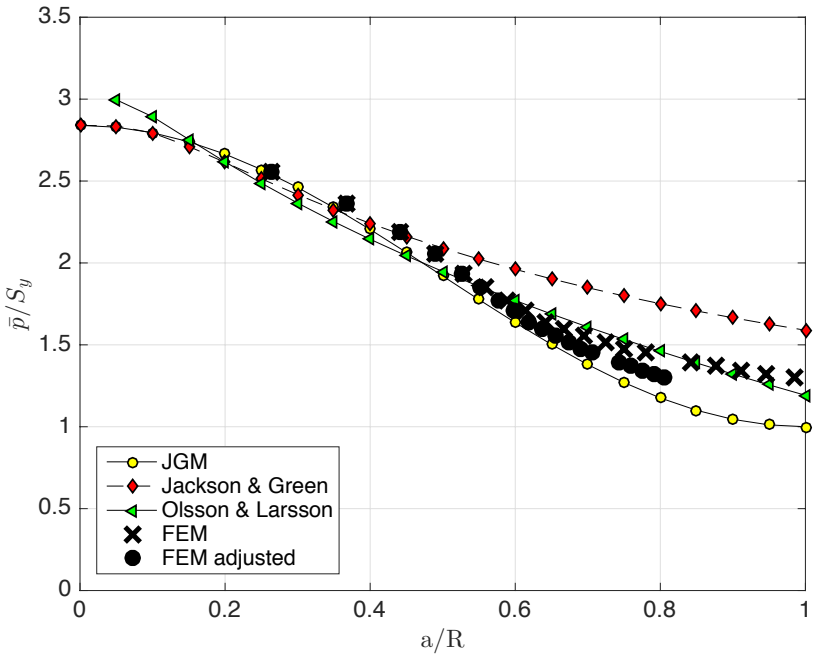

Figure 1.3: Comparison between Eqs. (1.12, 1.14, 1.15) and FEM results for flattening contact.

In Fig. 1.3 the adjusted FEM results show the modified results for radius of curvature. Equation (1.15) is one of the biggest difference between Jackson and Green's model with the previous models, it shows that the hardness or the average normal pressure decreases as the contact radius increases. As the sphere deforms, it changes shape. The original curved contact morphs towards a cylindrical column in contact with a flat. As this transition occurs, the average pressure for fully plastic contact changes from a value of approximately $2.84\,S_{ys}$ as found by Tabor [105], to unity times S_{ys}. The effectiveness of these equations was further confirmed for a wider range of materials by Quicksall et al. [89].

Note that the Jackson and Green [54] equations are only valid up to $a/R = 0.41$. However, Wadwalkar et al. [110] also used finite elements to find a model that is valid for much larger loads and deformations until the contact radius nearly equals the radius of the sphere. Sahoo also [95] studied the effect of E'/S_y on the contact. Note that in these cases of severe deformation, the sphere actually begins to behave similarly to a barreling cylinder in compression.

1.3 Elastic-plastic contact

The elastic-plastic zone starts at the initiation of yielding, where the maximum von misses stress reaches the yield strength. Several models such as [70, 71, 122] considers the elastic plastic exactly at the initiation of yield, when interference is δ_c. Jackson and Green [55] showed that even though the yielding starts at the critical interference, the contact area and the contact force starts to deviate from the elastic solution when the interference is 1.9 times larger than the critical interference, $\delta = 1.9\,\delta_c$.

Although, there have been many efforts to provide an analytical solution for the elastic-plastic regime, non of the presented models are able to capture the complexity of an elastic-plastic contact. For the elastic-plastic regime to simplify the problem most of the models study the contact between a sphere and a flat. Later many studies implemented finite element analysis (FEA) to observe, and formulate the behavior of contact in the elastic-plastic regime, starting with the works of Sinclair and Follansbee [29, 98]

The first elastic-plastic contact model was proposed by Chang et al. [18] referred to as CEB model. In CEB model, the sphere remains elastic up to a critical interference. For larger interferences, the model imposes the volume conservation of the sphere. The CEB model has a discontinuity in the contact force and the first derivation of both the contact force and the contact area.

A majority of the studies for elastic-plastic contact use finite element analysis to model, simulate and formulate description of the contact. In the following subsections some of the famous contact models have been reviewed in two groups, flattening, and indentation.

1.3.1 Indentation models

In 1985, Johnson [63] developed a contact model for a spherical contact now referred to as the simple plastic contact. In Johnson's model, the contact is divided into two phases: the fully elastic phase and the fully plastic phase. The fully elastic phase has been considered to follow the Hertzian theory, and in the fully plastic phase the hardness is considered to be $H = 2.8\, S_y$. Johnson verified this model with Tabor's [106] work.

In 1967 and 1971, Zienkiewicz [128, 129] presented the triangular ring element for FEM analysis of an axi-symmetric problems, which was used by Yamada [121] to solve elastic-plastic problems numerically. In 1971, Hardy [47] started to analyze the indentation problem with FEM methods. He investigated the elastic-plastic indentation; however, he did not provide any formulation for the contact force. Sinclair [98] and Follansbee [29] did the same finite element analysis for the indentation problem with a better meshing. Their results were compared with Tabor's [106] experiments, Ishlinskii's theory [50] and Richmond's adhesive slip-line theory [91].

Sinclair and Follansbee [98, 29] also provided empirical formulations for their finite element analysis. In their work, the elastic phase follows the Hertzian theory and is dominate for $\bar{p}/S_{yf} \leq 1.1$, where S_{yf} is the yield strength of the flat. They considered hardness to be, $H = 2.8\, S_{yf}$, and that the fully plastic phase starts at $a\, E'/R\, S_{yf} = 50$. The normalization used in their work for the real radius of contact was given by Johnson et al. [63]. This was probably the first study in contact mechanics that developed an empirical formulation based on the FEM analysis.

Later, Komvopoulos [72, 73] used FEA modeling in order to analyze the indentation of a rigid sphere in a layered flat. Even though, the work was for the contact of a sphere with a layered material, he also developed a formulation for a single asperity contact.

Even with the development of computers allowing accurate FEA modeling to perform, still there were many assumptions such as neglecting the effect of hardening, pile-up, sink-in and friction. Mesarovic et al. [83] did a comprehensive study on the effect of strain hardening, friction and pre-existing stress. They showed that friction can affect the stress distribution, contact force and contact area. However, no formulation was provided for predicting the effect of the studied parameters.

Komvopoulos and Ye [122, 74] developed a new formulation for the indentation of homogeneous and layered materials. They used a different normalization than Johnson [63]. In the KY model [71] contact is divided into four different sub-phases: the elastic phase, small deformations, medium deformations, and large deformations.

Later, Kogut and Komvopolous [71] improved the last model and gave a new formulation for the indentation of a homogeneous flat. They provided formulations for the loading and unloading phases. The same normalization as [122, 74] was used for the deformation. Later, Bartier et al. [5] presented a comparison between the analytical models for the real contact radius.

Next, in 2012 Brake [13] developed a new semi-analytical model. The contact was divided into three phases, elastic, elastic-plastic, and fully plastic phases. The fully elastic phase follows the Hertz theory, and the fully plastic phase follows Johnson's theory. For the elasto-plastic phase, Brake fitted a third-order polynomial interpolation between the fully elastic and the fully plastic phases. The model was impelemented for the impact of a sphere with a flat and verified with the experiments presented by Kharaz's [68, 67]. In a more recent work [14], Brake used the same methodology with different transition functions from the elastic phase to the plastic phase of the contact. The formulation for the fully plastic phase uses the Meyer hardness exponent. Brake also considered the frictional contact for the

oblique impact case. This model shows an improvement over the previous model presented by Brake [13].

1.3.2 Flattening models

Flattening refers to the contact of a deformable sphere with a rigid flat, Fig. 1.4. Figure 1.4 shows the contact of an elastic-plastic sphere with a rigid flat, where δ is the relative normal displacement between the sphere and the flat and a is the real radius of contact. In

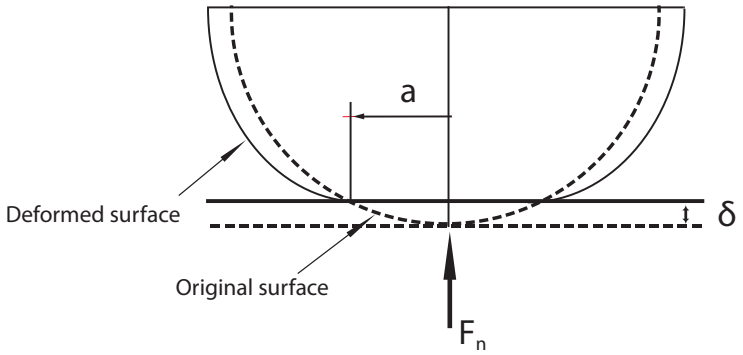

Figure 1.4: In the flattening models the flat is rigid and the sphere is deforming.

1968, Johnson [62] investigated the fully plastic contact between spheres and cylinders experimentally; however the elastic-plastic contact had to wait another decade to be studied. Over the past 30 years, many models have been devised to account for the plastic deformation in the sphere. Most of the models consider the material to be the elastic-perfectly plastic and do not consider the effect of the strain hardening. Even for this simplified case, there is no known analytical solution to this date.

Later, by using the finite element method Li and Thornton [75], Wu et al. [116], Kogut and Etsion [69] and Jackson and Green [54] improved upon previous models such as the ground breaking study by Chang et al. [18]. In 2002 Li and Thornton [75] worked on a theoretical model for the normal contact force between elastic-plastic bodies. They modified Thornton's [109, 108] contact models with a more accurate pressure distribution based on FEM analysis.

Kogut and Etsion [69] presented a new empirical formulation for elastic-plastic contact of a hemisphere and a rigid flat. The material was considered elastic-perfectly plastic and the contact was divided into elastic and elastic-plastic phases during the loading. The elastic phase follows the Hertzian theory and was defined as $\delta/\delta_c \leq 1$, where δ and δ_c are the deformation and the critical deformation (the deformation in which yielding first occurs), respectively. The elastic-plastic phase has been divided into three sub-phases: $1 < \delta/\delta_c \leq 6$, $6 < \delta/\delta_c \leq 68$ and $68 < \delta/\delta_c$. For the elastic-plastic phase, an empirical formulation has been provided from the curve fitting of the FEM results. The simple presented formulation in their work causes an inaccuracy in the prediction of large deformations. Later Wang [114] improved the formulation of Kogut and Etsion specially for the unloading phase that was presented in [28].

In 2005, Jackson and Green [54] developed a new model for the contact between an elastic-plastic half sphere and a rigid flat. They provided equations for the prediction of initial yielding in the sphere according to the Von Mises yield criteria:

$$\delta_c = \left(\frac{\pi\, C\, S_{ys}}{2E'}\right)^2 R, \tag{1.16}$$

where δ_c is the critical value in which the yield occurs, S_{ys} is the yield strength of the sphere, E' is the reduced modulus of elasticity defined by Hertz [48] and C can be found from the following:

$$C = 1.295\, e^{0.73\nu_s}, \tag{1.17}$$

where ν_s is the Poisson's ratio of the sphere. Note that C is actually a fit to the theoretical predictions but has the same exponential form as its analytically derived counterpart equation for sinusoidal contact [59]. Even though Eq. (1.16) was verified for a flattening case, it should be applicable for the indentation cases as well. Using the critical deformation, the

critical area and the critical contact force are defined as:

$$A_c = \pi^3 \left(\frac{C\, S_{ys}\, R}{2\, E'} \right) \tag{1.18}$$

$$F_c = \frac{4}{3} \left(\frac{R}{E'} \right)^2 \left(\frac{C}{2} \pi\, S_{ys} \right) \tag{1.19}$$

These critical values have been used in the model to normalize the formulation for the elastic-plastic phase. Later, Shankar and Mayuram [97] studied the transition to the elastic-plastic phase based on the evolution of the elastic core. Note that Jackson and Green [56] suggested that the yield strength of the weaker material could be used in the contact of two deformable surfaces. Green [45] also suggested that C of the weaker material can be used.

In the model by Jackson and Green, the elastic phase effectively is defined as $\delta/\delta_c \leq 1.9$, in which the Hertzian theory can be used. However, once the plastic deformation is significant, the following equations fit to the FEM results can be used for the force:

$$\frac{F}{F_c} = \left[e^{\left(-0.25(\delta/\delta_c)^{0.416}\right)} \right] \left(\frac{\delta}{\delta_c} \right)^{1.5} + \frac{4\,\bar{p}}{C\, S_{ys}} \left[1 - e^{\left(-0.04(\delta/\delta_c)^{0.55}\right)} \right] \left(\frac{\delta}{\delta_c} \right) \tag{1.20}$$

where $\bar{p}/S_y$ is found from Eq. (1.15), and the contact area:

$$\frac{A}{A_c} = \frac{\delta}{\delta_c} \left(\frac{\delta}{1.9\, \delta_c} \right)^B \tag{1.21}$$

where B can be calculated as:

$$B = 0.14\, e^{23\, S_{ys}/E'} \tag{1.22}$$

All of the above works only considered a deformable sphere loaded against a frictionless rigid flat surface. Etsion's research group has also studied the effect of the slip conditions between the surfaces on the normal contact [16, 70].

1.4 Contact mechanics in the study of impact

Contact models have been used in many impact applications. Stronge used Johnson's [63] elastic-fully plastic model where he defined a new energetic coefficient of restitution [99]. Stronge divided the impact into three phases: the fully elastic, the fully plastic, and the restitution [99, 101, 102, 104, 100]. The elastic phase follows the Hertzian theory [48]. The fully plastic phase follows Johnson's expression [63]. The restitution is considered to be fully elastic and follows the Hertzian theory.

Thornton [109] developed a numerical model to study the impact of a sphere with a wall. He also studied elastic-perfectly plastic impact and provided an analytical solution to a simplified model [108]. The restitution phase follows the Hertzian theory. However, Thornton assumes that the radius of curvature for this phase is larger than the radius of curvature for the loading phase.

In 1999 and 2000, Kharaz et al. performed a new accurate experimental study on the impact of 5 mm aluminum balls with a massive steel surface [68],[67]. They used computer vision in order to measure the motion. Jackson et al. [57] studied the impact of an elasto-plastic sphere with a rigid flat and used the Jackson and Green contact model in order to predict the coefficient of restitution after the impact. They compared and verified their results with Kharaz's experiments. Marghitu et al. [78] applied the Jackson-Green contact model for the impact of a rotating link with a massive surface. Brake used his contact models [13, 14] for the normal and oblique impacts in order to compare and verify his results with Kharaz's experiments. It has to be considered that Kharaz experiments performed with 5 mm diameter aluminum balls and did not result in large deformations. Therefore, comparing the results with Kharaz's experiments might result in some inaccuracies.

In this study we tried to relate the permanent deformations after collision to the motion of the colliding object during impact of two elastic-plastic materials. The study can be divided into four main steps: formulation of the contact force, prediction of the permanent

deformation for normal collision, verification of the models for oblique impact, and a new semi analytical model that predicts the average contact force and the impact duration.

For the first step, a new comprehensive model for the elastic-plastic contact of two deformable objects is developed. We studied more than 400 different material properties, and defined a new parameter to the field, as the yield strength ratio, S_y^*. The impact was divided into two main phases, compression and restitution. The developed contact model was later used to solve the equations of motion during the compression phase of a normal collision of a round ended rod with an elastic-plastic flat. For the restitution phase, a new permanent deformation expression was developed based on the experimental results. It was verified in this step that the permanent deformations can be used to predict the dynamic of collision accurately.

The same approach was taken for the oblique impact of a round end rod with a flat. Comparison with the experiments showed that majority of the contact models match the results for coefficient of restitution. However, in the case of permanent deformations, the numerical simulations are orders of magnitude different from the experimental results. To address this issue a semi-analytical semi-experimental model was developed that predicts the impact duration, and the average normal force during the collision. The new model showed that the impact duration during the oblique impact increases significantly while the normal contact force is orders of magnitude larger than the numerical predictions. Finally we showed that the permanent deformation patterns after the collision can be used to predict the impact parameters much more accurately. In following chapters the details about each step have been explained in each chapter.

Chapter 2

Finite element modeling of elastic-plastic contact of two deformable objects

In this work the frictionless contact of an elastic-plastic sphere with an elastic-plastic flat has been studied. Previously, elastic-plastic contact has been mostly studied either for the isolated flattening or indentation cases. This work analyzes the case in between these, where both surfaces deform elastic-plastically. It has been shown that the deformation on both objects has a significant effect on the real area of contact and the contact force. The ratio between the yield strength of the sphere and the flat has been defined as a major governing factor, and is called yield strength ratio, S_y^*. The deformations on both of the objects and their effects on the real area of contact and the contact force have been analyzed. It has been shown that for the case in which both of the objects have the same yield strength, the real area of contact and the contact force decrease significantly. Finite element analysis has been performed for more than 400 cases, and a comprehensive formulation has been developed based on the FEM results in order to predict the deformation of each object, the real area of contact, hardness (the average pressure for fully plastic contact) and the contact force. The new formulation has been compared with previous contact models, reviewed in chapter 1, for indentation and flattening cases. The details of FE modeling, curve fitting and the formulation will be discussed in this chapter.

2.1 Modeling

The problem has been simulated as an axi-symmetric, elastic-plastic frictionless contact of a half sphere and a half space. The materials have been modeled as elastic-perfectly plastic with no strain hardening. A finer mesh around the contact point has been applied, Fig. 2.1. A mesh convergence has been performed both for small and large deformations to verify

the model for elastic and plastic contacts respectively. Finally, a mesh consisting of a total number of 9784 9-node elements has been chosen. The force has been applied as a constant displacement on the top edge of the half-sphere. The FEM has been done for more than 800 cases, and the results have been analyzed for the deformations of both objects, the real radius of contact, hardness and the contact force. The deformation on the sphere is measured by subtracting the displacement of the tip node from the applied displacement. Deformation of the flat is the applied displacement minus the sphere deformation. Real contact radius has been measured from final position of the furthest node in contact. The contact force is measured from the reaction force on all of the top edge nodes in the Y direction. The hardness is the contact force divided by the projected real contact area.

It has to be noted that the assumption of the frictionless contact that has been used here as well as many previous studies in this field, can cause inaccuracies in the results for real area of contact. Even though, the friction force can effect the sink-in or pile-ups, this parameter has been neglected in majority of the contact models. Another problem with consideration of friction force is the complexities in the implementation of friction force in the contact elements. In the following subsections, short discussions on the FEM results have been presented.

2.2 Modeling results

In most of the contact models the contact is categorized as either indentation or flattening, therefore the minimum yield strength, $S_{y\,min}$, is enough to analyze the results. In this study both of the materials can undergo plastic deformations, hence the yield strength of both of the materials are important. Before explaining the FEM results, we need to define a new parameter to be able to present and compare the results. The yield strength ratio, S_y^*, is defined as the ratio between the yield strengths of the sphere and of the flat:

$$S_y^* = \frac{S_{ys}}{S_{yf}} \tag{2.1}$$

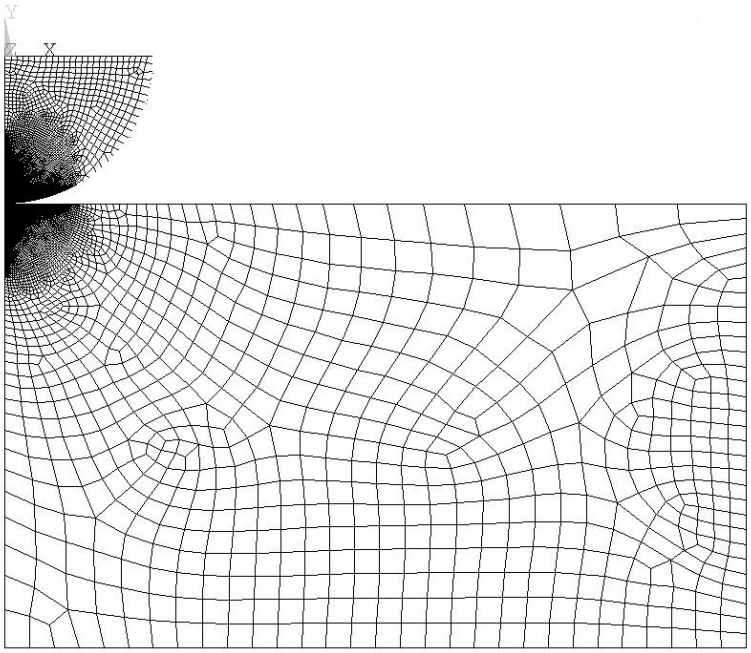

Figure 2.1: Final mesh used in the finite element analysis.

where S_{ys} and S_{yf} are the yield strengths of the sphere and the flat respectively. At $S_y^* = 0$ the contact is ideally flattening, for $S_y^* = \infty$ the contact can be considered as indentation and at $S_y^* = 1$ both of the materials are the same. In this section the modeling results has been presented. The stress distribution patterns has been depicted for three different cases with similar minimum yield strength, and different yield stress ratio to show the differences between the flattening and indentation models. The numerical results have been presented for deformation on both objects, real contact radius, hardness, and contact force. For all numerical results five different cases have been studies. Table 2.1 shows the material properties for all five cases. It has to be considered that for each case the yield strength ratio is changing from $S_y^* = 0.1$ to $S_y^* = 10$. For each case, $S_{y\,min}$ is the same for the flattening and the indentation parts of the graphs. This means that $S_{y\,min} = S_{ys}$ in $S_y^* < 1$ is equal to $S_{y\,min} = S_{yf}$ in $S_y^* > 1$.

Table 2.1: Material property cases for results.

	Case 1	Case 2	Case 3	Case 4	Case 5
E_s(GPa)	200	200	71.7	71.7	200
E_f(GPa)	200	200	200	200	200
$S_{y,min}$(MPa)	200	300	300	503	503
ν_s	0.3	0.33	0.33	0.3	0.33
ν_f	0.3	0.3	0.3	0.3	0.3

2.2.1 Stress distribution

Deformation on both objects affects the stress distribution pattern. Fig. 2.2, 2.3, and 2.4 show the Von-mises stress distributions for three cases. All of these cases have the same minimum yield strength, $S_{y\,min}$, which means that for the flattening and the indentation models, the sphere and the flat have the same yield strength respectively. The same load (displacement) has been applied on the sphere for all three cases.

Figure 2.2 shows the case for $S_{ys} = 503$ MPa and $S_{yf} = 5030$ MPa, where the S_{ys} and S_{yf} are the yield strength of the sphere and the flat, respectively. The modulus of elasticity and the Poisson's ratio are 200 GPa and 0.3 for both of the objects. This case is closer to the flattening models; however, as can be seen, the maximum stresses reach the surface on the flat at the last point of contact. The flat is still in the elastic phase because of the large difference between the yield strength of the flat and the sphere.

Figure 2.3 shows the case in which both the flat and the sphere have the same material properties ($S_y = 503$ MPa, $E = 200$ GPa and $\nu = 0.3$). Here, the maximum stress region reaches the surface over the whole contact area, and a large portion of both the flat and the sphere reach the plastic deformation.

Figure 2.4 shows the case for $S_{ys} = 5030$ MPa and $S_{yf} = 503$ MPa. The modulus of elasticity and the Poisson's ratio are 200 GPa and 0.3 for both of the objects. This case is close to the indentation models. The stress is significant around the last point in contact, and the flat reaches yield even outside of the contact area. The sphere has not reached

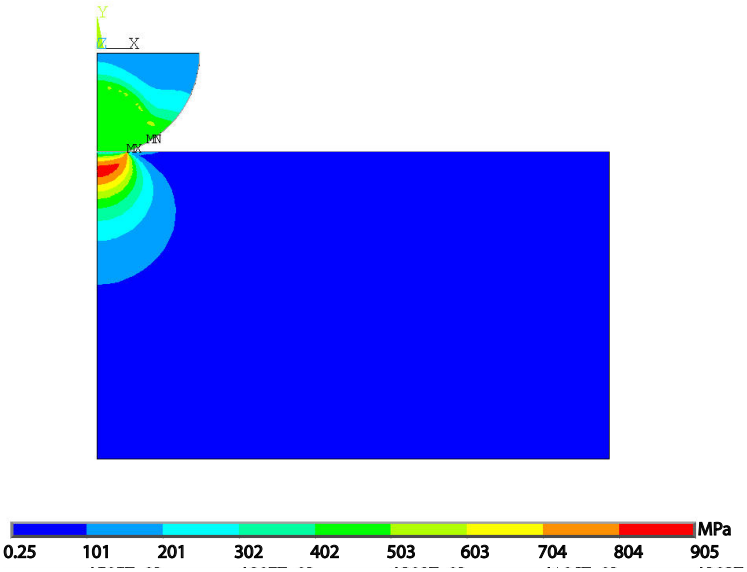

Figure 2.2: Von mises stress distribution for $S_y^* = 0.1$, $S_{y\,min} = 503$ MPa, $E = 200$ GPa, and $\nu = 0.3$.

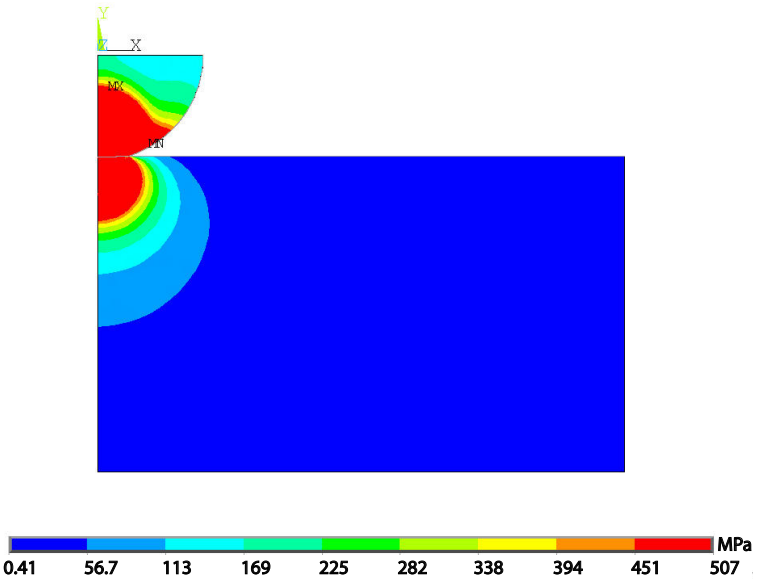

Figure 2.3: Von mises stress distribution for $S_y^* = 1$, $S_{y\,min} = 503$ MPa, $E = 200$ GPa, and $\nu = 0.3$.

yield yet and acts as a fully elastic material because of the large difference between the yield strengths of the sphere and the flat.

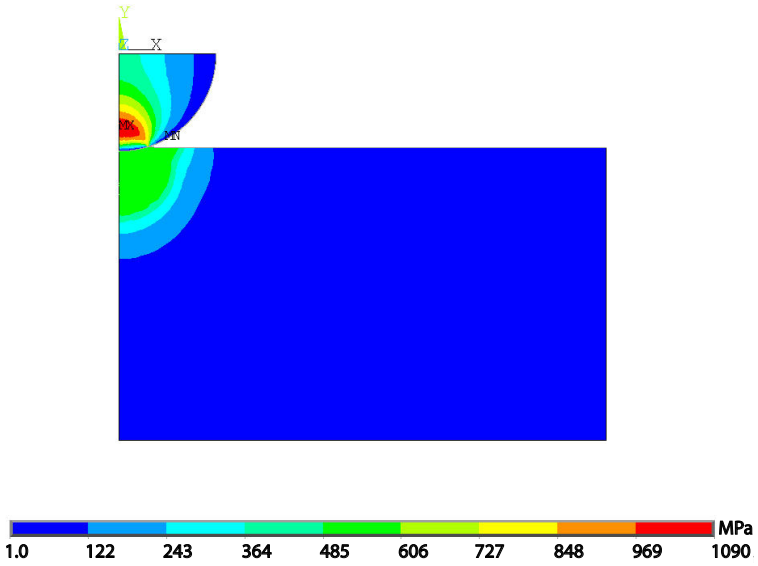

Figure 2.4: Von mises stress distribution for $S_y^* = 10$, $S_{y\,min} = 503$ MPa, $E = 200$ GPa, and $\nu = 0.3$.

2.2.2 Deformation

The minimum yield strength, $S_{y\,min}$, is defined as the $min[S_{ys}, S_{yf}]$. The deformation ratios of the sphere and the flat, δ_s^*, δ_f^*, are:

$$\delta_s^* = \frac{\delta_s}{\Delta} \quad , \quad \delta_f^* = \frac{\delta_f}{\Delta}, \tag{2.2}$$

where δ_s and δ_f are the deformations on the sphere and the flat respectively and Δ is the total applied displacement.

Figure 2.5 shows the relationship between the deformation ratio of the sphere, δ_s^*, and the yield strength ratio, S_y^*, for 5 different material property sets, which are presented in Table 2.1. The sphere deformation ratio, δ_s^* starts near 0.9 at $S_y^* = 0.1$ and is constant up to $S_y^* = 0.6$. From $S_y^* = 0.6$ to $S_y^* = 1$ the sphere deformation ratio, δ_s^*, decreases with an increasing rate. At $S_y^* = 1$ the flattening phase ends with a rapid change in the sphere deformation ratio, δ_s^*, into the indentation phase. From $S_y^* = 1$ to $S_y^* = 1.7$ the sphere

deformation ratio is decreasing with a decreasing rate. After this point the deformation ratio can be considered to be nearly constant for each mentioned case.

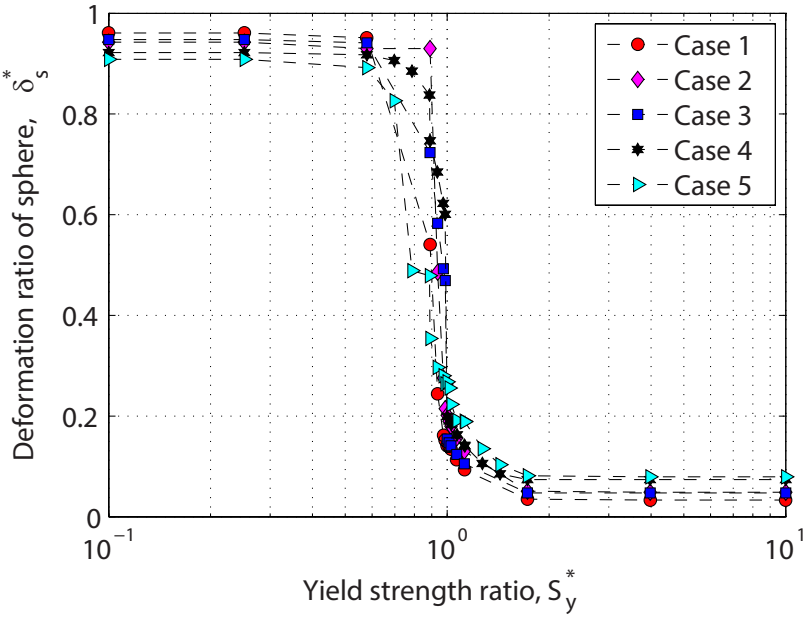

Figure 2.5: Deformation ratio of the sphere for five different cases shown in Table 2.1.

2.2.3 Real radius of contact

Figure 2.6 shows the contact radius for $S_y^* = 0.1$ to $S_y^* = 10$ for different material properties. It has to be considered that the x-axis is in logarithmic scale. The material properties used in Fig. 2.6 are presented in Table 2.1. The results are for contact between a sphere with $R = 1$ mm and a flat with an applied displacement ratio of $\Delta/R = 0.04$. The same pattern can be observed for all of the cases. It is interesting that although the rapid change in the deformation plot (Fig.2.5) occurs at $S_y^* = 1$, for the contact radius, it can be seen that the transition from the flattening phase to the indentation phase happens slightly after $S_y^* = 1$ and near $S_y^* = 1.07$. Before $S_y^* = 0.6$ the contact radius can be considered to be constant for all of the cases. After this point, the contact radius starts to decrease with an increasing slope up to $S_y^* \simeq 1.1$. The contact radius starts increasing significantly from

$S_y^* \simeq 1.1$ to $S_y^* = 1.7$, when it reaches a value higher than that of the flattening phase. The contact radius can be considered to be constant after this point.

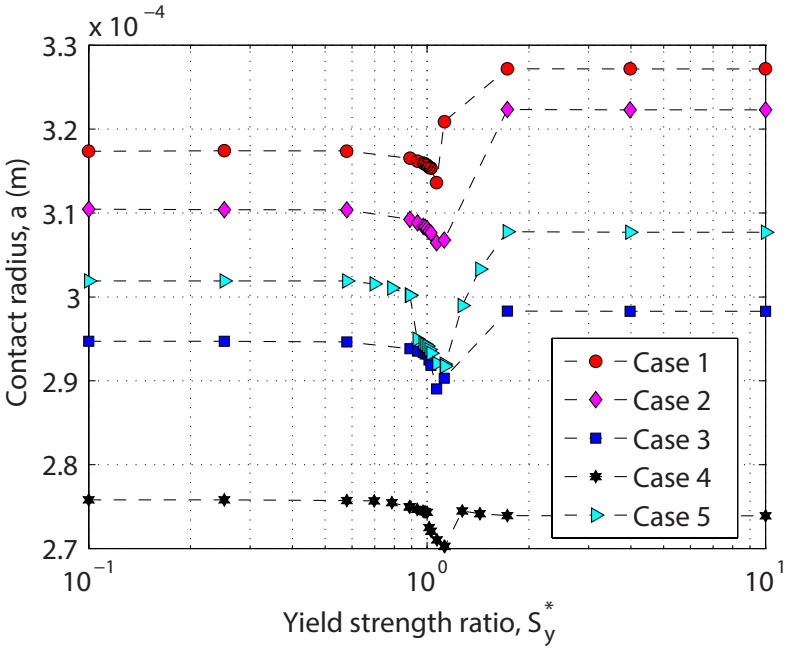

Figure 2.6: Contact radius for five different cases shown in Table 2.1.

2.2.4 Hardness

Figure 2.7 shows the FEM results for the average normal pressure for different values of S_y^* for the cases presented in Table 2.1. The pressure is nearly constant from $S_y^* = 0.1$ to $S_y^* \simeq 0.94$. After this point, there is a rapid change from $S_y^* \simeq 0.94$ to $S_y^* \simeq 1.06$. From this point up to $S_y^* = 1.7$, the hardness behaves differently for different cases. For Cases 2-4, the average normal pressure has a maximum around $S_y^* = 1.4$, which matches the contact radius results shown in Fig. 2.6. The contact radius results show a minimum at $S_y^* = 1.07$, which causes the average normal pressure maximum at the same point for cases 2 to 5. For Case 1, which is a highly plastic material, the hardness does not have a maximum. After $S_y^* = 1.7$, the average normal pressure can be considered to be constant. This is probably due to differences in the deformed geometry of the surfaces.

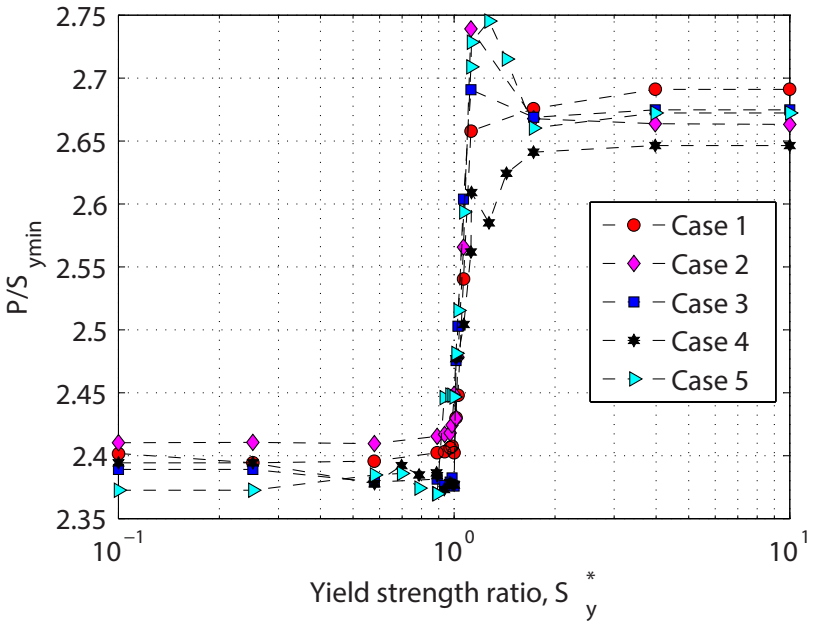

Figure 2.7: Normalized average normal pressure, P/S_{ymin}, vs. the yield strength ratio, S_y^*, for different material properties from Table 2.1.

2.2.5 Contact force

The same five cases have been analyzed for the contact force, as can be seen in Fig. 2.8. The contact force has nearly the same pattern as the contact radius (Fig. 2.6). It is interesting that in contradiction to the contact radius, the transition from the flattening phase to the indentation phase happens at almost exactly $S_y^* = 1$.

2.3 Final formulation

A formulation has been developed based on the FEM results for the deformations of both objects, the real area of contact and the contact force. The formulation is verified for modulus of elasticity, $E = [50, 300]$ GPa, yield strength ratio, $S_y^* = [100, 1100]$ MPa. The most difficult task is predicting the trend of the real radius of contact shown in Fig. 2.3. This trend is the result of the effects of the deformations and the radius of curvature. For the case that both of the objects are deforming, changes in the radius of curvature cannot

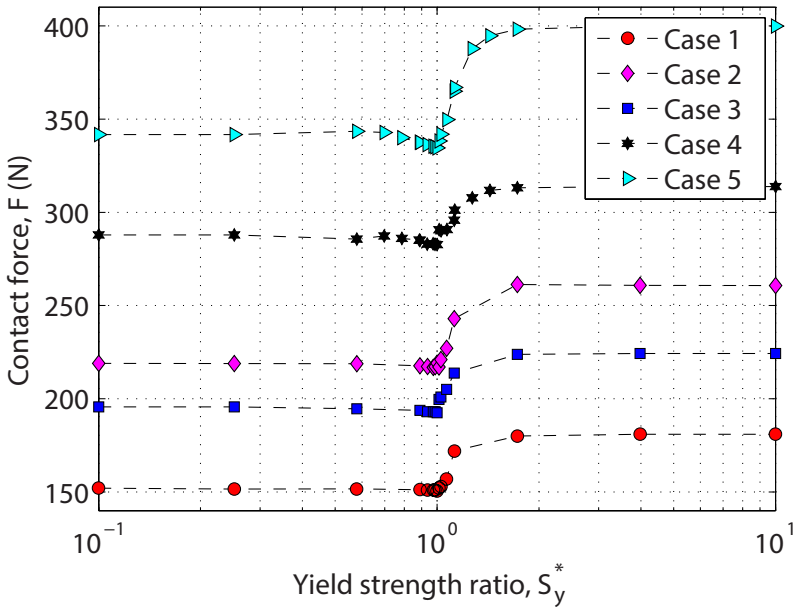

Figure 2.8: Contact force vs. the yield strength ratio, S_y^*, for different material properties in Table 2.1.

be neglected. We defined five main steps in order to find the correct relationship and finally develop the expression for the contact force:

Step 1: The deformation on each object is found, δ_s and δ_f.

Step 2: The radius of the curvature is updated, R'.

Step 3: The expression for the real radius of contact based on the updated deformations and the deformed radius of curvature is developed, a.

Step 4: The average normal pressure is characterized.

Step 5: The expression for the contact force is developed, F.

Here only the final formulation has been presented; details for these steps are presented in the curve fitting section.

2.3.1 Elastic phase and the modified radius of curvature

In the new empirical model, we are using the deformation on only one of the objects as an input; therefore, it is necessary to find the force expression of the Hertzian theory with respect to only one object's deformation. For large and small S_y^* values plastic deformation is located only on one object. One can simply find that the deformation on each object in Hertzian theory can be found as:

$$\frac{\delta_s}{\Delta} = \frac{E'\,(1-\nu_s^2)}{E_s} \quad , \quad \frac{\delta_f}{\Delta} = \frac{E'\,(1-\nu_f^2)}{E_f}, \tag{2.3}$$

where δ_s and δ_f are the deformations on sphere and the flat respectively, and Δ is the total displacement. Hertzian theory also provides the following equations for the contact force:

$$F_e = \frac{4}{3}\,R\,E'\,\Delta^{1.5} \quad , \quad a = \sqrt{R\,\delta}, \tag{2.4}$$

where R is the radius of the sphere for our case, because $R_f = \infty$. In our model, we consider the change in the radius of curvature during the contact. If we consider the sphere to be rigid and neglect the effect of pile-up and sink-in, then:

$$a = (R^2 - (R-\Delta)^2)^{0.5}. \tag{2.5}$$

Now if we apply the deformation of the sphere and the radius of curvature, to find the same contact radius the following condition should be satisfy:

$$(R^2 - (R-\Delta)^2)^{0.5} = (R'^{\,2} - [R' - (\Delta - \delta_s)]^2)^{0.5} \tag{2.6}$$

Solving this equation for R' with the first order accuracy yields:

$$\frac{R'}{R} = 1 + \frac{\delta_s}{\Delta} - \frac{\delta_s}{R} = 1 + \delta_s^* - \frac{\Delta\,\delta_s^*}{R} \tag{2.7}$$

For the elastic phase, $\Delta\,\delta_s^*/R$ can be neglected, therefore

$$a = \sqrt{R\,\Delta} = \sqrt{R'\,\delta_s}. \tag{2.8}$$

By using Eqs. (2.3, 2.8), one can find that:

$$R\,\Delta = R\,\delta_s\,\frac{E_s}{E'\,(1-\nu_s^2)} = R'\,\delta_s$$

Therefore:

$$R' = R\,\frac{E_s}{E'\,(1-\nu_s^2)} \tag{2.9}$$

Combining Eqs. (2.3-2.9) will result in the following expression for the elastic contact force between a sphere and a flat with respect to the deformation on the sphere and the modified radius of curvature:

$$F_{es} = \frac{4}{3}\,R'\,\frac{E_s}{(1-\nu_s^2)}\delta_s^{1.5}. \tag{2.10}$$

The same equation form can be used for the flat. This method of using the Hertzian theory helped us to develop the formulations based on the deformation of only one of the objects. Considering the effect of change in the radius of curvature helps to developed model to satisfy larger deformations than most of the previous models.

2.3.2 Elastic-plastic phase

The contact can be divided into two phases: the elastic phase and the elasto-plastic phase; however, to define these phases, the deformations have to be defined. If one applies Δ as a displacement, a portion of this displacement will deform the flat and the other portion will deform the sphere, such that:

$$\Delta = \delta_s + \delta_f \tag{2.11}$$

where Δ is the applied displacement and δ_s and δ_f are the deformations on the sphere and the flat, respectively. Therefore, the normalized parameters have been defined as:

$$\Delta' = \frac{\Delta}{R} \quad , \quad \delta_s^* = \frac{\delta_s}{\Delta} \quad , \quad \delta_f^* = 1 - \delta_s^* \tag{2.12}$$

where Δ' is the normalized applied displacement, δ_s^* and δ_f^* are the deformation ratios for sphere and flat, respectively, and R is the original radius of the sphere. To calculate δ_s^*, three criteria have to be defined with respect to the yield strength ratio, S_y^*.

For $S_y^* \leq 1$:

$$\begin{aligned}\delta_s^* =& 1.115\ (\Delta')^{0.0528} \sin\left[5.592\ (\Delta')^{1.37} + \frac{\pi}{2.37}\right] \times \\ & \sin\left[0.625\ (S_y^*)^2 + \frac{\pi}{2.16}\right]\end{aligned} \tag{2.13}$$

For $1 < S_y^* \leq 1.53$:

$$\begin{aligned}\delta_s^* =& -22.49 \left(\frac{E'}{S_{ymin}}\right)^{-0.7} \sin\left[45.63\ (\Delta')^{1.75} + 0.094\pi\ (S_y^*)^{4.01}\right] \times \\ & \sin\left[1.546\ (S_y^*)^{-9.22} + 1.035\right]\end{aligned} \tag{2.14}$$

And for $1.53 < S_y^*$:

$$\begin{aligned}\delta_s^* =& 0.852\ \left(\frac{E'}{S_{ymin}}\right)^{-0.7} (\Delta')^{-0.41}\ (S_y^*)^{0.031} \times \\ & \tan^{-1}\left[0.142\ \ln(S_y^*)^{1.06\Delta'} + 3.22\right] e^{C_\delta}\end{aligned} \tag{2.15}$$

where C_δ is:

$$C_\delta = 2.307(\Delta')^{0.46S_y^*} - 0.7 \tag{2.16}$$

and E' is:

$$E'^{-1} = \frac{(1-\nu_s^2)}{E_s} + \frac{(1-\nu_f^2)}{E_f}. \tag{2.17}$$

The deformation on the flat can be calculated from Eq. (2.12).

Now the updated radius of curvature can be calculated as (see Appendix A for derivation):

$$\frac{R'}{R} = 1 + \delta_s^* - \frac{\Delta\,\delta_s^*}{R} \tag{2.18}$$

Using the updated radius of curvature, R', and the developed expressions for the deformations, the critical values for the elastic and elasto-plastic phases can be calculated. It has to be considered that here the formulation is based on deformation of only sphere for $S_y^* \leq 1$ and of only the flat for $S_y^* > 1$. Therefore, the Hertzian theory has to be updated for the deformation of only one of the objects. Appendix A provides the new formulation. Yielding begins when δ_s or δ_f is equal to δ_c; however, it effectively starts at $\delta_{s|f} = 1.9\ \delta_c$. Now that the critical value for deformation is defined, the problem can be divided into two main parts with respect to the S_y^*. Ideally for $S_y^* \leq 1$, the problem is closer to a flattening case, in which the sphere is the weaker object, and for $S_y^* \geq 1$ the problem is closer to an indentation case; however, we observed that the transition between these two phases occurs at $S_y^* = 1.07$ instead of $S_y^* = 1$.

The real radius of contact can be calculated as follows.

For $S_y^* \leq 1.07$ use Eqs. (2.19-2.25):

$$\delta_n = \frac{\delta_s}{\delta_c} \tag{2.19}$$

if $\delta_n \leq 3.7$:

$$a = \sqrt{R'\ \delta_s} \tag{2.20}$$

if $3.7 < \delta_n \leq 408$:

$$a = R' \left(\frac{\pi C S_{ys}}{2E'} \right) \left[\delta_n \left(\frac{\delta_n}{1.9} \right)^B \right] \chi_{11} \tag{2.21}$$

where

$$B = 0.14 e^{\frac{23 S_{ys}}{E'}} \tag{2.22}$$

as defined in the JG model and

$$\chi_{11} = 0.4 + 0.55 \delta_n^{0.022} + 0.283 \delta_n^{-0.5} S_y^{*6} \tag{2.23}$$

if $\delta_n > 408$:

$$a = R' \left(\frac{\pi C S_{ys}}{2E'} \right) \left[\delta_n \left(\frac{\delta_n}{1.9} \right)^B \right] \chi_{12} \tag{2.24}$$

and

$$\chi_{12} = 1 + 0.024 - 0.004(\delta_n - 408)^{0.3814} + [0.013 + 2.2 \times 10^{-5}(\delta_n - 408)] S_y^{*6}. \tag{2.25}$$

For $S_y^* > 1.07$ use Eqs. (2.26-2.33):

$$\delta_n = \frac{\delta_f}{\delta_c} \tag{2.26}$$

if $\delta_n \leq 3.7$:

$$a = \sqrt{R'\ \delta_f} \tag{2.27}$$

if $3.7 < \delta_n \leq 408$:

$$a = R' \left(\frac{\pi C S_{yf}}{2E'} \right) \left[\delta_n \left(\frac{\delta_n}{1.9} \right)^B \right] \chi_{21} \tag{2.28}$$

and

$$\chi_{21} = 0.4 + 0.55\delta_n^{0.022} + 0.283\delta_n^{-0.5} S_y^{*C_{\chi\ 21}} \tag{2.29}$$

where

$$C_{\chi 21} = -0.091 e^{-0.008\delta_n} \tag{2.30}$$

if $\delta_n > 408$:

$$a = R' \left(\frac{\pi C S_{yf}}{2E'} \right) \left[\delta_n \left(\frac{\delta_n}{1.9} \right)^B \right] \chi_{22} \tag{2.31}$$

and

$$\chi_{22} = 1 + 0.024 - 0.004(\delta_n - 408)^{0.3814} + [0.013 + 2.2 \times 10^{-5}(\delta_n - 408)] S_y^{*C_{\chi\ 22}}. \tag{2.32}$$

where

$$C_{\chi\ 22} = -0.0091 \left[\log(\delta_n - 408) \right]^{3.53} \tag{2.33}$$

In the expressions developed for the real radius of curvature, $\chi_{11,12,21,22}$ are small modifications on the JG model. The detailed explanation can be found in Appendix C.

The next step is formulating the average pressure during fully plastic deformation (ie. the hardness). The finite element results show that the contact is plastic when $\delta_n \geq 110$ for both $S_y^* \leq 1.07$ and $S_y^* > 1.07$. A step transition for hardness happens at $S_y^* = 1$ to $S_y^* = 1.12$ (details are provided at Appendix D). The Jackson-Green expression [54] for the hardness has been used for the flattening phase, and the Jackson et al. expression in [53] has been used for the indentation phase. Finally, the following expression has been provided

to transition the hardness between the indentation and flattening phases:

$$H = \frac{H_i - H_f}{\pi}\left[\tan^{-1}\left(300\,\log[S_y^* - 0.06]\right) + \frac{\pi}{2}\right] + H_f \tag{2.34}$$

where H_f and H_i are the hardnesses for the flattening and the indentation phases, respectively. They are given as:

$$H_f = 2.84 - 0.92\left[1 - \cos\left(\pi\frac{a}{R}\right)\right] \tag{2.35}$$

and from the slip-line theory analysis of Jackson et al. [53]:

$$\begin{aligned} H_i = {} & \frac{4}{3\sqrt{3}}\left(\frac{a}{R}\right)^{-2} \times ... \\ & \left[\frac{1}{3}\left(\frac{a}{R}\right)^3 - \left(1 - \cos^{-1}\left[\frac{a}{R}\right]\right)\left(1 - \left[\frac{a}{R}\right]^2\right)^{3/2} - \frac{a}{R} + \frac{\pi}{2} + 1\right]. \end{aligned} \tag{2.36}$$

Finally the contact force expression for $S_y^* \leq 1.07$ is:

$$F = W_e F_{es} + W_p F_p \tag{2.37}$$

and for $1.07 < S_y^*$:

$$F = W_e F_{ef} + W_p F_p \tag{2.38}$$

where F_p is the fully plastic force, and F_{es} and F_{ef} are the fully elastic forces for the sphere and the flat, respectively.

$$F_{es} = \frac{4}{3}R'\frac{E_s}{(1-\nu_s^2)}\delta_s^{3/2}, \tag{2.39}$$

$$F_{ef} = \frac{4}{3}R'\frac{E_f}{(1-\nu_f^2)}\delta_f^{3/2}, \tag{2.40}$$

where F_{es} and F_{ef} are for the flattening ($S_y^* \leq 1.07$) and the indentation ($S_y^* > 1.07$) phases respectively. Next

$$F_p = \pi a^2 \ H, \tag{2.41}$$

where H and a can be calculated from the Eqs (2.19-2.36) and W_e and W_p are the weights for the fully elastic and the fully plastic phases, respectively, which are calculated for the different phases as below.

For $S_y^* <= 1.07$:

$$\begin{aligned} W_e &= e^{-1.6(\delta_n - 1.9)^{\ 0.16}} \\ W_p &= 0.95 - e^{-0.58\ {\delta_n}^{0.3}} \end{aligned} \tag{2.42}$$

and for $S_y^* > 1.07$:

$$\begin{aligned} W_e &= e^{-1.7(\delta_n - 1.9)^{\ 0.26}} \\ W_p &= 1 - e^{-0.465\ {\delta_n}^{0.45}} \end{aligned} \tag{2.43}$$

Details for the source of the contact force expression have been provided in the following section.

2.4 Curve fittings

2.4.1 Curve-fittings for the deformation ratio

The deformation on each object has been normalized with the total relative displacement of the sphere and the flat, Δ. There are many parameters that affect the deformations on each object, such as the yield strength ratio, the modulus of elasticity, the applied displacement and the minimum yield strength. Finding the relationship between the deformation and

all of these parameters is complicated; however, it has to be considered that the effects are relatively small and can be later modified in the next steps of the curve fittings.

Figure 2.9 shows the relationship between the deformation ratio of the sphere, δ_s^*, and the yield strength ratio, S_y^*, for different applied displacements. It can be seen that by increasing the applied displacement, a larger portion of the displacement occurs on the weaker material; however, the maximum difference between the largest displacement and the smallest displacement is approximately 10 %. By analyzing the FEM data for the

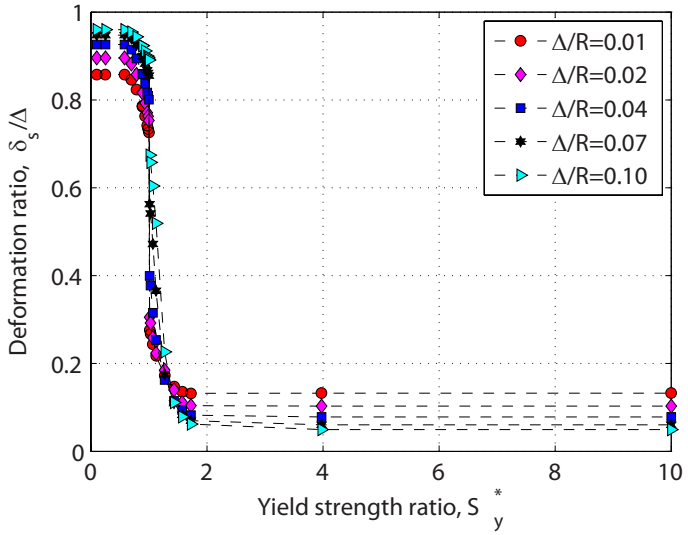

Figure 2.9: Relation between the deformation ratio of the sphere, δ_s^* and the yield strength ratio, S_y^* for case 4 defined in Table 2.1.

deformations, an interesting relation can be observed. Figure 2.10 contains the same results as Fig. 2.9 in a 3D plot. It can be seen that there is a rapid change between the flattening phase and the indentation phase. The applied displacement has a significant effect on the deformation ratio of the sphere, δ_s^*, especially when $0.95 \geq S_y^* \leq 1.2$. The rapid change decreases as the applied displacement increases. As was shown in Fig. 2.10, the deformation ratio changes with a significant rate around $S_y^* \simeq 1.07$ and $S_y^* \simeq 1.53$. This forces us to section the governing formulation into three phases, as explained in the formulation section. To consider the effect of the reduced modulus of elasticity, E', and the minimum yield

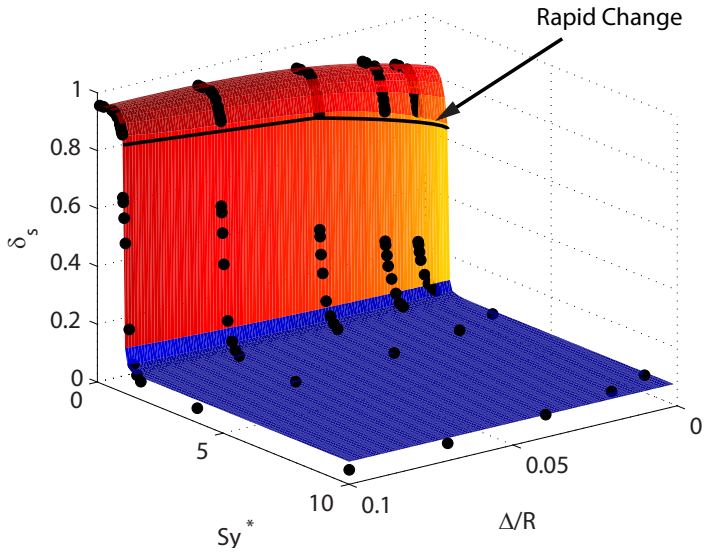

Figure 2.10: Relation between the deformation of the sphere and the yield strength for case 4 defined in Table 2.1.

strength, $S_{y\,min}$, we used the well known dimensionless parameter, $E'/S_{y\,min}$, which has been used in the previous literature to normalize the effect of the material properties. Figure 2.11 shows an example of the effect of the E' and $S_{y\,min}$ on the deformation ratio for $S_y^* = 10$ and $\Delta/R = 0.04$. We applied the effect of E' and $S_{y\,min}$ only for the indentation case, because for the flattening case the effect is smaller and also cannot be charactrized with only $E'/S_{y\,min}$. Thus it made the formulation more complicated. Therefore, we decided to apply small modifications on the radius of contact, rather than the deformation ratio.

2.4.2 Curve-fittings for the contact radius

In order to verify that applying the effect of the deformations on both of the objects and the change in the radius of curvature results in the same trend as can be observed in Fig. 2.6, we applied these effects to the JG model. Figure 2.13 shows the updated JG model with the δ_s and R' for Case 4 (from table 2.1), with $R = 1$ mm and $\Delta = 4 \times 10^{-5}$ m. The JG model shows slightly larger values with less than a 2 % difference with the FEM results. The updated JG model has the same trend as the FEM results, and the maximum difference with

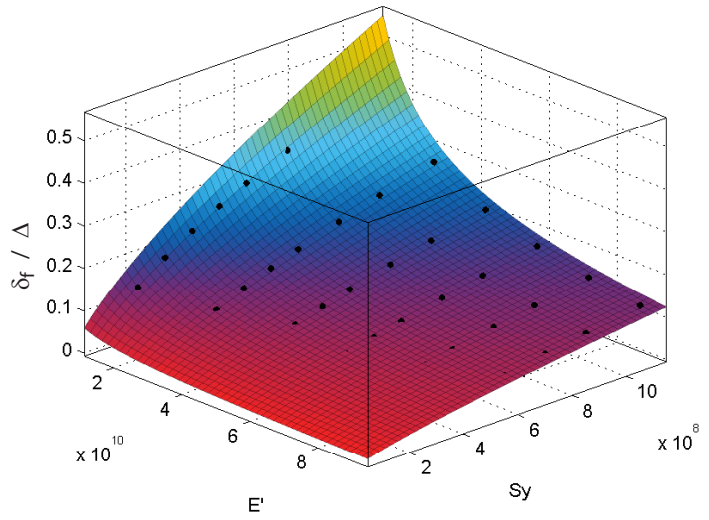

Figure 2.11: Relation between the deformation ratio of the sphere, δ_s^*, and the minimum yield strength, $S_y\,min$, and reduced modulus of elasticity, E', for $S_y^* = 10$ and $\Delta/R = 0.04$.

the numerical results is 3.2 % at $S_y^* \simeq 1$. The r_p in the graph is the truncated contact radius, $r_p = \sqrt{R^2 - (R-\Delta)^2}$, and is plotted for the sake of comparison. The truncation method has been used extensively but is again shown here to have significant errors. This verifies the idea of using the deformation of one object and modifying the radius of curvature. The correction factors $\chi_{11,12,21,22}$ from Eq. (2.23,2.25,2.29,2.32) were applied in order to reduce the small differences between the model and the FEM results.

Figure 2.13 shows the relationship between the difference of the updated JG model for the radius of contact, a, and the normalized deformation, δ_n. The FEM results are for $\Delta/R = 0.04$ and 27 different sets of material properties while holding $S_y^* = 0.1$ (the flattening case). As can be seen, there is a critical value for these results at $\delta_n \simeq 408$. The difference increases from $\delta_n = 0$ to $\delta_n = 408$, and after this point, the difference starts decreasing. It should be noted that the range of δ_n used in our analysis is nearly 100 times larger than the ranges used in the JG and KE models.

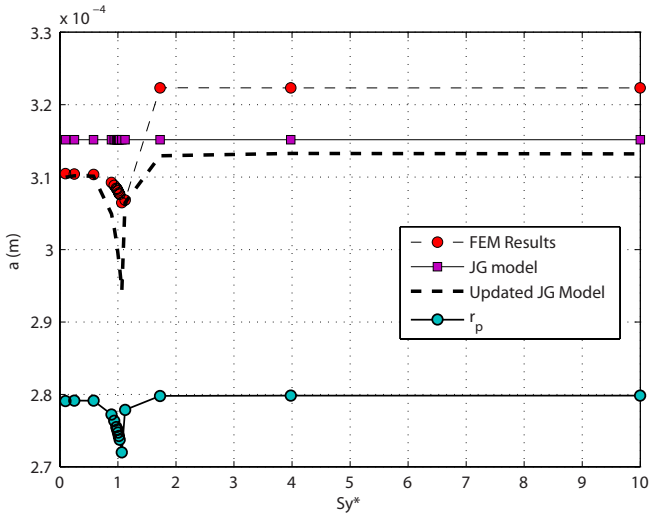

Figure 2.12: Comparison between the FEM results, JG model, updated JG model and the radius of truncated contact area for contact radius versus different yield strength ratio, S_y^*, for material properties same as case 4 and $\Delta/R = 0.04$.

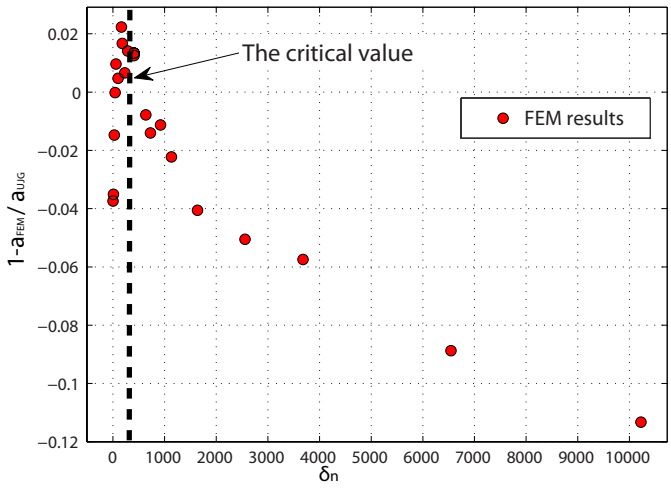

Figure 2.13: The difference between the FEM results and the updated JG model.

The same procedure has been applied for $S_y^* = 1$ and $S_y^* = 10$ and the same critical value has been observed for both. The effects of E' and $S_{y\,min}$ have been considered for all of the cases, and incorporated in the resulting findings, Eqs. (2.21-2.32).

2.4.3 Hardness

Finding at what δ_n the normal average pressure reaches the fully plastic state (i.e. hardness) is necessary to develop the formulation. Figure 2.16 shows the relationship between the normal average pressure and the normalized deformation δ_n for $S_y^* = 0.1$, $S_y^* = 1$ and $S_y^* = 10$. It should be noted that each point in the plot represents a set different material properties, which is why there appear to be scatter in the results. The normal average pressure appears to peak at approximately $\delta_n = 110$ (similar to KE [69]). The hardness for $S_y^* = 1$ is slightly smaller than the flattening part, $S_y^* = 0.1$. We neglected this difference in our formulation. The indentation part shows larger values for the whole range of δ_n.

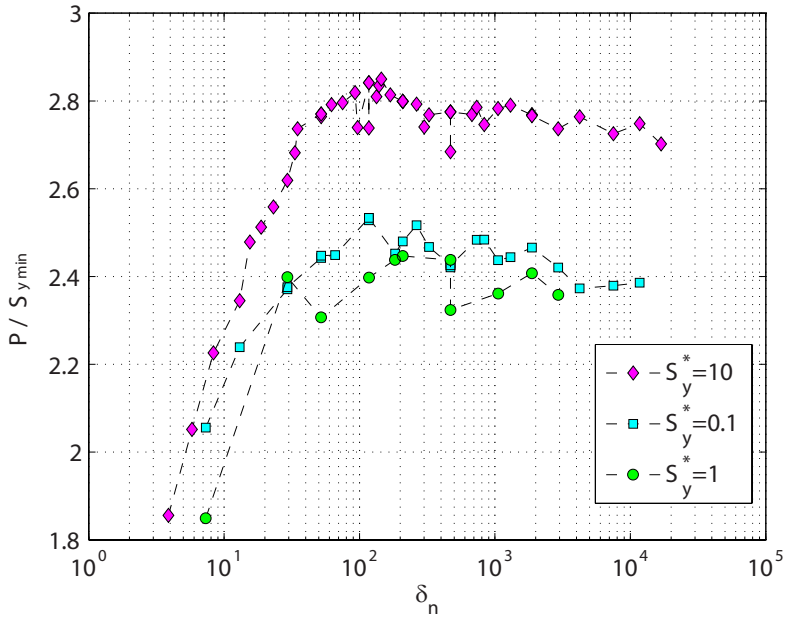

Figure 2.14: The normal average pressure vs. the normalized deformation.

We compared our FEM results with the previous models for the hardness. In Fig. 2.17 the FEM results for $S_y^* = 0.1$, $S_y^* = 1$ and $S_y^* = 10$ are shown. The Jackson-Green and Kogut-Etsion models are presented for the flattening part, and the Yu-Blanchard and Alcala have been compared for the indentation part. Results for $S_y^* = 0.1$ and $S_y^* = 1$ have a good agreement with the Jackson-Green expression for the hardness. For the indentation part,

$S_y^* = 10$, the FEM results show a good agreement with the JGP solution [53]; therefore, we did not use a new fitting for the hardness. It should be noted that our FE modeling could not converge for deformations that result in $a/R > 0.5$, therefore we cannot verify either of the models for larger deformations. However assigned verification for larger deformation of the flattening case can be found in [110].

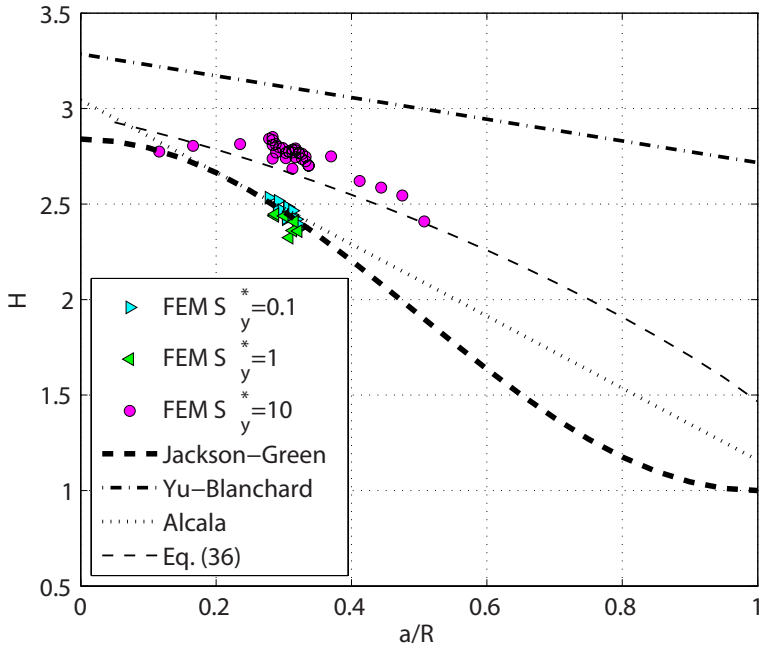

Figure 2.15: The comparison between the FEM results and the previous models for hardness.

2.5 Results and Comparisons

The formulation has been compared with the FEM results for different material properties than the ones used for the fittings. For the FEM, the deformations on both objects, the radius of contact, the average normal pressure and the contact force have been compared with the new formulation. It has been shown that the new formulation matches the FEM results within a 5 % error range for all of the cases. Finally, the new model has been compared with the previous models for five different sets of material properties.

2.5.1 Deformation ratio

Figure 2.16 shows the comparison between the FEM results and Eqs. (2.13-2.15). For this case $S_{ymin} = 300$ MPa, $E_s = 71.7$ GPa, $E_f = 200$ GPa, $\nu_s = \nu_f = 0.3$ and $\Delta/R = 0.04$. There is a small error between the FEM results and the formulation. As can be seen, because of the large rapid change near $S_y^* = 1$, finding a good fit is difficult; however, the formulation works within an acceptable range.

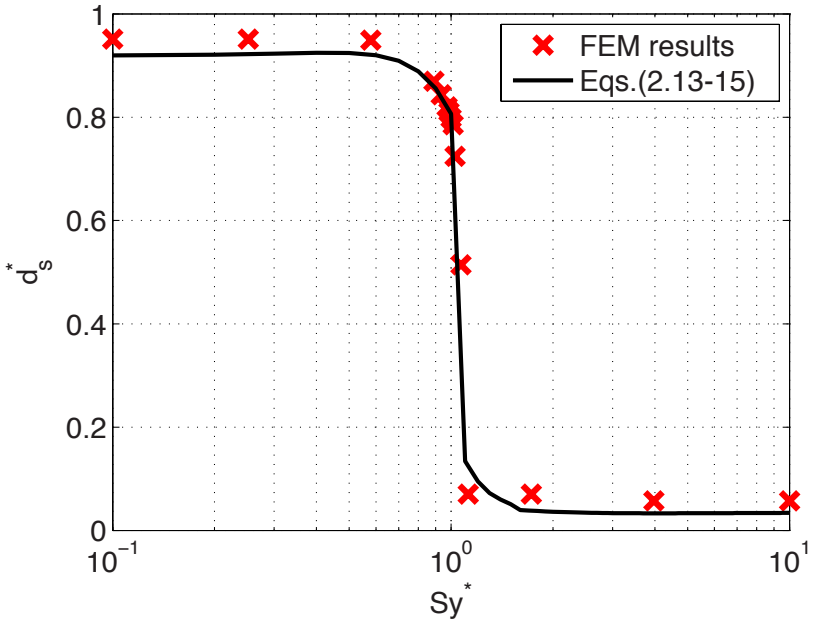

Figure 2.16: Comparison between the FEM results and Eqs. (2.13,2.14,2.15) for δ_s^* vs. S_y^*, where $S_{y\ min} = 300$ MPa, $E_s = 71.7$ GPa, $E_f = 200$ GPa, $\nu_s = \nu_f = 0.3$ and $\Delta/R = 0.04$.

2.5.2 Radius of contact (a)

Figure 2.17 shows the contact radius, a, versus the normalized applied displacement, Δ/R. The deformations considered for this case range from nearly elastic to highly plastic ($1 < \delta_n < 14676$). This shows that Eqs. (2.27, 2.28, 2.31) are working for the large deformations as well as the small deformations. The results have been compared with the JG [54] and KE [69] flattening models and the KK [71] and YK [122] indentation models. Both of

the flattening models show larger values, while the JG model works slightly better than KE. In contrast, the indentation models show smaller values, and the YK model works better than the KK model.

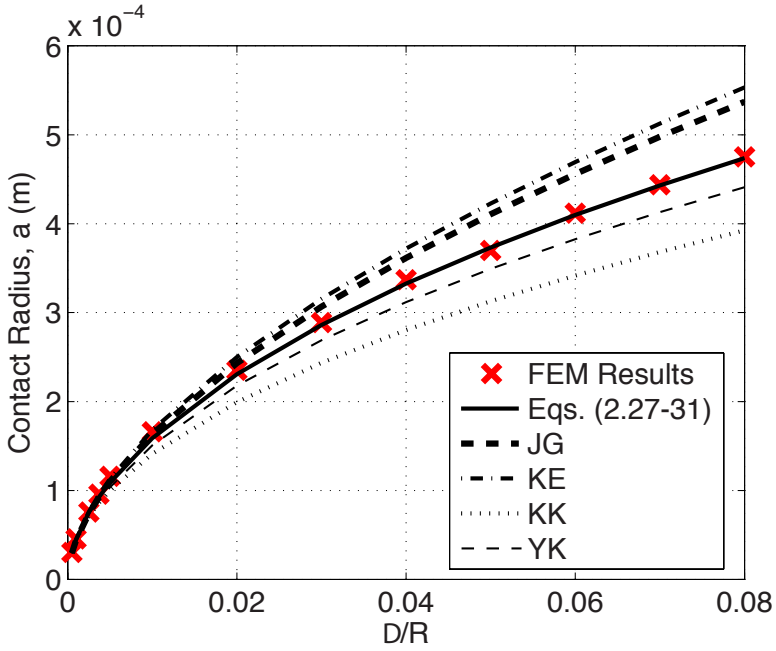

Figure 2.17: Comparison between the FEM results and Eq. (2.27-2.31) for a vs. Δ/R, where $S_{y\ s} = 1000\ MPa$ $S_{y\ f} = 100$ MPa, $E_s = E_f = 300$ GPa, $\nu_s = \nu_f = 0.3$.

Figure 2.18 shows the contact radius, a, versus the yield strength ratio, S_y^*, for Case 5 defined in Table 2.1. The new model has been compared with the previous models. The previous models have a constant value because they are either for the flattening case, $S_y^* \simeq 0$, or for the indentation case, $S_y^* \simeq \infty$. The new model shows the same shape as the FEM results, it has to be considered that the shape of the FEM results has not been artificially fabricated into the curve fittings. The shape arises from considering the effect of the deformation on each object and the effects of changes in the radius of curvature during contact. The difference between Eqs. (2.20-2.31) and the FEM results is less than 1 %. All the previous models show smaller values for this case, while the flattening cases are larger than the indentation cases, and JG works better than the other models. This shows that the deformation of the

sphere in the indentation part is more important than the deformation of the flat for the flattening part.

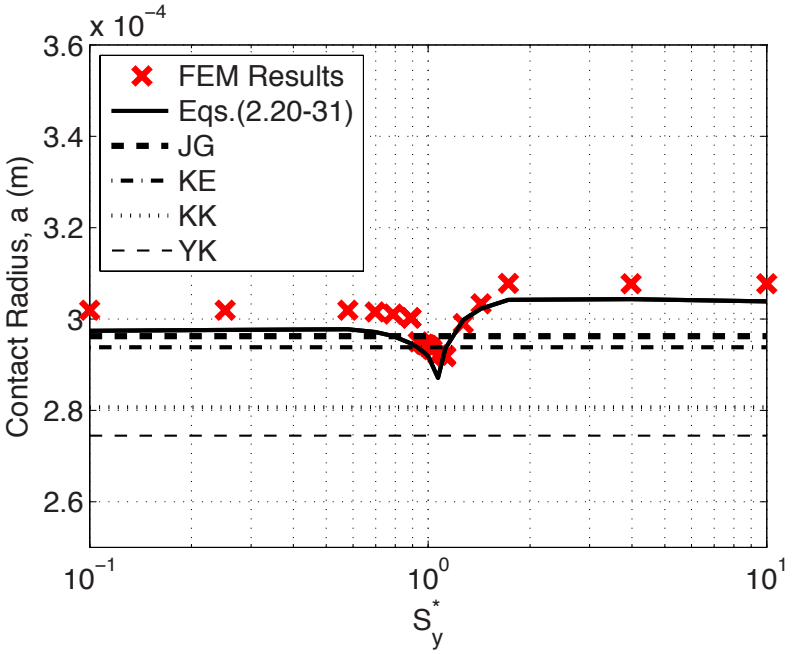

Figure 2.18: Comparison between the FEM results and Eq. (2.20-2.31) for a vs. S_y^* for case 5 defined in Table 2.1.

2.5.3 Normal average pressure

As explained in Section 3 the average normal pressure P, is calculated from the previous literature, Eqs. (2.34-2.36). For the flattening phase, the expression in [54] has been used, and for the indentation phase, the expression from [53] has been used. The methodology for the curve fitting and comparison of the FEM results and previous models was shown in the last section.

Figure 2.19 shows the comparison of the normal average pressure between the FEM results and different models for different yield strength ratios, S_y^*. The material properties used for this plot are Case 1 (presented in Table 2.1). The difference between Eq.(2.34) and the JG model for the flattening part is due to the difference in the contact radius. The average normal pressure is nearly constant for $S_y^* < 1$ and rapidly changes to the indentation

case for $S_y^* > 1$. As can be seen, Eq. (2.34) can simulate the rapid change between the flattening and the indentation phases. For all of the other cases presented in Table 2.1, the maximum difference between the FEM results and Eq. (2.34) is less than 5 %.

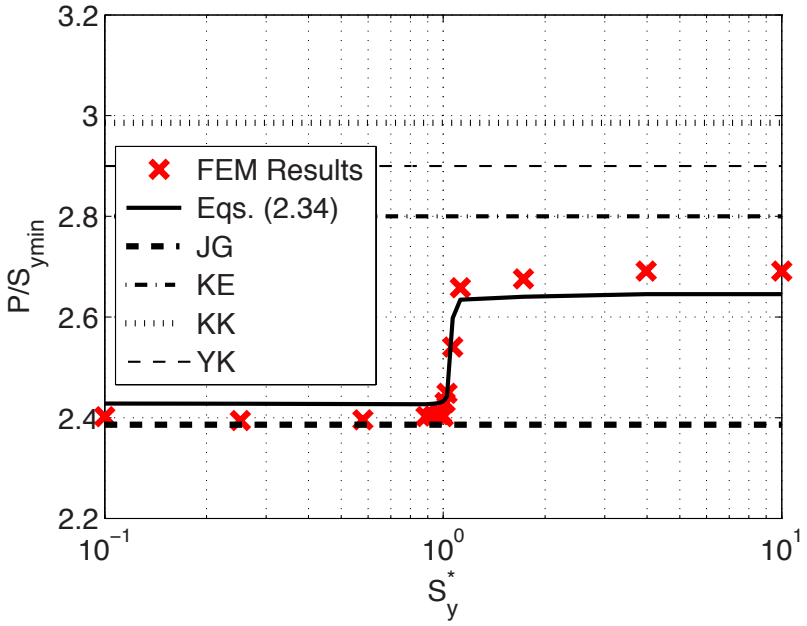

Figure 2.19: Comparison between the FEM results and Eq. (2.34) for H vs. S_y^* for case 1 defined in Table 2.1.

2.5.4 Contact Force

Finally, Eq. (2.37-2.38) for the contact force are compared with the FEM results. Figure 2.20 shows the contact force with respect to the applied displacement for the same material properties used for the results shown in Fig. 2.17. The material properties used for this case result in highly plastic deformation and are closer to an indentation case. The new model and the YK model show a good agreement with the FEM results. The KE model shows larger values. The reason is that the material properties are not suited for this model, and also due to the fact that the KE model was developed for much smaller deformations. The JG and KK models result in smaller values with nearly 30 % and 20 % differences from the FEM results, respectively.

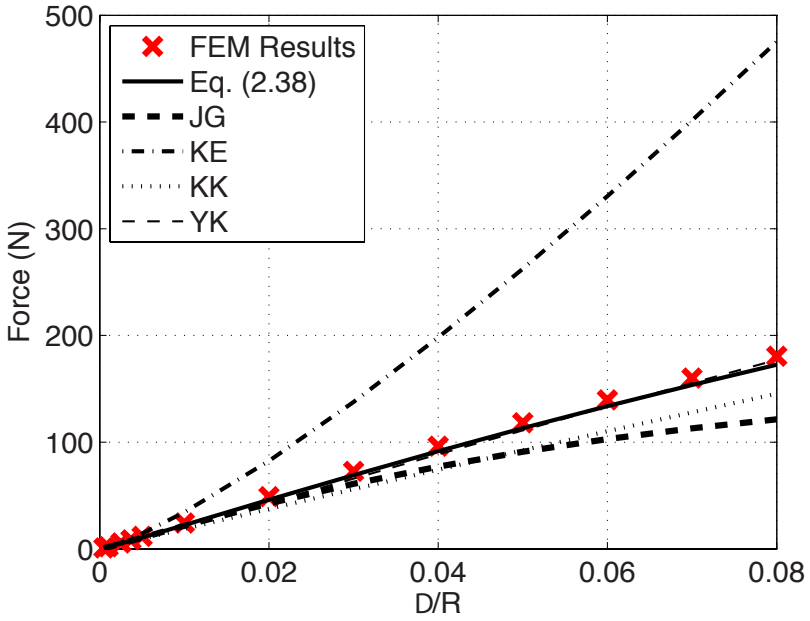

Figure 2.20: Comparison between the FEM results and 2.38) for F vs. Δ/R, where $S_{y\ s} = 1000\ MPa$ $S_{y\ f} = 100$ MPa, $E_s = E_f = 300$ GPa, $\nu_s = \nu_f = 0.3$.

Figure 2.21 compares the FEM results to the other models for the contact force and different yield strength ratios. The material properties used for this graph are Case 3, which are presented in Table 2.1. It should be considered that the minimum yield strength is held constant and only S_y^* changes. The JG model has a good agreement with the FEM results for the flattening part, $S_y^* < 1$. The KE model shows larger values, compared to the FEM results. The KK and YK models show smaller values compared to the indentation phase, $S_y^* > 1$. The new model, Eq. (2.37,2.38), shows a good agreement with the FEM results. The same results have been analyzed for the other cases in Table 2.1, and the maximum difference between the new model and the FEM results is always less than 5 %. The average difference between the FEM results and the developed formulation is 3%.

2.6 Conclusions

In this study we analyzed a largely ignored aspect of the contact of two elasto-plastic objects. Unlike the previous models, both of the objects are considered to be subjected

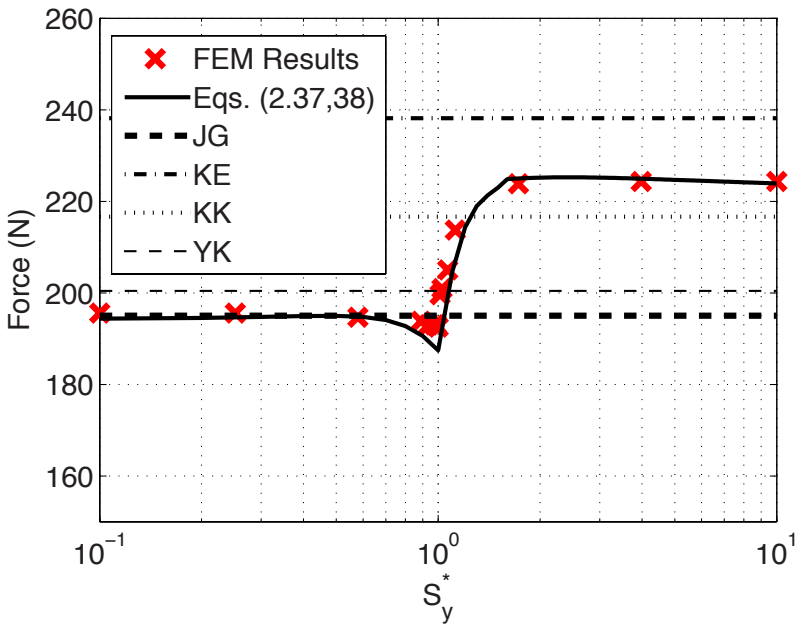

Figure 2.21: Comparison between the FEM results and Eqs. (2.37,2.38) for F vs. S_y^* for case 3 defined in Table 2.1.

to elastic-plastic deformations. This introduces a bridge between the two conventional categories of contact models, i.e. flattening and indentation models. We introduced a new parameter, S_y^*, to characterize this contact problem. More than 400 different cases of material properties and initial conditions have been simulated numerically, using FE techniques, with the material properties ranging from $50 \leq E \leq 300$ GPa, , $0 \leq a/R \leq 0.5$, $50 \leq S_{y\ min} \leq 1100$ MPa, and $\nu = 0.3$. The finite element results have been analyzed for the deformations on both objects, the radius of contact, the average normal pressure and the contact force.

A comprehensive formulation has been developed in order to satisfy the effects of deformation on both objects in the contact. This formulation has been compared with independent FEM results for the radius of contact, the hardness and the contact force. The results have been compared and analyzed with the previous contact models (flattening and indentation). Finally, it has been shown that the new model appears to be in good agreement with the numerical simulations. It should be noted that our FE modeling could not converge for

deformations that result in $a/R > 0.5$, therefore we cannot verify either of the models for larger deformations.

Chapter 3

Experimental and numerical analysis of permanent deformation after normal impact

In this chapter a new expression for the permanent deformation after the impact of a rod with a flat surface is given. Both flat and the surface have been considered elastic-plastic. The contact has been considered frictionless and has been divided into three phases, the elastic, the elastic-plastic, and the unloading phase. For the normal impact force in the loading phase we considered a nonlinear expression that satisfies the effect of deformation on both objects by using a finite element model that was discussed in Chapter 2. For the unloading phase the contact force has been considered to follow the Hertz theory. The simulation and experimental results were conducted for different initial impact velocities of the rod. Permanent deformation after the impact and the motion of the rod has been measured accurately in the experiments. Based on the simulation and experimental results an expression for the permanent deformation has been developed. Finally, the model has been verified and compared with previous contact models in terms of the coefficient of restitution. The detail of the experimental setup and the analysis will be discussed in the following chapter.

3.1 Experiments

The experiments have been designed to study the motion and the permanent deformation during collision of a round end rod with an elastic-plastic flat. The motion of the rod before, during and after the impact was recorded by a high speed camera, and later analyzed using image processing techniques to measure the position and velocity of the rod during the phenomena. The deformed areas after the collision was scanned using a profilometer. The profile measurements was used to analyze the permanent deformation patterns during the

impact. The detail of the setup and measurement techniques are explained in the following sections.

3.1.1 Setup

The experiments have been designed in order to measure the motion of the rod and the permanent deformation of the flat after each impact. A round ended rod made of stainless steel with length $L = 304$ mm, diameter $D = 9$ mm and $m = 0.255$ kg with modulus of elasticity of $E_s = 212$ GPa and yield strength of $S_{ys} = 750$ MPa has been used. For the flat, carbon iron 1070 with a modulus of elasticity of $E_f = 200$ GPa and yield strength of $S_{yf} = 298$ MPa has been used (material properties provided by supplier). Figure 3.1 shows the schematic of the experimental setup. The impacting flat is fixed on a rigid table. A robotic arm is used to drop the rod vertically with a high accuracy and from different heights, H ranged from 0.2 to 1.45 m. Four lights, 1 000 W each, have been used in order to capture a clear image with little noise during the impact. A high speed camera capable of recording with 80 000, frames per second (fps) has been used to capture the motion of the rod before, during and after the impact. After each impact, the profile of the deformed region on the flat has been measured with a profilometer. The permanent deformation has been defined as the maximum depth in the deformed region. Each impact has been analyzed with two techniques: image processing and profilometery. A MATLAB program has been developed to analyze the experimental data for both phases.

3.1.2 Image processing

The image processing has been used to measure the real radius of curvature of the tip of the rod and the motion of the rod during each experiment. For the radius of curvature, a high resolution image has been captured and then analyzed with a MATLAB program. For the motion analysis, after some sample experiments, a frame rate of 80 000/s has been chosen to capture the motion. The recorded videos then have been analyzed with the image processing

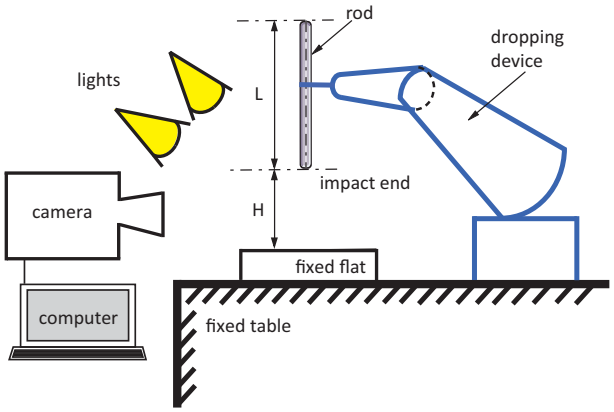

Figure 3.1: Sketch of the experimental setup.

techniques. It has to be noted that for high frame per second capture rates, the resolution of the high speed camera decreases significantly, which causes inaccuracies in the measurements. The out-of-plane motions of the rod tried to be eliminated by the consistent dropping device, robotic arm; however, existence of very small out-of-plane motions is possible.

Radius of Curvature

The real radius of curvature of the contact point on the rod is needed. A 12 mega pixel camera with a micro lens has been used to capture a clear image of the tip of the rod as is shown in Fig. 3.2a.

(a) (b)

Figure 3.2: (a) Original image from the tip of the rod. (b) Processed image of the tip of the rod.

The image with a pixel size of 24.7 μm has been analyzed in order to find the radius of curvature of the tip of the rod. First, the boundary of the rod has been found, shown by the continuous line in Fig. 3.2b. An 8th order polynomial has been fitted to the boundary, shown by the dotted line in Fig. 3.2b. The tip of the rod has been defined as the minimum

of the polynomial, shown by the diamond in Fig. 3.2b. The final radius of curvature has been calculated by averaging the radii of curvature around the tip. The order of the fitted polynomial can affect the radius measurements, to overcome this inaccuracies we have tried different polynomial orders from 4 to 12. for orders 6 to 10 we were measuring almost the same radius of curvatures, therefore we used 8th order for the final calculation. After averaging the values of 200 points (4.94 mm) around the tip, the radius of curvature has been calculated as 0.1365 m. The difference between the radius of the rod and radius of the curvature of the tip of the rod is the result of inaccuracies in the polishing process.

Motion Analysis

Each recorded movie contained about 1 000 frames, and each frame contained 512 $\times$ 48 pixels. An integer from 0 to 255 has been assigned to each pixel, called the gray value of each pixel. The value 0 refers to pure black, and 255 refers to pure white. In order to find the edges of the rod, a number for critical gray value has been used as the threshold between the rod and the background. To find this number, a certain frame during the impact has to be selected and analyzed. This frame has been called the critical frame. The critical frame has been defined as the frame when the rod is in contact with the flat, because the largest portion of the rod is in the frame. In order to find the critical frame, the distribution of the gray value in each frame has been calculated. Figure 3.3a shows the gray value distribution for all of the frames. The number of pixels with a gray value between 0 to 100 (the black background) is greater than the number of pixels with a gray value greater than 200, the rod. As the rod approaches the flat, more white pixels are seen in the frame, or in other words, the number of black pixels is decreasing. The critical frame has been defined as the frame with the minimum number of black pixels. The critical frame for the selected experiment was 426.

Figure 3.3b shows the gray value distribution of the critical frame and the gray values associated with the rod are in the range of 240 to 255. This range has been used to change

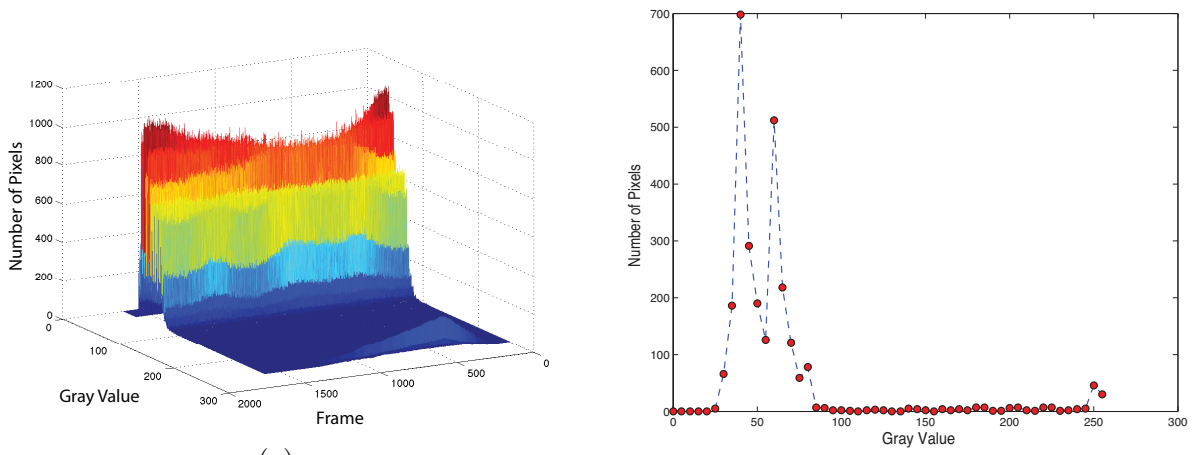

(a) (b)

Figure 3.3: (a) Gray value distribution for all of the frames. (b) Gray value distribution for critical frame.

the contrast of all the frames in the recorded video. Thus, the pixels with a gray value of more than 240 have been changed to pure white, and the pixels with a lower gray value have been changed to pure black. Figure 3.4 shows the same frame after image processing. Next

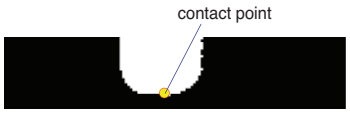

Figure 3.4: Processed image with the tracked contact point.

the processed image has been analyzed in order to check whether the rod was vertical during the impact or not and to calculate the velocity of the rod before and after the impact. The angle of the rod has been checked by analyzing the right and left edges of the rod for 20 frames before and 20 frames after the impact. The results showed that all of the impacts have an angle in the range of $90° \pm 5°$.

In order to calculate the velocity of the rod before and after the impact, a certain point on the rod has been tracked, as shown in Fig. 3.4. This point has been selected as the tip of the rod and it was the contact point. The position diagram of the contact point used to calculate the velocity of the rod is shown in Fig. 3.5. The minimum point of the position diagram represents the instant at which the rod and the flat are in contact. One should

note that the light diffraction around the edges of the rod causes inaccuracies in finding the exact boundary of the rod. However, while the light intensity for the range of the rod motion before and after the impact is considered constant, this wont affect the coefficient of restitution measurements.

For the sample experiment depicted in Fig. 3.5, the motion of the rod for 7.3 ms before impact (from the beginning to the minimum point) and 9.3 ms after the impact (from minimum to end) has been accurately captured. The velocities before and after the impact have been calculated from the slopes of the position diagram before and after the minimum point respectively.

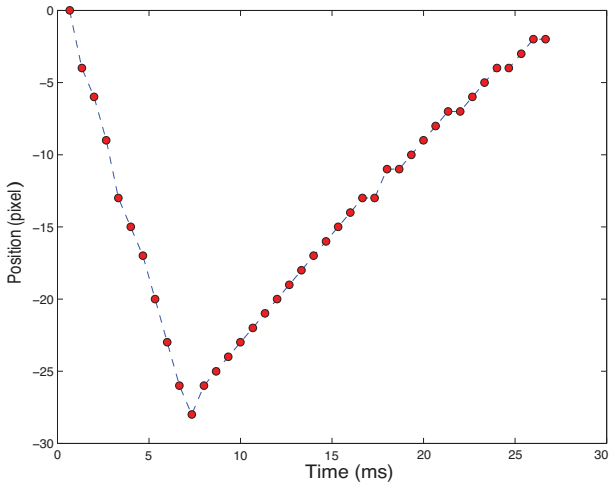

Figure 3.5: Position of the contact point before and after the impact; the dots show the position for every 40 frames.

3.1.3 Profilometeries

The flat and rod samples were well-polished before impact so that the average roughness of the flat was in the order of 10^{-2} of the permanent deformations after impact. After each impact, the profile of the deformed region has been measured with a profilometer. Figure 3.6a shows the 3D scan of the deformed area after one impact. The cross section of the deformed region has been used in order to measure the permanent deformation. A seventh order polynomial has been fitted using a MATLAB program on the cross section of the deformed

area as shown in Fig. 3.6b. The value of the minimum point of the polynomial has been selected as the permanent deformation. For this study 70 experiments were done for 18

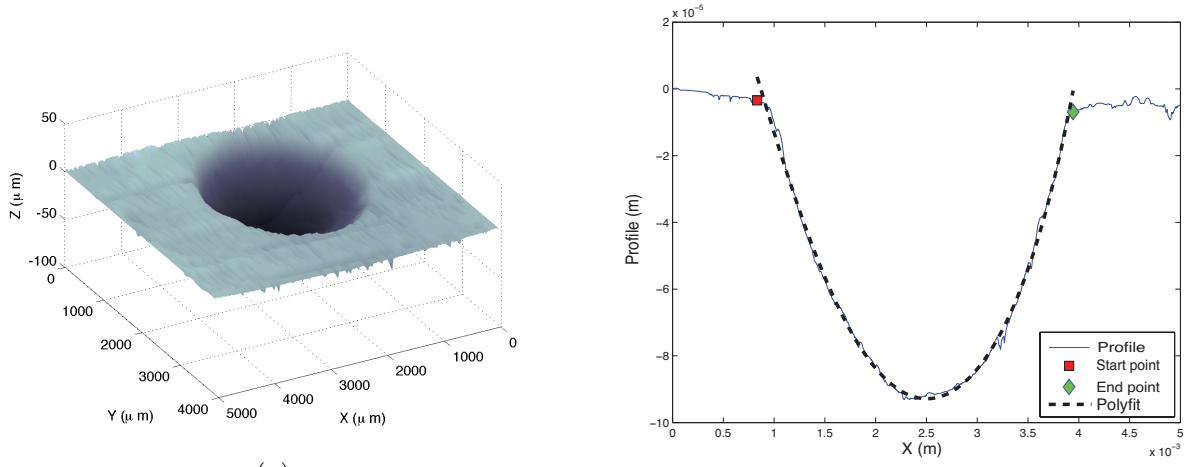

(a) (b)

Figure 3.6: (a) 3D scan of the profile after the impact. (b) the cross section of the profile after the impact.

different drop heights. The coefficient of restitution and the permanent deformation are calculated for each drop height by averaging data from at least 3 experiments. The surfaces have been polished with sand papers from score 60 to 1500, till the surface is mirror like. The profilometeries of the surfaces before impact have shown roughness around, $R_a = 0.4$ μm. Even though the roughness is much smaller than the permanent deformations after collision, it can be a cause of error in the measurements.

3.2 Formulation of the contact force

The contact during the impact has been divided into three phases: elastic, elasto-plastic and restitution. The impact starts with the elastic indentation of the rod into the flat. The elastic phase continues until yielding occurs, then the elastic-plastic phase starts and continues until the tip of the rod stops. At this moment there is the maximum indentation and the restitution phase starts. The restitution continues until there is no contact between the rod and the flat.

The contact force for the elastic phase has been considered to follow the Hertz theory [48]. For the contact force during the compression phase results from chapter two is used. The contact force during the restitution has been considered to be elastic and to follow the Hertz theory; however, during the restitution, because of the deformation of the flat and the rod, the geometrical properties of the profiles change. The contact force during the restitution depends on the maximum indentation during the loading phase and the permanent deformation of the flat after the impact. Therefore a new expression for permanent deformation has been developed and verified with experimental results. Each phase will be explained in detail in the following subsections.

3.2.1 Elastic Phase

Loading for the elastic phase has been considered to follow the Hertzian theory. Based on the JG model [54], the critical interference of elastic and elasto-plastic phases has been defined using a dimensionless indentation as

$$\delta^* = \frac{\delta}{\delta_y}, \tag{3.1}$$

where δ is the elastic indentation and δ_y is the indentation at which yield starts and can be calculated as

$$\delta_y = \left(\frac{\pi\, C\, S_y}{2\, E'}\right)^2 R, \tag{3.2}$$

with

$$C = 1.295\, e^{0.736\,\nu} \quad \text{and} \quad \frac{1}{E'} = \frac{1-\nu_{rod}^2}{E_{rod}} + \frac{1-\nu_{flat}^2}{E_{flat}},$$

where ν_{rod}, ν_{flat} are the Poisson ratios of the rod and the flat respectively, E_{rod}, E_{flat} are the moduli of elasticity of the rod and the flat, and S_y is the yield strength of the softer material, which in this study is the flat. Therefore the contact force for the elastic phase is calculated using the formula

$$P = K_1\, \delta^{3/2}, \tag{3.3}$$

where K_1 is given by

$$K_1 = \frac{4}{3} E' \sqrt{R}, \tag{3.4}$$

with

$$\frac{1}{R} = \frac{1}{R_{rod}} + \frac{1}{R_{surface}}.$$

However, as the $R_{surface}$ is infinite, $1/R = 1/R_{rod}$.

3.2.2 Elasto-plastic Phase

The elasto-plastic phase begins theoretically when $\delta^* = 1$ however, effectively begins from JG model with $\delta^* = 1.9$ and continues until the maximum compression. For the elasto-plastic phase the same axisymmetric FE model described in chapter 2 has been used. Figure 3.7a shows the FEA modeling for the material properties used in this study. The formulation presented in chapter 2 is used for the calculation of the contact force during the elastic-plastic regime.

Figure 3.8 shows the normalized contact force, F/F_y, as a function of normalized indentation δ/δ_y. Dots are representing the FEM results and the continuous line represents Eq. (2.38). The mean absolute error between FEM and Eq. (2.38) results is less than 1 % in the range of $0 < \delta_n < 2500$, which shows Eq. (2.38) works well for large deformations. The dashed line in Fig. 3.8 shows results from JG model. For the contact force shown in Fig. 3.8, at larger indentation the difference between the JG contact model and Eq. (2.38) increases.

3.2.3 Restitution

The unloading phase, or restitution, starts from the maximum compression when the vertical velocity of the rod is zero. The contact force for this phase has been considered to be elastic and follows the Hertz theory

$$P_r = K_{1r} \left(\delta - \delta_r\right)^{3/2}, \tag{3.5}$$

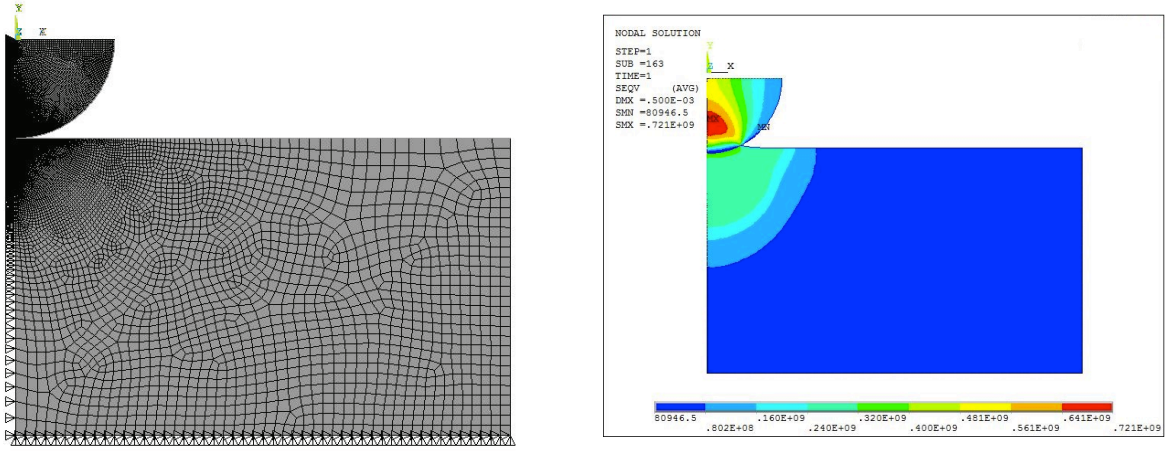

(a) (b)

Figure 3.7: (a) FEA modeling with fine mesh around the contact point and (b) stress distribution of the FEA model.

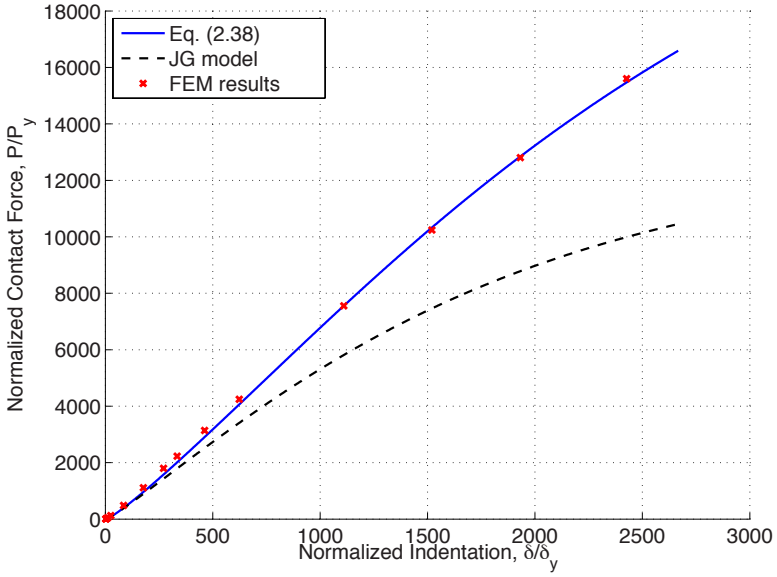

Figure 3.8: ANSYS results for contact force, red dots, and Eq. (2.38) results, continuous line.

where K_{1r} is given by Eq. (3.4). The radius of curvature changes according to [57]

$$R_r = \frac{1}{(\delta_m - \delta_r)^3} \left(\frac{3P_m}{4E'} \right)^2 , \tag{3.6}$$

where δ_m is the maximum indentation, δ_r is the permanent deformation and P_m is the contact force at the instant when restitution starts. Figure 3.9 shows the permanent deformation versus the maximum deformation on a logarithmic scale. The experimental data for the permanent deformation δ_r are different from the models in references [69, 28] and [54, 51, 78]. Using the experimental and FEM results an empirical expression for the permanent deformation, δ_r, is proposed

$$\frac{\delta_r}{\delta_m} = 0.8\left[1 - \left(\frac{\delta_m/\delta_c + 5.5}{6.5}\right)^{-2}\right] \tag{3.7}$$

There is a 4 % mean absolute error between the experimental data and Eq. (3.7). Thornton and Ning's model [108] and KK indentation model [71] predict greater values for δ_r. The KK indentation model with 20 % mean absolute error works better than KK and JG models as the material properties used in the experiments results in deformation that is closer to indentation models than the flattening models. The JG and the KE models show smaller values for the permanent deformations.

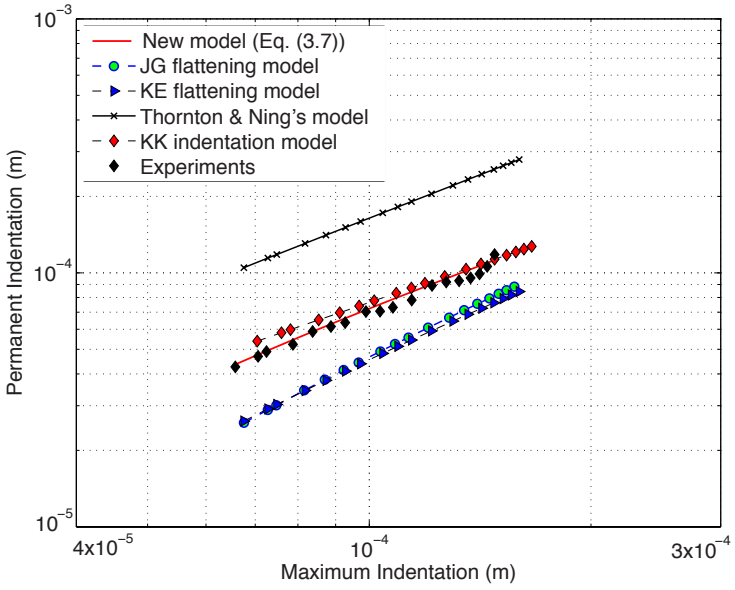

Figure 3.9: Logarithmic scale plot of permanent deformation, δ_r, vs. maximum indentation, δ_m, for different models.

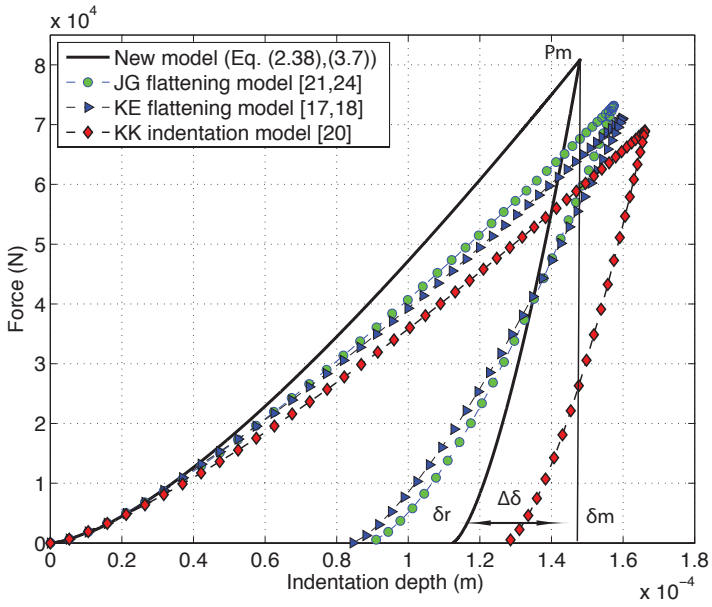

Figure 3.10: Force vs. indentation depth for the maximum experimented drop height.

3.3 Results and discussion

Figure 3.10 depicts the force-indentation results when the bar is dropped from a height of $H = 1.43$ m, which is the maximum drop height tested. For a maximum load of $F_m = 8.085 \times 10^4$ N the indentation is $\delta_m = 148$ μm. The restitution or unloading phase starts at this maximum indentation and continues to $\delta_r = 107$ μm with the vertical load $F \simeq 0$ N. Due to the deformation on both the flat and the sphere during the loading phase, the new model shows a larger force and smaller maximum indentation than the JG, the KE and the KK models. Even though, the material properties used is matching the indentation models, the JG flattening model is working better than the KK indentation model (Fig.3.10). The difference between the models for the maximum contact force during the loading is about 5 %. For the restitution phase, the new model shows a smaller difference between δ_m and δ_r, defined as $\Delta\delta$, as shown in Fig. 3.10. The difference between the flattening models and the KK model for δ_r is about 50 %. This substantial difference between the models for the loading and the unloading phase shows that the unloading phase plays a significant role.

Five different models, the JG model [54, 51, 57], the KE model [69, 28], the KK indentation model [71], Thornton and Ning's model [108] and the new model, developed in this paper, have been implemented. For each model there is a loading and an unloading phase. For the theoretical dynamics the differential equations of motion are:

$$m\mathrm{a_C} = \mathrm{F} - \mathrm{mg},$$
$$I_C\boldsymbol{\alpha} = \mathrm{r_{CE}} \times \mathrm{F_n},$$

where, m is the mass of the rod, $\boldsymbol{a}_C$ is the acceleration of the center of the mass, I_C is the mass moment of inertia, $\boldsymbol{r}_{CE}$ is the position vector from center of the mass, C, to the contact point, E, and $\boldsymbol{F}$ is the total normal contact force of the impact point. For the vertical impact, $\boldsymbol{r}_{CE} \times \boldsymbol{F}$ in the rotational equation of motion is neglected. The expressions that have been used for the contact force, F, are nonlinear. Therefore the equations of motion have been solved numerically using a Runge-Kutta integration method. The permanent deformation and the kinematic coefficient of restitution are calculated and analyzed using simulation and experimental results.

Each implemented model includes loading and unloading phases. For the JG model the formulation provided in [54] and [51, 57] have been used for the loading and unloading phases respectively. To implement the KE model, equations provided in [69] and [28] have been used for the loading and unloading phases respectively. Formulations in [71] have been used to implement the KK indentation model, and [109] has been used to implement Thornton and Ning's model.

Figure 3.11 shows the permanent deformation, δ_r, for different drop heights (different initial impact velocities) and different models. The experimental results start with δ_r = 42 μm for H = 0.20 m and gradually increase to δ_r = 118 μm for H = 1.43 m. Thornton and Ning's model shows 5 to 6 times greater values for δ_r. The KK indentation model shows 1.3 times greater values. The KE and JG models predict 1.5 to 2 times smaller values. The new model, Eq. (3.7) shows a good agreement with the experimental results.

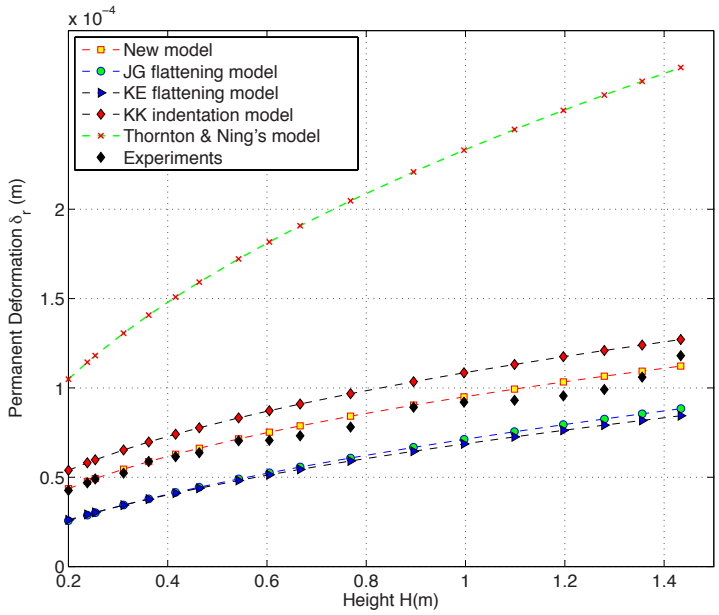

Figure 3.11: Permanent deformation, δ_r, for different models.

Figure 3.12 depicts the kinematic coefficient of restitution for different drop heights, H, from experiments and different models. The dropping height is ranging in 0.20 m< H <1.43 m. The experimental data shows a variation of the coefficient of restitution from $e = 0.56$ for $H = 0.2$ m to $e = 0.49$ for $H = 1.3$ m. The KE and the JG models show greater values for e. As the dropping height, H, increases the JG model is closer to the experimental results. The KK indentation model shows nearly constant coefficient of restitution equal to 0.46 in the experiments range, which is smaller than the experimental results. This difference between the models and the experimental results is coming from unloading phase as stated before in the descriptions for the Fig. 3.10. The new model predicts slightly larger values for the coefficient of restitution. The mean absolute error between the experimental results and the new model for the coefficient of restitution is less than 4 %. Thornton and Ning's model is not shown on the graph because of the large difference with the experimental results. The new model shows a better agreement with experimental results.

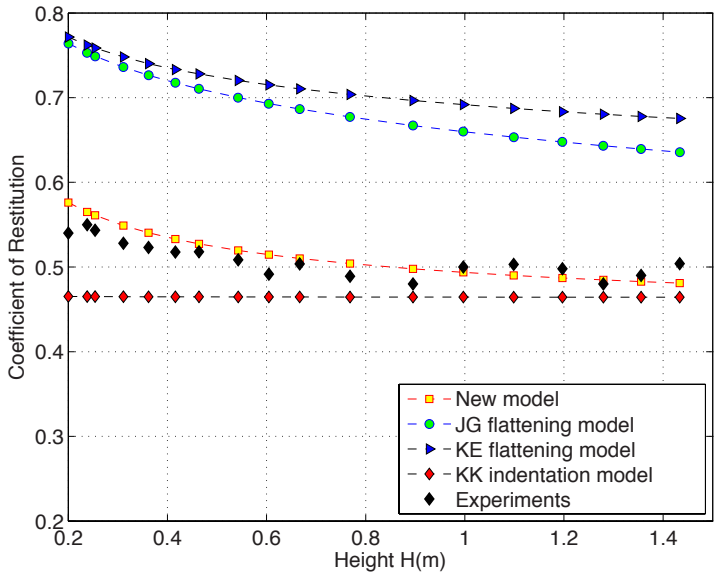

Figure 3.12: Kinematic coefficient of restitution for different models.

The unloading phase in the JG, KE and KK models have been updated with the new model unloading phase. The new expression for δ_r is used in all three models. Figure 3.13 depicts the permanent deformation as a function of dropping heights for the updated JG, KE, and KK models. The simulation results obtained from the updated models have been improved and are in good agreement with the experimental results. Both the JG and KE updated models show larger values for permanent deformation with mean absolute errors less than 10 %. As H increases the KE model begins to show better agreement than the JG model. The updated JG model shows slightly better agreement with the experiments than the KK model. The new model presented works better for the whole range with 2.5 % mean absolute error.

Figure 3.14 shows the kinematic coefficient of restitution for the updated models. In this case all updated models show better agreement with experiments and the mean absolute error for all models is less than 10 %. The JG and KK models are working better for small dropping heights and the KE and the new model are working better for the larger dropping height. The predictions have been significantly improved for all models. The new model

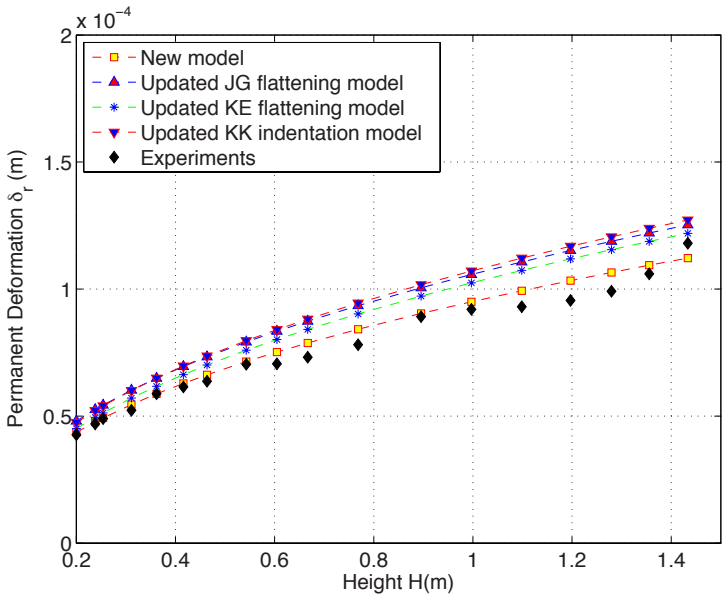

Figure 3.13: Permanent deformation, δ_r, for updated JG and KE models.

has overall better results for both permanent deformation and coefficient of restitution in the whole dropping height range. The comparison between the experimental results and the updated models verifies the new expression for δ_r for the case considered in this work.

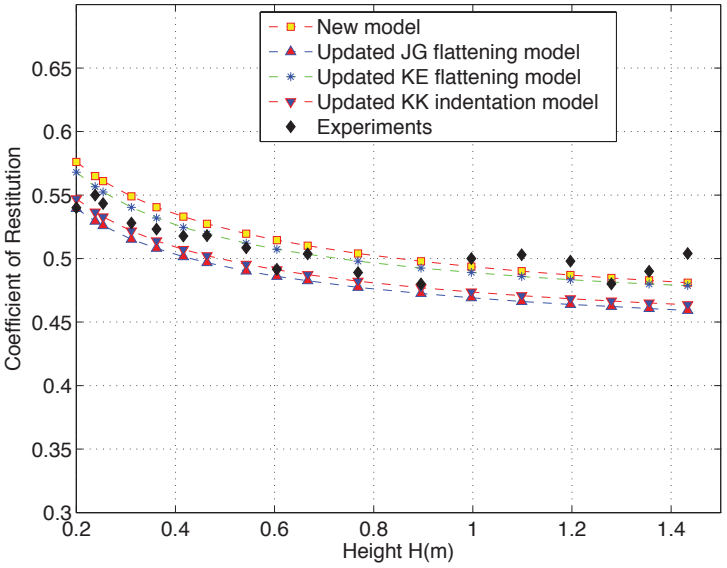

Figure 3.14: Kinematic coefficient of restitution for updated JG and KE models.

3.4 Conclusion

The presented new model includes the effect of deformation on both of the objects for the loading phase and a new empirical expression for permanent deformation after the impact of two elastic-plastic objects. The study provides accurate experimental results employed to compare different contact models in terms of permanent deformation and the kinematic coefficient of restitution. Although all of the models have been used and verified in many applications, to the best of our knowledge there is no experimental study of the permanent deformation. The current work provided accurate experimental results for permanent deformation and coefficient of restitution. Four models have been implemented and compared with experimental results. The new expressions for the permanent deformation appear to make better predictions than the previous approaches. The model is improved mostly due to its consideration of the flattening and indentation in the finite element model and also the new experimental expression for the permanent deformation after collision. The experimental results for the coefficient of restitution and the permanent deformation, verify the new model only for the considered material properties. The effect of strain rate during the impact might be important, but has been neglected in this study because the FEA results show a small area with high strain. To validate the proposed model, additional experimental results are needed for different link shapes, different material properties and different impact angles. In the next chapter we will be discussing the permanent deformation after the oblique impact of a round ended rod and an elastic-plastic flat.

Chapter 4

Numerical and experimental results for oblique impact

In this chapter, the elastic-plastic oblique impact of a rigid rod with an elastic-plastic flat has been analyzed experimentally and numerically. Nine different flattening and indentation contact models have been used to simulate the impact. The models have been compared theoretically in terms of the linear and the angular motion, the contact force during the impact, and the permanent deformation. A 3D infrared camera has been used in order to capture the motion of the rod before and after the impact. Experimental results for the coefficient of restitution and the rebound angular velocity have been compared with the presented models. Selecting the appropriate contact model is important on predicting the motion of the system for the simulations. For the impact angle $\theta = 45^\circ$ our previous model matches the experimental results. For the impact angle $\theta = 17.2^\circ$ it has been shown that all of the presented contact models show smaller values for coefficient of restitution and rebound angular velocity compare to the experiments.

4.1 Dynamics of the Oblique Impact

The equations of motion of a rod during the oblique impact were developed using Newton-Euler equations of motion. MATLAB has been used to find and solve the equations of motion. Because of the complexity and non-linearity of the contact force expressions, the equations of motion have been solved numerically using ODE45.

Figure 4.1 shows the schematic of the rod during the impact. The impact angle is θ. The center of the mass is point C , and the contact point is T. The gravitational force is $\vec{G}$, the normal force during the impact is $\vec{F}_{\mathrm{n}}$, and the friction force during the impact is $\vec{F}_{\mathrm{f}}$. The friction has been considered to be continuous.

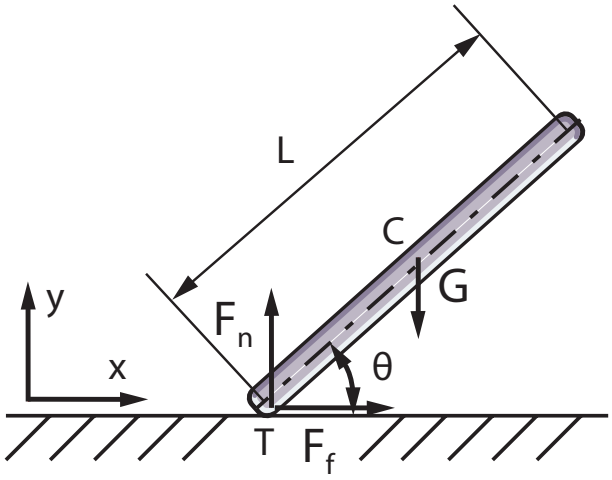

Figure 4.1: Schematic of the rod during the impact.

The position vector of the contact point T:

$$\vec{r}_{\mathrm{T}} = x\,\hat{\imath} + \delta\,\jmath, \tag{4.1}$$

where x is the tangential displacement of the contact point and δ is the normal deformation or indentation of the rod for flattening and indentation models respectively.

The position vector of the center of the mass of the rod:

$$\vec{r}_{\mathrm{C}} = [x\,\hat{\imath} + (\delta + R)\,\jmath] + \frac{L}{2}[\cos(\theta)\,\hat{\imath} + \sin(\theta)\,\jmath], \tag{4.2}$$

where the radius of the tip of the rod is R, and the length of the rod is L as shown in Fig. 4.1.

The angular velocity and acceleration can be written as:

$$\vec{\omega} = \dot{\theta}\,\hat{k} \quad , \quad \vec{\alpha} = \ddot{\theta}\,\hat{k}, \tag{4.3}$$

where ω is the angular velocity of the rod, and α is the angular acceleration of the rod.

The velocity of the center of the mass of the rod and contact point can be calculated as:

$$\vec{v}_{\mathrm{C}} = \frac{d\vec{r}_{\mathrm{c}}}{dt} \quad , \quad \vec{v}_{\mathrm{T}} = \vec{v}_{\mathrm{C}} + \vec{\omega} \times (\vec{r}_{\mathrm{T}} - \vec{r}_{\mathrm{C}}), \tag{4.4}$$

where $\vec{v}_{\mathrm{C}}$ is the velocity of the center of the mass of the rod, and $\vec{v}_{\mathrm{T}}$ is the velocity of the tip of the rod.

The acceleration of the center of the mass of the rod and contact point can be written as:

$$\vec{a}_{\mathrm{C}} = \frac{d^2\vec{r}_{\mathrm{c}}}{dt^2} \quad , \quad \vec{a}_{\mathrm{T}} = \vec{a}_{\mathrm{C}} + \vec{\alpha} \times (\vec{r}_{\mathrm{T}} - \vec{r}_{\mathrm{C}}) + \vec{\omega} \times [\vec{\omega} \times (\vec{r}_{\mathrm{T}} - \vec{r}_{\mathrm{C}})], \tag{4.5}$$

where $\vec{a}_{\mathrm{C}}$ is the acceleration of the center of the mass of the rod, and $\vec{a}_{\mathrm{T}}$ is the acceleration of the tip of the rod.

The equations of motion are:

$$m\,\vec{a}_{\mathrm{C}} = F_{\mathrm{n}}\,\hat{\imath} + (F_{\mathrm{f}} - m\,g)\jmath \quad , \quad F_{\mathrm{f}} = -\mu_{\mathrm{k}}\,F_{\mathrm{n}}\frac{\vec{v}_{\mathrm{T}}\hat{\imath}}{|\vec{v}_{\mathrm{T}}\hat{\imath}|}, \tag{4.6}$$

$$I_{\mathrm{C}}\,\vec{\alpha} = (\vec{r}_{\mathrm{T}} - \vec{r}_{\mathrm{C}}) \times (F_{\mathrm{n}}\,\hat{\imath} + F_{\mathrm{f}}\,\jmath), \tag{4.7}$$

where I_{C} is the mass moment of inertia about the center of the mass of the rod, F_{n} is the normal contact force, F_{f} is the friction force, and μ_{k} is the kinematic coefficient of friction.

The impact can be divided into two main phases: the compression and the restitution phase. The compression phase starts when the end of the rod touches the flat and continues until the contact point of the tip stops. At this point, the maximum deformation occurs, and the normal velocity of the tip of the rod is zero. The restitution phase starts at this instance and continues until the rod reaches the permanent deformation. At this instance the contact force is zero. The compression phase is divided into sub-phases depending on the contact model. Some models divide the compression phase into two sub-phases: the fully elastic and the elastic-plastic phase. Other models divide it into three sub-phases: the fully elastic, the elastic-plastic, and the fully plastic phase.

4.2 Contact force models ad formulations

In this section, different contact models are reviewed in detail. Different contact force expressions are provided for each model and each phase.

Two different flattening models are chosen and presented. The first formulation uses the Jackson-Green [54] modeling for the loading phase and Jackson's work in [51] for the unloading phase. This formulation will be called JG model in the rest of the chapter for simplification. The second formulation uses the Kogut-Etsion [69] model for the loading phase and Etsion et al. work in [28] for the unloading phase. This formulation is called KE model.

Three models have been chosen and used among indentation models. The first formulation uses the Kogut-Komvopoulos [71] (KK model) for the loading and unloading phase. The second formulation uses Ye-Komvopoulos [122] (YK model) formulation for the loading phase. Jackson's work in [51] is used for the unloading phase since this work doesn't provide a study for unloading phase. The third formulation uses Brake [14] contact model for the loading and unloading phases. In Brake's model it is not mentioned that the model is for indentation regime; however, the fully plastic formulation that has been used in the model is for indentation cases.

In chapter 3 we considered both the rod and the flat to be elasto-plastic. The model consists of the compression and restitution phases, the model will be called Ghaednia et al.. Moreover, Brake's model presented on 2012 [13], Stronge [104] and Thornton [108] models have been used for comparison.

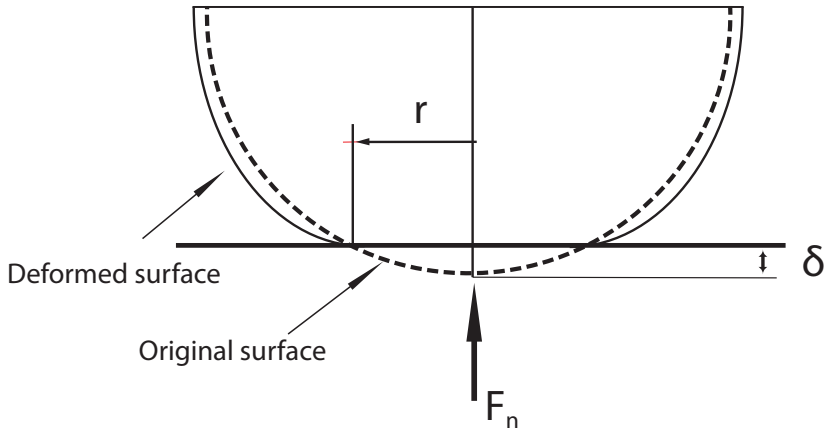

Figure 4.2: Schematic of the deformed objects for flattening contact models.

4.2.1 Hertzian Contact Theory

Most of the models are using the Hertzian theory [48] for the elastic phase and the restitution phase. The Hertzian theory uses the reduced modulus of elasticity and radius:

$$E^{-1} = \frac{1-\nu_1^2}{E_\mathrm{r}} + \frac{1-\nu_2^2}{E_\mathrm{f}},$$
$$\frac{1}{R} = \frac{1}{R_\mathrm{r}} + \frac{1}{R_\mathrm{f}},$$

where $R_\mathrm{r},\ E_\mathrm{r}$ and $R_\mathrm{f},\ E_\mathrm{f}$ are the radius and the modulus of elasticity of the rod and the flat respectively. $R = R_\mathrm{r}$ for our case since $R_\mathrm{f} = \infty$.

Using calculated R and E the contact force for the elastic phase of the contact, F_e, is calculated as follows:

$$F_\mathrm{e} = \frac{4}{3} E\, R^{0.5}\, \delta^{1.5}. \tag{4.8}$$

For the elasto-plastic phase of the contact each model has different expression for the contact force. The detailed formulation of the selected models will be given in the following sections of the paper.

4.2.2 JG Flattening Model

In the JG model the contact of an elasto-plastic deformable hemisphere with a rigid flat has been simulated in Fig. 4.2. The JG model [54] divides the loading phase into two sub-phases, the elastic and the elasto-plastic phase.

JG Elastic Phase

The elastic phase has been considered to follow the Hertzian [48] theory. It has been considered that the effective elasto-plastic phase starts at, $\delta^* \geq 1.9$ where

$$\delta^* = \frac{\delta}{\delta_{\rm y}} \quad , \quad \delta_{\rm y} = \left(\frac{\pi\, C_{\rm j}\, S_{\rm y}}{2\, E}\right)^2 R \quad , \quad C_{\rm j} = 1.295\, e^{0.736\nu}, \tag{4.9}$$

and $\delta_{\rm y}$ is the interference at which the yields starts and $S_{\rm y}$ is the yield strength of the weaker material. The elasto-plastic phase starts theoretically at $\delta^* = 1$, however effectively starts at $\delta^* = 1.9$ according to [54]. For the contact force in this phase, Eq. (4.8) is used.

JG Elastic-Plastic Phase

For the elastic-plastic phase the JG model considers the following formulation:

$$F_{\rm ep} = F_{\rm c}\left[e^{-0.25\,\delta^*)^{5/12}}\delta^{*1.5} + \frac{4\,H_G}{C_{\rm j}\,S_{\rm y}}(1 - e^{-0.04\,(\delta^*)^{5/9}}\delta^*)\right], \tag{4.10}$$

where

$$\begin{aligned} B = 0.14\, e^{23\,S_{\rm y}/\,E} \quad , \quad a &= \sqrt{R\,\delta_{\rm y}\left(\frac{\delta}{1.9\,\delta_{\rm c}}\right)^B}, \\ \frac{H_G}{S_{\rm y}} &= 2.84 - 0.92\left[1 - cos\left(\pi\frac{a}{R}\right)\right], \\ F_{\rm c} &= \frac{4}{3}\left(\frac{R}{E}\right)^2\left(\frac{\pi\, C_{\rm j}\, S_{\rm y}}{2}\right)^3. \end{aligned} \tag{4.11}$$

The average normal pressure is H_G, the critical force at the instant the yield occurs is F_{c}, and the contact force during the elastic-plastic phase is F_{ep}.

JG Restitution Phase

For the restitution phase of the JG model, Jackson's work in [51],[57] has been used. The restitution has been considered to be elastic and follows the Hertzian theory. The permanent deformation after the impact has been calculated from curve-fitting of the FEM analysis. The empirical formulation provided in [51] and [57] is as below:

$$\delta_{\mathrm{r}} = \delta_{\mathrm{m}} \left(1.02 \left[1 - \left(\frac{\delta_{\mathrm{m}}/\delta_{\mathrm{y}} + 5.9}{6.9} \right)^{-0.54} \right] \right), \tag{4.12}$$

where δ_{m}, is the maximum deformation at the end of the loading phase, and δ_{r} is the permanent deformation after the contact. It has been considered that the radius of curvature for the unloading phase is changing as below:

$$R_{\mathrm{r}} = \frac{1}{(\delta_{\mathrm{m}} - \delta_{\mathrm{r}})^3} \left(\frac{3\,F_{\mathrm{m}}}{4\,E} \right)^2, \tag{4.13}$$

where $F_{\mathrm{m}} = F_{\mathrm{ep}}\,(\delta = \delta_{\mathrm{m}})$. Using the new radius of curvature, R_{r}, and the permanent deformation, δ_{r}, the contact force for restitution phase is calculated as below:

$$F_{\mathrm{r}} = \frac{4}{3}\,E\,R_{\mathrm{r}}^{0.5}(\delta - \delta_{\mathrm{r}})^{1.5}. \tag{4.14}$$

4.2.3 KE Flattening Model

The KE model [69] has the same methodology as the JG model; however, the formulation is simpler.

KE Elastic Phase

The contact is elastic while $\delta/\delta_c \leq 1$, where δ_c can be calculated as:

$$\delta_c = \left(\frac{\pi K H}{2E}\right)^2 R, \tag{4.15}$$

$$K = 0.454 + 0.41\,\nu \quad , \quad H = 2.8\,S_y.$$

The KE model considered the hardness (average normal pressure) to be constant.

KE Elastic-Plastic Phase

The elastic-plastic phase has been divided into two sections. For small deformations $1 < \delta/\delta_c \leq 6$ the contact force expression is:

$$\frac{F_{ep}}{F_c} = 1.03\left(\frac{\delta}{\delta_c}\right)^{1.425} \quad , \quad F_c = F_e\left(\delta = \delta_c\right). \tag{4.16}$$

For large deformations $6 < \delta/\delta_c \leq 110$ the contact force expression is:

$$\frac{F_{ep}}{F_c} = 1.40\left(\frac{\delta}{\delta_c}\right)^{1.263}. \tag{4.17}$$

It has to be considered that for most of the impact problems δ/δ_c is larger than 110.

KE Restitution

Etsion et al.[28] model considers the restitution phase to be elastic-plastic and provides expressions for the permanent deformation after the contact and the contact force during the restitution:

$$\delta_r = \delta_m\left[1 - \left(\frac{\delta_m}{\delta_c}\right)^{-0.28}\right]\left[1 - \left(\frac{\delta_m}{\delta_c}\right)^{-0.69}\right], \tag{4.18}$$

$$F_m = F_{ep}\left(\delta = \delta_m\right) \quad , \quad F_r = F_m\left(\frac{\delta - \delta_r}{\delta_m - \delta_r}\right)^{1.5\left(\delta_m/\delta_c\right)^{-0.0331}}, \tag{4.19}$$

where the maximum interference is δ_{m}, and the maximum contact force during the impact is F_{m}.

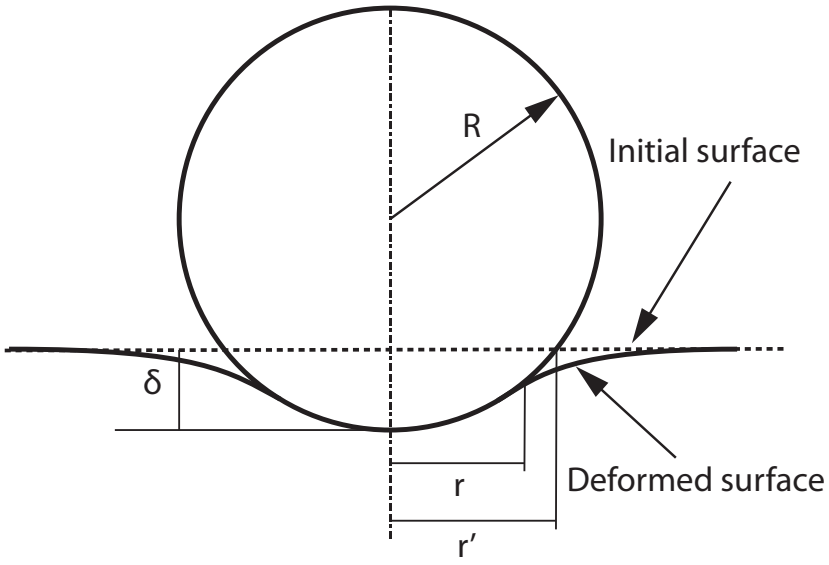

Figure 4.3: Schematic of the deformed flat for indentation contact models.

KK Indentation Model

For the indentation models δ is defined as the indentation of the rigid sphere in the flat as shown in Fig. 4.3. The formulations provided by KK model [71] are presented below.

KK Elastic Phase

The Elastic phase starts from $\delta = 0$ and continues until:

$$\frac{\delta}{r'} \leq \frac{1.78\, S_{\mathrm{y}}}{E},$$

where r' is shown in Fig. 4.3, E is the reduced modulus of elasticity defined in the Hertzian theory, and S_{y} is the yield strength of the flat. Using this criteria for the elastic phase the

contact force is:

$$\frac{F_{\mathrm{e}}}{a\,S_{\mathrm{y}}} = \frac{4\sqrt{2}}{3\pi}\left(\frac{E\,\delta}{S_{\mathrm{y}}\,r'}\right), \tag{4.20}$$
$$a = \frac{a'}{2} \quad , \quad a' = \pi\, r'^2 \quad , \quad r' = \sqrt{R^2 - (R-\delta)^2}.$$

KK Elastic-Plastic Phase

The elasto-plastic phase starts when $\delta\,/r' > 1.78\,S_{\mathrm{y}}\,/E$. The KK model suggests the following expression for the contact force:

$$\frac{F_{\mathrm{ep}}}{a'\,S_{\mathrm{y}}} = \frac{0.839 + \ln\left[(E\,/S_{\mathrm{y}})^{0.656}(\delta\,/r')^{0.651}\right]}{2.192 - \ln\left[(E\,/S_{\mathrm{y}})^{0.394}(\delta\,/r')^{0.419}\right]}. \tag{4.21}$$

KK Restitution Phase

The restitution phase has been considered to follow the Hertzian theory with the following expression for the permanent deformation:

$$\delta_{\mathrm{r}} = \delta_{\mathrm{m}}\,(1 - E_{R\delta}) \quad , \quad E_{R\delta} = 0.591\left(\frac{E}{S_{\mathrm{y}}}\right)^{-0.156}. \tag{4.22}$$

4.2.4 YK Indentation Model

The YK model [122] defines four different sub-phases for the contact: the elastic phase, small deformations, medium deformations, and large deformations. YK model defines Q as:

$$Q = \left(\frac{E}{S_{\mathrm{y}}}\right)\left(\frac{\delta}{r'}\right) \quad , \quad r' = \sqrt{R^2 - (R-\delta)^2}, \tag{4.23}$$

where r' is shown in Fig.4.3.

YK Elastic-Phase

The elastic phase starts at $Q = 0$ and continues until $Q < 1.78$. For elastic phase the contact force is formulated as:

$$\frac{F_{\mathrm{e}}}{a} = \frac{4\sqrt{2}}{3\pi}\, Q\, S_{\mathrm{y}} \quad , \quad a = \frac{a'}{2} \quad , \quad a' = \pi\, r'^{2}. \tag{4.24}$$

YK Elasto-Plastic Phase

For the small deformation when $Q \leq 21$, the contact force is defined as:

$$\frac{F_{\mathrm{ep}}}{a} = (0.7 \log Q + 0.66)\, S_{\mathrm{y}} \ , \tag{4.25}$$

$$\frac{a'}{a} = (0.05 \log Q^{2} - 0.57 \log Q + 2.41). \tag{4.26}$$

For the medium deformation when $21 < Q \leq 400$, the following formulation is provided:

$$\frac{F_{\mathrm{ep}}}{a} = 2.9\, S_{\mathrm{y}}. \tag{4.27}$$

Eq.(4.26) should be used to calculate a for the medium deformations.

For the large deformation when $Q > 21$, Eq.(4.27) is used with $a = a'/0.71$.

YK Restitution Phase

The YK model does not provide any governing equations for the restitution phase. Therefore, for the sake of the comparison we used the formulation provided by the JG model for the YK model.

4.2.5 Brake Indentation Model

Brake model [14] divides the contact into two phases, elastic and elasto-plastic phase. The elastic phase follows the hertzian theory and for the plastic phase Meyer's hardness

has been used. For the elasto-plastic phase transitionary functions have been proposed and showed that are matching the experimental results. The elasto-plastic phase in Brake's model [14] follows the Mayer's hardness model, therefore this model has been categorized in the indentation models.

Brake Elastic Phase

The Elastic phase starts from $\delta = 0$ and continues until $\delta \leq \delta_y$:

$$\delta_y = \frac{r}{F(\nu)} \left(\frac{\pi S_y}{2E} \right)^2, \tag{4.28}$$
$$F(\nu) = \max \left(-[1-\nu] \left[1 - \frac{z}{r} \tan^{-1}(\frac{r}{z}) \right] + \frac{3}{2} \frac{1}{1+(z/r)^2} \right)^2 \quad for \quad z \geq 0$$

Using this criteria for the elastic phase the contact force is calculated from Eq.(4.8).

Brake Elasto-Plastic Phase

The elastic-plastic phase starts when $\delta > \delta_y$. Brake propose the following equation for the contact force:

$$F = \text{sech} \left((1+\mathrm{n}_\epsilon) \frac{\delta - \delta_\mathrm{y}}{\delta_\mathrm{p} - \delta_\mathrm{y}} \right) \frac{4}{3} \mathrm{E} \sqrt{\mathrm{r}} \delta^{1.5} + \left(1 - \text{sech} \left[(1-\mathrm{n}_\epsilon) \frac{\delta - \delta_\mathrm{y}}{\delta_\mathrm{p} - \delta_\mathrm{y}}) \right] \right) \mathrm{P}_0 \pi \frac{\mathrm{a}^\mathrm{n}}{\mathrm{a}_\mathrm{p}^{\mathrm{n}-2}} \tag{4.29}$$

$$P_0 = H\, g\, 10^6, \quad H = \left(\frac{2}{H_s} + \frac{2}{H_f} \right)^{-1} \tag{4.30}$$

where $n_\epsilon = n - 2$, and n is Meyer's strain hardening components, H is Brinell's hardness and a_p can be calculated by solving the following nonlinear equation for the smallest positive root of δ:

$$a_p = \sqrt{2\delta R} = \left(\frac{3P_0}{4E} 2^{n/2} \pi r^{(n-1)/2} \delta^{(n-3)/2} \right)^{1/(n-2)},$$

and $\delta_p = a_p^2/2R$.

Brake Restitution Phase.

The restitution phase has been considered to follow the Hertzian theory with the following expression for the permanent deformation and radius of curvature for the unloading phase:

$$\delta_r = \delta_m \left(1 - \frac{F_m}{(4/3E)(\delta_m - \delta)^{1.5}}\right), \quad R_r = \frac{F_m^2}{(4/3E)^2(\delta_m - \delta)^3} \tag{4.31}$$

4.2.6 Ghaednia et al.

Ghaednia et al. model [34] uses the same formulation that was presented in chapter 2 and chapter 3.

4.3 Simulation results and comparison

Nine different contact models have been used in the simulations and compared for the linear and the angular motion during the impact and the permanent deformation. The material properties and the geometry in Table 4.1 are used for the simulations. Table 4.2 provides the legend used for comparison plots. The rod has round end and is impacting the flat with initial angle $\theta = 45°$ and $\theta = 17.2°$, zero initial tangential and angular velocity. The coefficient of friction has been calculated and averaged for all of the experiments at each angle using the following equation:

$$\mu = \frac{v_{\mathrm{Cf}}\hat{\imath} - v_{\mathrm{Ci}}\hat{\imath}}{v_{\mathrm{Cf}}\jmath - v_{\mathrm{Ci}}\jmath} \tag{4.32}$$

where v_{Ci} and v_{Cf} are the velocity of the center of the rod before and after the impact respectively. For the initial impact angle $\theta = 45°$ the coefficient of friction is $\mu = 0.13$ and for $\theta = 17.2°$ the coefficient of friction is $\mu = 0.2$.

Table 4.1: The material properties of the rod and the flat.

Rod (stainless steel AISI 201)		Flat (low-carbon iron AISI 1010)	
R	0.0088 (m)	t	0.03 (m)
L	0.3048 (m)	ρ	7870 (kg/m^3)
m	0.4607 (kg)	E_f	200 (GPa)
ρ	7800 (kg/m^3)	S_{yf}	305 (MPa)
E_r	200 (GPa)	H_f	105 (kgf/m^2)
S_{yr}	760 (GPa)	ν_f	0.3
H_r	327 kgf/m^2		
ν_r	0.3		

Figure 4.4 shows the normal displacement of the contact point during the impact. The loading phase starts at $t = 0$ s. For JG, Ghaednia et al., KE, KK, YK and Stronge models the loading phases continues to $t = 1.1 \times 10^{-4}$ s. Brake 2012, Brake 2015 and Thornton models are showing longer loading phase. At this point the normal displacement is minimum. The restitution phase starts at this instant. Stronge and Thornton models show minimum and maximum permanent deformations respectively. Thornton shows the longest impact duration among the other models. Besides the Thornton model Brake models are showing longer impact duration compare to the other models.

Figure 4.5 depicts the tangential displacement of the contact point during the impact. All of the models show same trend, while Thornton and Brakes models are slightly different from the other models. Brake 2012 models show the largest tangential displacements.

The normal velocity of the contact point during the impact is shown in Fig. 4.6. The initial normal velocity used in the simulation is $\vec{v}_i = -1\jmath$. There is a large difference between Thornton and the other models. When the normal velocity becomes zero, unloading phase starts, and all of the models give different results for this phase. The final rebound normal velocity calculated with Stronge's model is the largest comparing to other models. Brake 2012, Brake 2015 and KE models are showing nearly similar results. Thornton model shows the smallest value for the rebound velocity.

Table 4.2: The legend and equations used to depict the simulation results.

Legend	Name, equations and references
– – –■– – –	Jackson-Green (JG), Eqs.(4.(8-14))
– – –◆– – –	Ghaednia et al. (MJG), Eqs.(4.(8,32-34))
– – –●– – –	Kogut-Etsion (KE), Eqs.(4.(8,15-19))
– – –◀– – –	Kogut-Komvopoulos (KK), Eqs.(4.(20-22))
– – –▶– – –	Ye-Komvopoulos (YK), Eqs.(4.(14,23-27))
– – –▲– – –	Brake 2015 Eqs.(4.(8,28-31))
– – –✡– – –	Brake 2012
– – –★– – –	Stronge
– – –✳– – –	Thornton
✖	Experimental Results

Figures 4.7 and 4.8 present the tangential velocity and the angular velocity of the rod during the impact respectively. Similar to the normal velocity results Thornton model is different from the other models. For all of the models the tangential velocity starts at zero and decreases with an increasing rate till the maximum compression happens and then decreases with a decreasing rate till the end of the impact. Stronge shows the maximum rebound angular and tangential velocities. Other than the Thornton model, KK and YK are showing the minimum angular and tangential velocities. Thornton, Brake and Stronge models are showing longer impact duration.

Figure 4.9 represents the permanent deformation after the impact as a function of the initial impact velocity. The permanent deformation increases with the increase of the initial impact velocity with a same trend for all of the models. Thornton model is showing significantly larger permanent deformations than the other models. Besides the Thornton model, the Brake 2015 and Stronge models show the largest and smallest values for the permanent deformation.

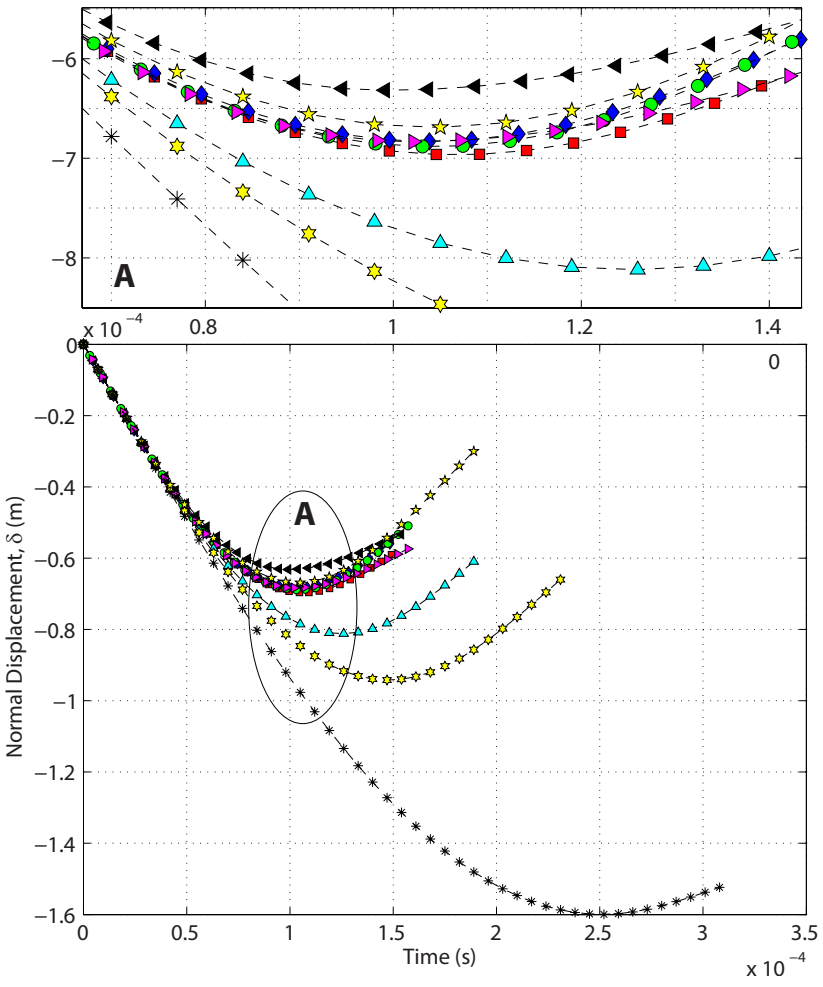

Figure 4.4: Normal displacement during the impact.

4.4 Comparison with the experimental results

The simulations and the experiments have been compared for the coefficient of restitution and the rebound angular velocity for initial impact angles, $\theta_i = 17.2°$, and $\theta_i = 45°$. In this work for the motion experimental results from Dr. Cermik dissertation has been used. The experimental results for the permanent deformation is the extension of Dr. Cermik's work, and is done by the author. It has to be considered that the material properties of the rod and the flat used for the experiments leads to an indentation regime (4.1). The kinematic coefficient of restitution is defined as the ratio between the rebound and the initial velocity

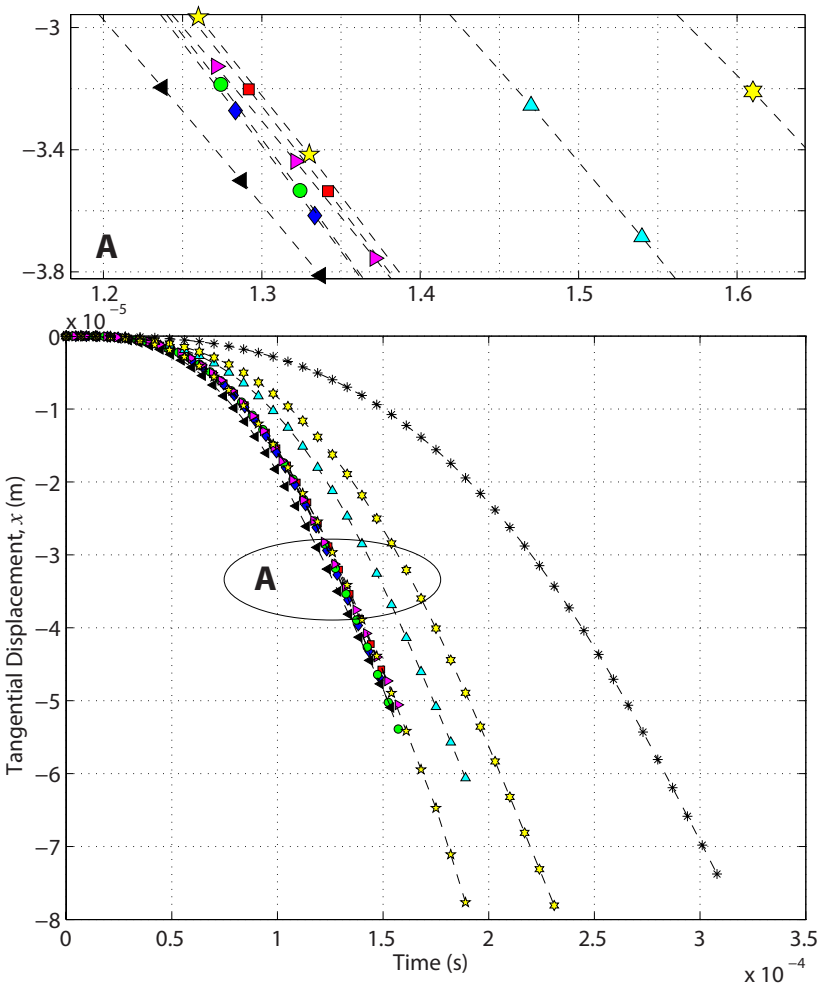

Figure 4.5: Tangential displacement during the impact.

at the contact point. The motion of the objects were measured using an OptoTrack 3020, which is high accuracy measurement error with error being 0.1 mm in a $2 \times 2 \times 2$ m space.

Figure 4.10 shows the coefficient of restitution as a function of the initial velocity for the contact models and the experiments. The experiments in this plot are performed for initial velocities from 0.5 to 4 m/s and initial impact angle, $\theta = 45°$. Experimental results are shown with black crosses. All of the models other than the Ghaednia et al. model show similar trend. For all of these models the coefficient of restitution is decreasing as the initial normal velocity increases. The experiments show nearly constant results for the coefficient of the restitution, $e \simeq 0.43$. The Ghaednia et al. model is in a good agreement with the

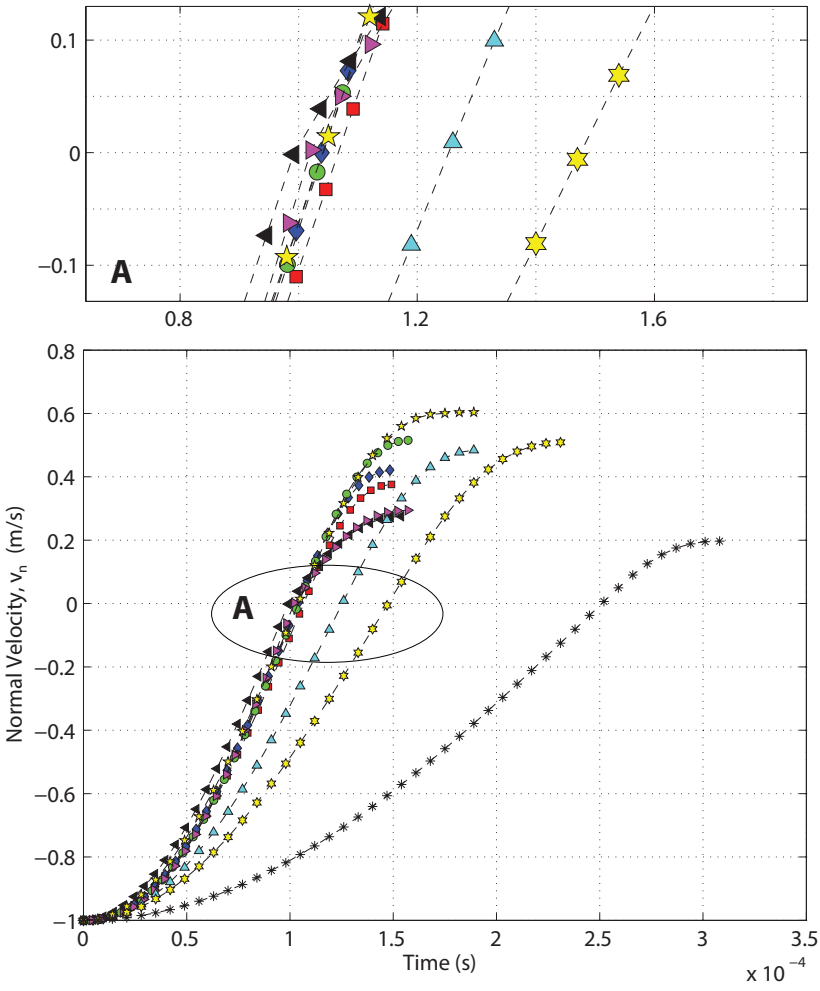

Figure 4.6: Normal velocity during the impact.

experimental results. The KE, Brake 2012, Brake 2015 and Stronge models are predicting larger values for smaller initial velocities and matching the experimental results for larger initial velocities. The JG, YK, and KK models predict smaller coefficient of restitution. The Stronge and Thornton models have the largest and smallest values respectively.

Figure 4.11 shows the rebound angular velocity as a function of initial impact velocity for $\theta = 45°$. The rebound angular velocity increases with the increase of the initial impact velocity. The Ghaednia et al. , KE, Stronge, Brake 2012 and Brake 2015 match the experiments for small initial velocities and show slightly smaller values for larger velocities. The JG, KK, YK and Thornton models show smaller values for the rebound angular velocities.

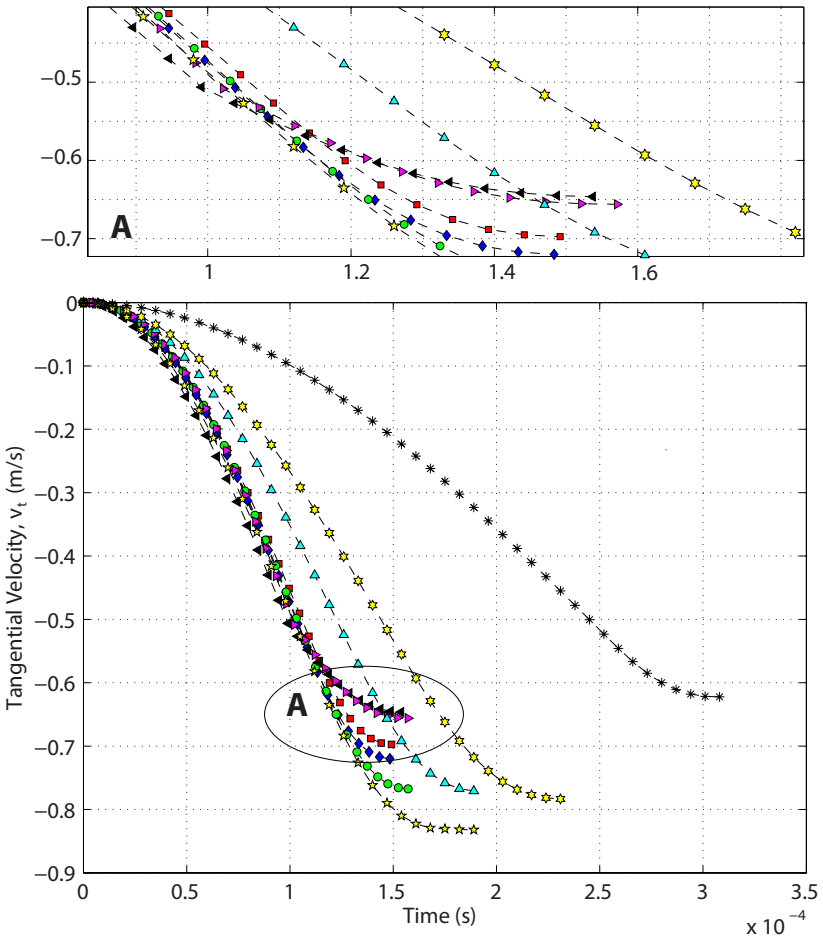

Figure 4.7: Tangential velocity during the impact.

Figure 4.12 shows the coefficient of restitution as a function of the initial velocity for the contact models and the experiments. The experiments are performed for initial velocities from 0.5 to 4 m/s and initial impact angle, $\theta = 17.2°$. Experimental results are shown with black crosses. Compare to the $\theta_i = 45°$ experiments (Fig.4.10), coefficient of restitution for $\theta_i = 17.2°$ shows larger values. All of the models other than the Ghaednia et al. model show similar trend. For all of these models the coefficient of restitution is decreasing as the initial normal velocity increases. The experiments show almost constant results for the coefficient of the restitution, $e \simeq 0.55$. The Ghaednia et al. model shows the same trend as the experimental data; however it shows smaller results. Overall non of the models matches

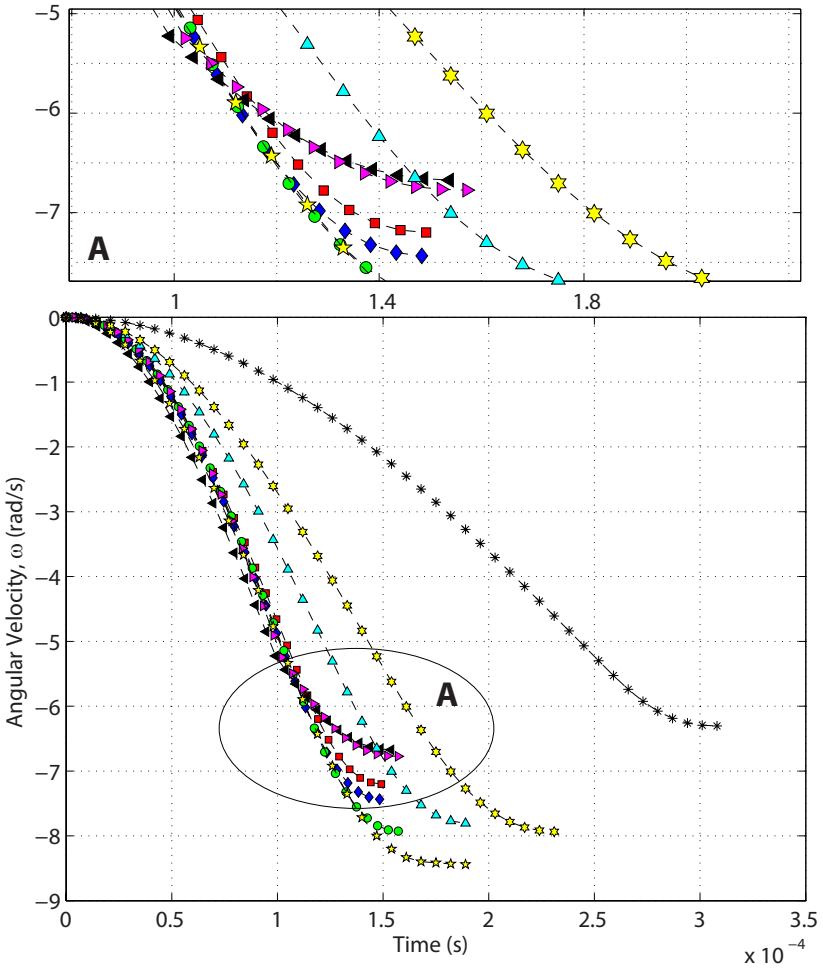

Figure 4.8: Angular velocity during the impact.

the experimental results in this case. Thornton and Stronge models similar to Fig. 4.10 show the smallest and largest results respectively.

Figure 4.13 shows the rebound angular velocity as a function of initial impact velocity. The rebound angular velocity increases with the increase of the initial impact velocity. All of the models show smaller values than the experimental results. Stronge and Thornton models are showing the maximum and the minimum results respectively.

Although, all of the models approximately show reasonable match with the experiments for motion analysis during the collision, when the models are compared with the experiments in case of permanent deformation, there is a significant difference between the predictions and the experiments. Figure 4.14 and Fig. 4.15 show the comparison between the experimental

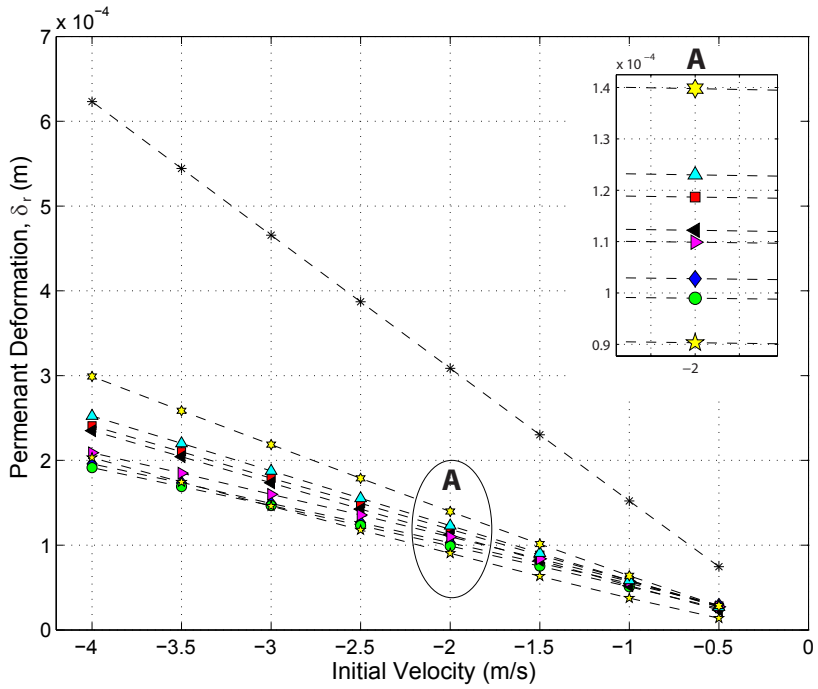

Figure 4.9: Permanent deformation after the impact.

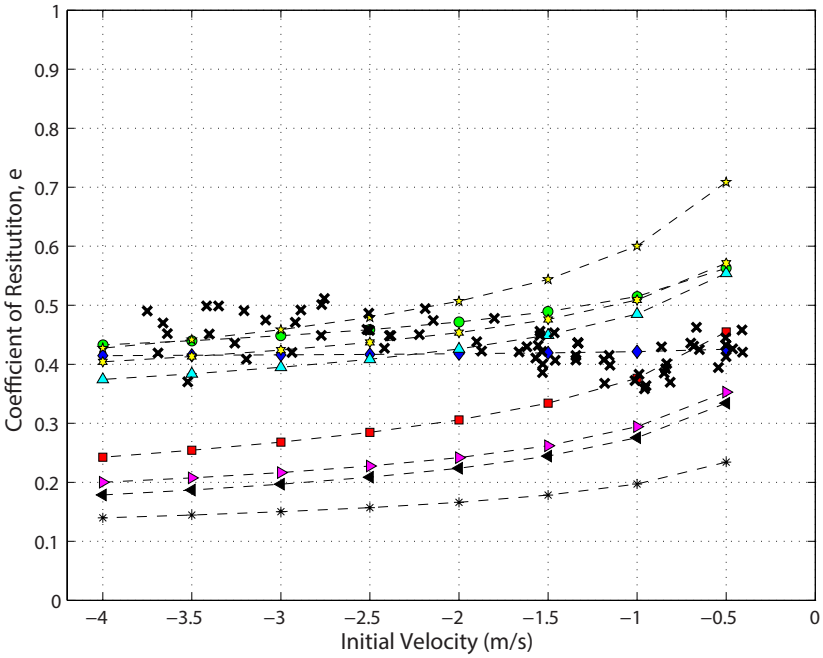

Figure 4.10: Comparison between the simulation and experimental results for the coefficient of restitution for $\theta = 45°$.

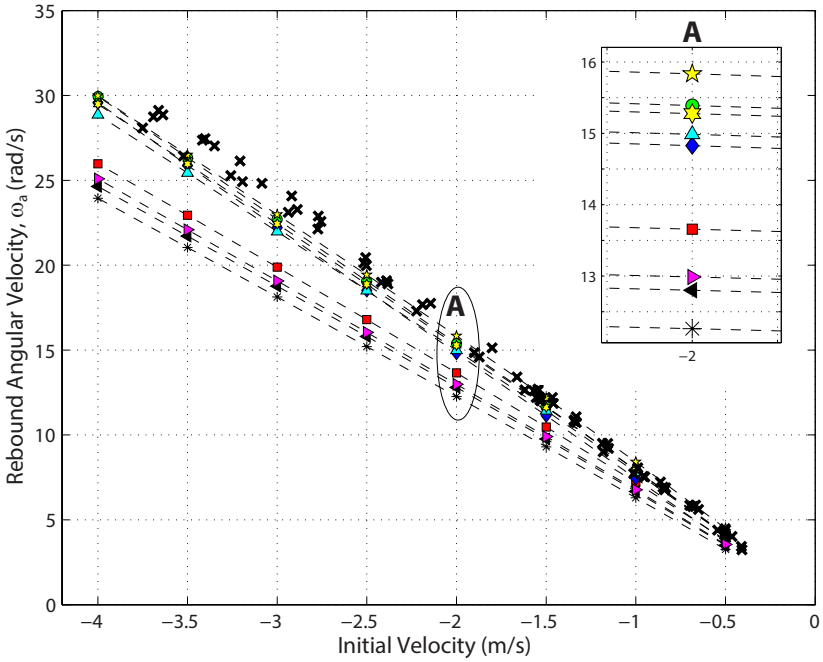

Figure 4.11: Comparison between the simulation and experimental results for the rebound angular velocity for $\theta = 45°$.

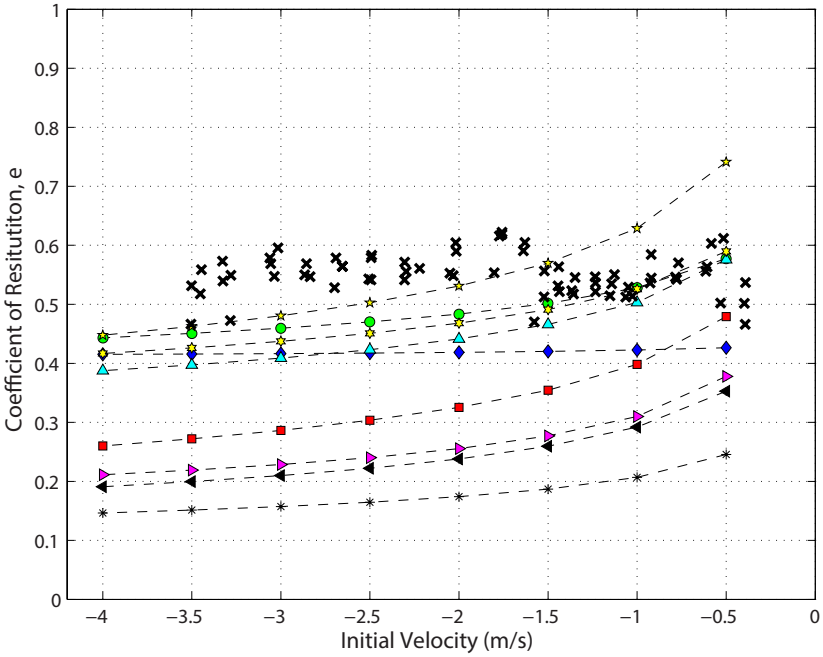

Figure 4.12: Coefficient of restitution as a function of initial impact velocity for $\theta = 17.2°$.

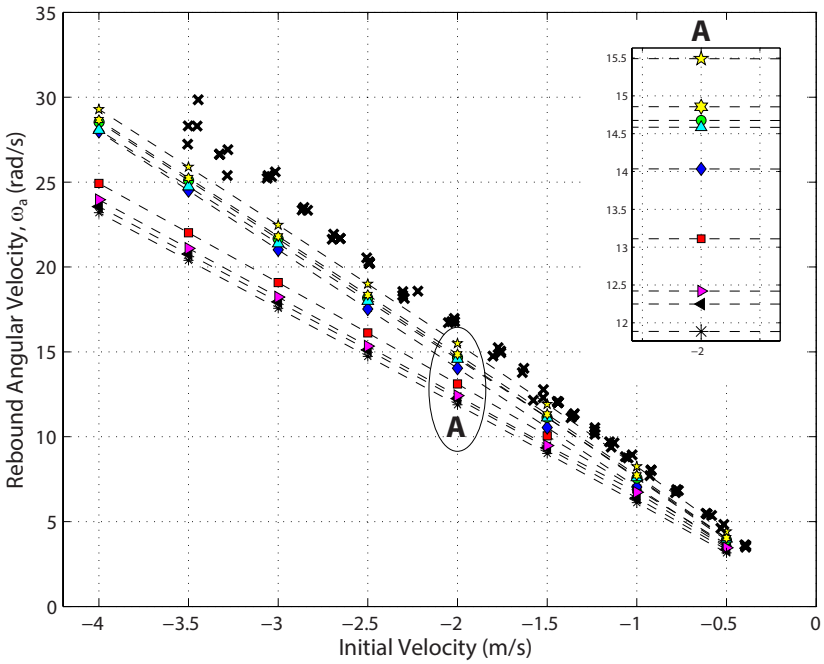

Figure 4.13: Rebound angular velocity as a function of initial impact velocity for $\theta = 17.2°$.

results and the numerical prediction for permanent deformation after impact with $\theta = 45°$ and $\theta = 17.2°$ respectively. For both impact angles the experiments show significantly smaller values, which shows that there is a miss understanding of the behavior of contact force during the oblique impact. The smaller permanent deformations show that the normal force during the impact should be very smaller that what is predicted in the simulations.

4.5 Conclusions

In this study, the dynamic of the oblique impact of a rod with a flat has been analyzed experimentally and theoretically. The motion of the rod during the impact has been analyzed. The linear and angular motion of the rod has been calculated for five different contact models. The permanent deformation plays an important role for all the models. Selecting the appropriate contact model is very important and gives different results especially for the unloading phase. The coefficient of restitution and the rebound angular velocity calculated from the experiments with impact angles, $\theta = 45°$ and $\theta = 17.2°$ are compared with the

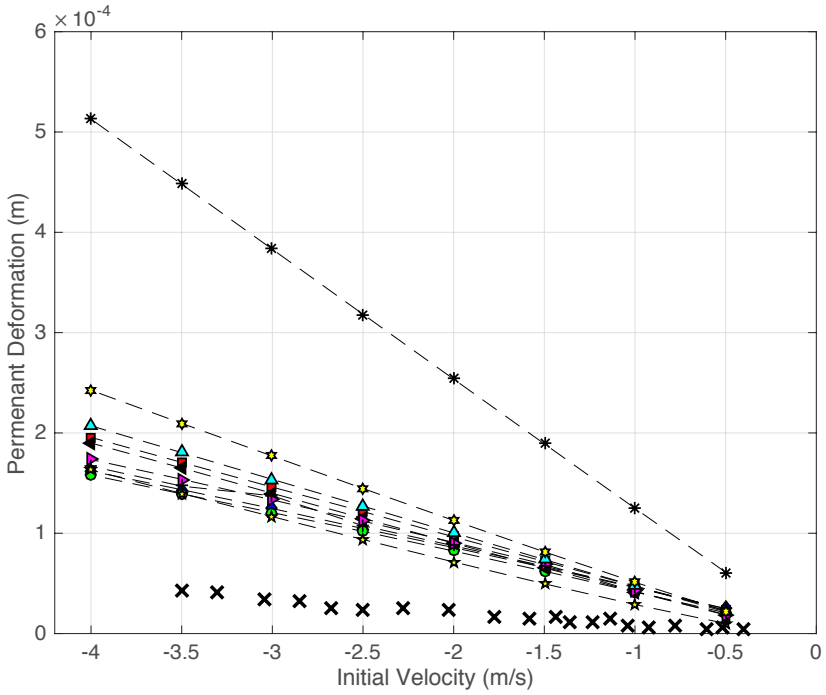

Figure 4.14: Permanent deformation after impact as a function of initial impact velocity for $\theta = 45°$.

simulations using different contact models. The experimental results lead to larger deformations than the previous experimental studies such as Kharaz's works [68][67], which help us to compare the contact models for more realistic situations when plastic deformation are dominating.

It has been shown that for the impact angle, $\theta = 45°$ our previous work, Ghaednia et al. [34] matches the experimental results for both the coefficient of restitution and rebound angular velocity. Stronge and Brake models also show good agreements with the experimental results. For the impact angle, $\theta = 17.2°$ it has been shown that all of the presented contact models are predicting smaller values for both the coefficient of restitution and the rebound velocity compare to the experimental results.

When comparing the numerical solution of the contact models for permanent deformation, there is a significant difference between the predictions and the experiments. The experiments show significantly smaller values, which shows that the normal contact force

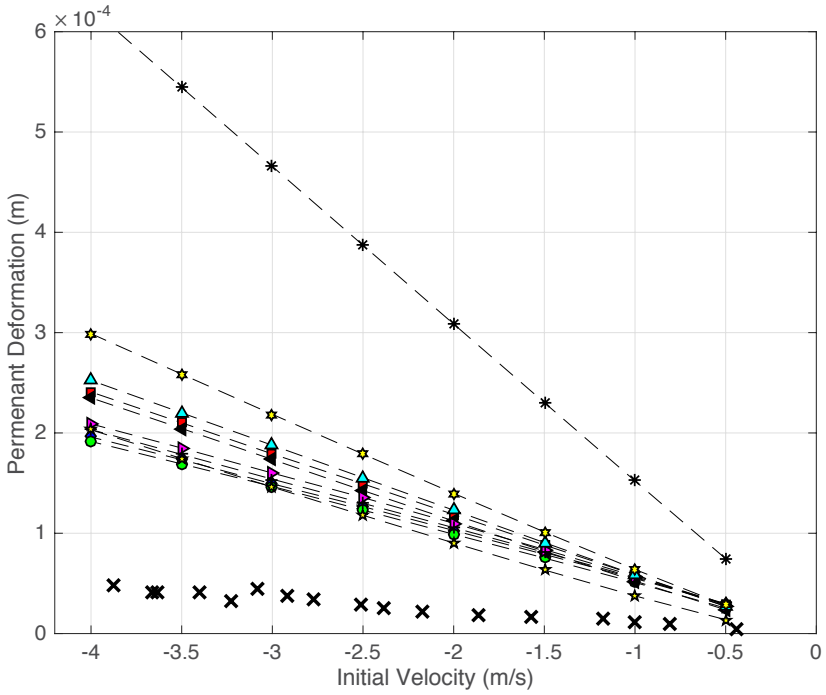

Figure 4.15: Permanent deformation after impact as a function of initial impact velocity for $\theta = 17.2°$.

during the oblique impact has been reduced significantly compare to the normal impact that was discussed in chapter 3. This phenomena has not been seen before and needs extra attention to be answered. In the next chapter we will try to address this issue and propose a simple solution for practical uses.

Chapter 5

Analytical study of the permanent deformations after oblique impact

In this chapter the displacements during the oblique impact of a rigid rod with a deformable flat has been studied. A new approach has been developed in order to relate the impact duration, the normal permanent deformation and the sliding length during the impact. The theoretical and numerical results have been compared. An experimental setup was built to measure the motion of the rod before and after the impact. The deformation region after the impact was scanned and measured. Using the experimental results and the calculated impact duration the average normal contact force was calculated. It has been shown that the presented approach yields to more accurate results compare to direct integration of equations of motion using quasi-static contact models.

5.1 Mathematical solution

In this section a formulation is developed to relate the impact duration to the normal permanent deformation and the sliding length. Figure 5.1 shows the schematic of the problem a rigid rod with the length, L, impacting a massive surface at an angle θ. The rod has semi-spherical ends with the radius, R. The contact point between the rod and the surface is T and the center of mass is noted by C. The position vectors then can be calculated as:

$$\theta(t=0) = \theta_i$$

$$\vec{r}_T = 0\ \hat{\imath} + 0\ \jmath, \quad \vec{r}_C = \frac{L}{2}\cos(\theta_i)\ \hat{\imath} + \left(\frac{L}{2}\sin(\theta_i) + R\right)\ \jmath$$

$$\vec{v}(t=0) = 0\ \hat{\imath} + v_i\ \jmath, \quad \vec{\omega}(t=0) = \omega_i\ \hat{k}$$

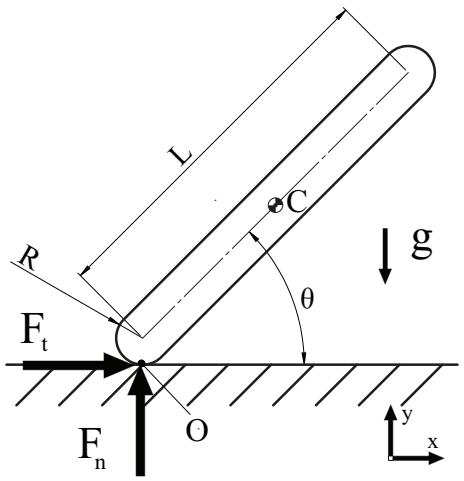

Figure 5.1: Schematic of the rod during the impact.

During the impact, the velocity of the center of the mass is:

$$\vec{v}_C = \vec{v}_{iC} + \frac{1}{m}\int_0^t \vec{F}dt = \frac{1}{m}\int_0^t F_x dt\ \hat{\imath} + \left(v_i + \frac{1}{m}\int_0^t F_y dt\right)\ \jmath \tag{5.1}$$

And the angular velocity can be calculated as:

$$\vec{\omega} = \frac{1}{\mathrm{I_C}}\int_0^t \vec{M}dt = \frac{1}{\mathrm{I}}\left(\frac{L}{2}\sin\theta + R\right)\int_0^t F_x dt - \frac{L\cos\theta}{2I}\int_0^t F_y dt \tag{5.2}$$

it has been assumed that $\theta = \text{const.}$ during the impact. Using Eqs.(5.1, 5.2) velocity of the tip of the rod is:

$$\vec{v}_T = v_{Tx}\ \hat{i} + v_{Ty}\ \hat{j} = \vec{v}_C + \vec{\omega}\times\vec{r}_{CT} \tag{5.3}$$

$$v_{Tx} = \left(\frac{1}{m} + \frac{1}{\mathrm{I}}\left[\frac{L}{2}\sin\theta + R\right]^2\right)\int_0^t F_x dt - \frac{L\cos\theta\left(\frac{L}{2}\sin\theta + R\right)}{2\mathrm{I}}\int_0^t F_y dt \tag{5.4}$$

$$v_{Ty} = v_i - \frac{L\cos\theta\left[\frac{L}{2}\sin\theta + R\right]}{2\mathrm{I}}\int_0^t F_x dt + \left(\frac{1}{m} + \frac{L\cos\theta}{4\mathrm{I}}\right)\int_0^t F_y dt \tag{5.5}$$

Assuming that

$$\int_0^t F_x dt = \mu\int_0^t F_y dt \tag{5.6}$$

where μ is the average coefficient of friction during impact, and yields to:

$$v_{Tx} = \left(\left[\frac{1}{m} + \frac{(L\sin\theta + R)^2}{4\mathrm{I}} \right] \mu - \frac{L\cos\theta \left(\frac{L}{2}\sin\theta + R \right)}{2\mathrm{I}} \right) \int_0^t F_y dt \tag{5.7}$$

$$v_{Ty} = v_i + \left[\frac{1}{m} + \frac{(L\cos\theta)^2}{4\mathrm{I}} - \frac{L\cos\theta \left(\frac{L}{2}\sin\theta + R \right)}{2\mathrm{I}} \mu \right] \int_0^t F_y dt \tag{5.8}$$

Using Eq.(5.8) the normal permanent deformation after the impact can be calculated:

$$\delta_p = \int_0^T v_{Ty} dt = \int_0^T v_i dt + \left[\frac{1}{m} + \frac{(L\cos\theta)^2}{4\mathrm{I}} - \frac{\left(\frac{L}{2}\sin\theta + R \right)}{2\mathrm{I}} \mu \right] \int_0^{t_f} \int_0^t F_y dt \tag{5.9}$$

Therefore

$$\int_0^T \int_0^t F_y dt = \frac{\delta_p - v_i T}{\left[\frac{1}{m} + \frac{(L\cos\theta)^2}{4\mathrm{I}} - \frac{\left(\frac{L}{2}\sin\theta + R \right)}{2\mathrm{I}} \mu \right]} \tag{5.10}$$

where δ_p is the normal permanent deformation and T is impact duration. Using Eqs.(5.7, 5.10) the sliding length, L_s can be found:

$$L_s = \int_0^{t_f} v_{Tx} dt = -\alpha(\delta_p - v_i T) \tag{5.11}$$

where α is:

$$\alpha = \frac{\left[\frac{1}{m} + \frac{(L\sin\theta + R)^2}{4\mathrm{I}} \right] \mu - \frac{L\cos\theta \left(\frac{L}{2}\sin\theta + R \right)}{2\mathrm{I}}}{\left[\frac{1}{m} + \frac{(L\cos\theta)^2}{4\mathrm{I}} - \frac{\left(\frac{L}{2}\sin\theta + R \right)}{2\mathrm{I}} \mu \right]} \tag{5.12}$$

5.2 Experiments

The experimental setup is designed to perform consistent drops of a stainless steel rounded end rod on a carbon iron flat (material properties and geometry of the rod and the flat are provided in Tab. 5.1). Setup provides desirable initial angle, zero tangential and angular velocity. Figures 5.2(a), 5.2(b) show the schematic of the experimental setup from the right and front views respectively. Two solenoids have been used to grab and release the

rod with a manual trigger. The initial angle of the drop can be changed continuously from 0 to 90 degree. The flat is clamped to a massive table.

Table 5.1: The material properties and geometry of the rod and the flat.

Rod (stainless steel AISI 201)		Flat (low-carbon iron AISI 1010)	
R	0.0088 (m)	ρ	7870 (kg/m^3)
L	0.3048 (m)	E_f	200 (GPa)
m	0.4607 (kg)	S_{yf}	305 (MPa)
ρ	7800 (kg/m^3)	H_f	105 (kgf/m^2)
E_r	200 (GPa)	ν_f	0.3
S_{yr}	760 (GPa)		
H_r	327 kgf/m^2		
ν_r	0.3		

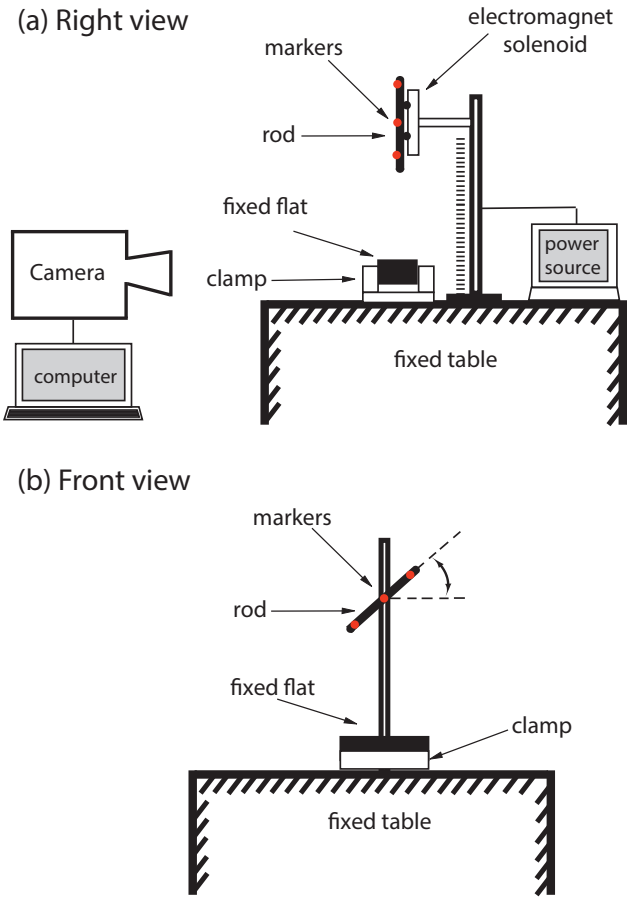

Figure 5.2: (a) Sketch of the experimental setup, right view. (b) Front view.

A high speed 3D infrared camera (Optotrak) is used to track the motion of three markers attached to the rod with 500 fps. The position of the markers used to calculate the velocity of the center of the rod before and after the impact. Using the velocities from experiments and Eq. (5.6), the average coefficient of friction during the impact is measured using the following equation:

$$\mu = \frac{\int_0^T F_x dt}{\int_0^T F_n dt} = -\frac{v_{Cx}(t=T) - v_{Cx}(t=0)}{v_{Cy}(t=T) - v_{Cy}(t=0} \tag{5.13}$$

The deformed areas after the impact have been marked and the profiles of the deformed areas have been scanned using an optical profilometer. In the profilometeries, the distance between the scanned points in X and Y directions was 3 μm and the resolution in the Z direction was 20 nm. The results from the profilometer model have been used to measure the normal permanent deformation and the sliding length.

5.3 Results and Discussion

The results are studied for three different impact angles, $\theta = 20°, 45°, 70°$. Using the scanned profiles the normal permanent deformations and the sliding lengths are measured. The normal permanent deformation is defined as the maximum depth of the deformed area and the sliding length is defined as the maximum length of the deformed area minus the width of the deformed area at the maximum deformation depth. The deformation patterns after the impact for the numerical simulations have been compared with the experiments and big differences can be seen. Position of three markers on the rod are tracked and used to find the linear and angular velocities of the rod before and after the impact.

5.3.1 Deformation Patterns

In this section the permanent deformation patterns for analytical, numerical and experimental solutions have been analyzed. For the analytical solution effect of α on the

deformation patterns has been mentioned. For experiments the e, δ_p and L_s have been measured for 3 cases with $\theta_i = 20°, 45°, 70°$. Numerical solutions have been performed to compare with experiments and analytical solutions.

Analytical solution

In the analytical solution α (see Eq. (5.12)) is a constant, which is a function of the geometry and the friction coefficient, and relates the sliding length to the normal permanent deformation. In Eq. (5.11), $\delta_p \leq 0$, $v_i \leq 0$ and $T \geq 0$. As $|v_n(t)| \leq |v_i|$ then $|\int_0^T v_n dt| \leq |v_i T|$, therefore $|\delta_p| = |\int_0^T v_n dt| < |v_i T|$ and yields to $(\delta_p - v_i T) \geq 0$. This shows that the sign of α uncovers the sliding direction. Figure.5.3 shows the change of α with respect to the initial impact angle for different friction coefficients (Information provided in Table. 5.1 is used to develop Fig. 5.3). It has to be considered that in the real problems the average coefficient of friction is changing with the initial impact angle but in Fig.5.3, $\mu = \text{const.}$.

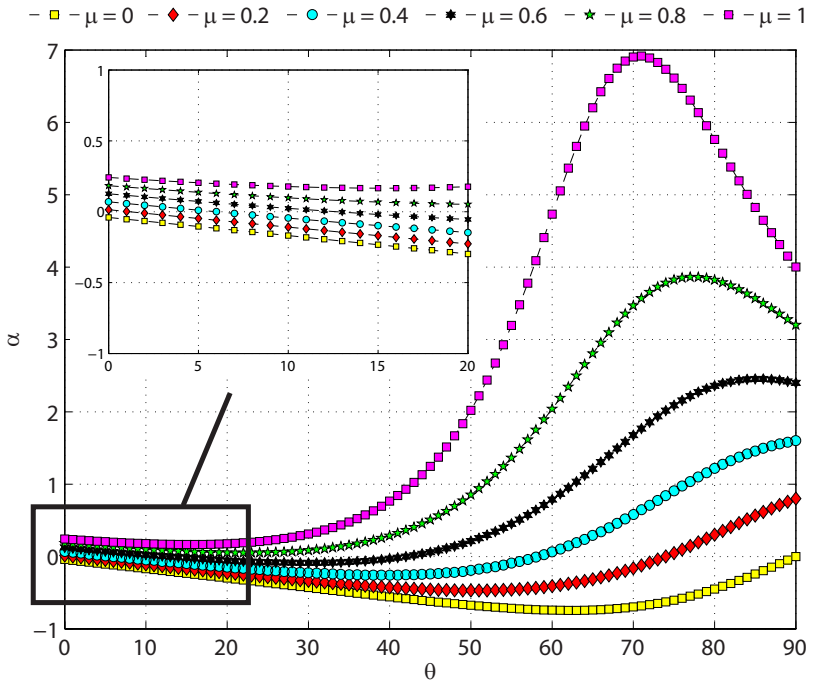

Figure 5.3: α vs. θ for different friction coefficients, Eq. (5.12) is used with table. 5.1 to calculate alpha for this figure.

It can be seen in Fig. 5.3 that sign of α changes for large impact angles, θ. Change in the sign here shows that the friction changes from sliding to sticking. This phenomenon is happening because at higher impact angles the friction force applies a larger moment than the normal force. More interestingly it can be seen that for coefficient of friction, $\mu > 0$, the change in sign of α also happens for small impact angles. Therefore for small angles sticking region can be seen as well as very large angles. For larger coefficient of frictions, μ, the sticking region is larger both for the small and large impact angles. For $\mu = 1$ it can be seen that the impact is always in the sticking region, which is expected.

Experiments

Deformation patterns for three different impact angles, $\theta = 20°,\ 45°,\ 70°$ have been scanned using the optical profilometer. For $\theta = 20°$ the rod has been dropped with initial velocity, $\vec{v}_i = -1.41\jmath$ m/s. The normal velocity of the tip of the rod is, $v_{fT} = 0.71$ m/s, therefore the coefficient of restitution is $e = 0.5$. The average friction coefficient is measure from the experiments using Eq. (5.13) and is, $\mu = 0.20$.

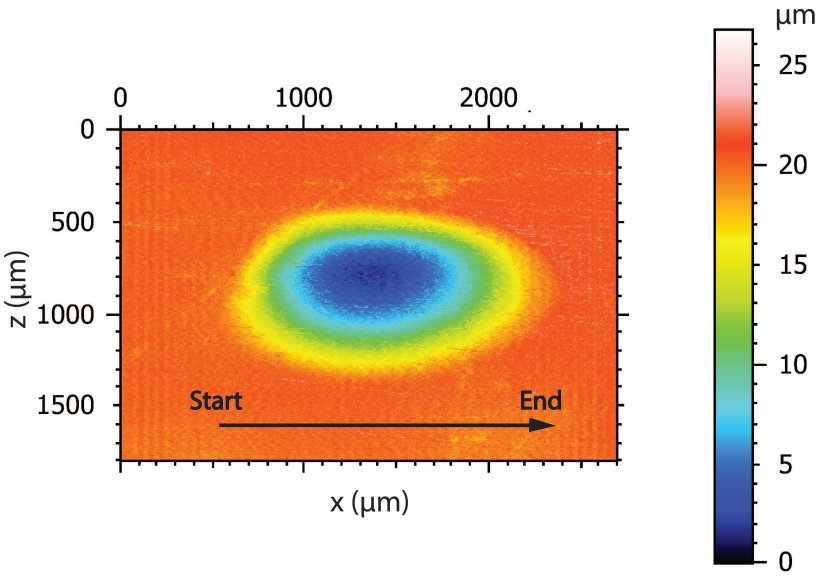

Figure 5.4: Deformation patterns, $\theta = 20°$.

The normal permanent deformation and the sliding length are measured using the scans of the deformed areas (Fig. 5.4). In Fig.5.4 the sliding direction is from left to the right, the profile is wider at the center and sharper at the end of the impact. The profile is approximately elliptical and symmetrical around the x axis. From the profile it can be seen that sliding was ongoing throughout the impact. The normal permanent deformation and the sliding length are approximately $\delta_p = 22$ μm and $L_s = 1400$ μm respectively.

For initial impact angle $\theta_i = 45°$ the initial velocity is $\vec{v}_i = -2.18\hat{j}$ m/s, the normal rebound velocity of the tip of the rod is $v_{fT} = 1.08$ m/s and coefficient of restitution is $e = 0.49$. The average coefficient of friction is measured from the experiments by using Eq. 5.13 $\mu = 0.13$.

The deformation pattern for this case compare to previous case with $\theta = 20°$ shows a deeper deformation at the start of the impact and sharper pattern at the end. Same as the previous case, from the profile, Fig. 5.5, it can be seen that the rod was sliding throughout the impact. The normal permanent deformation and the sliding length are measured as, $\delta_p = 26$ μm and $L_s = 1650$ μm respectively using the profilometer.

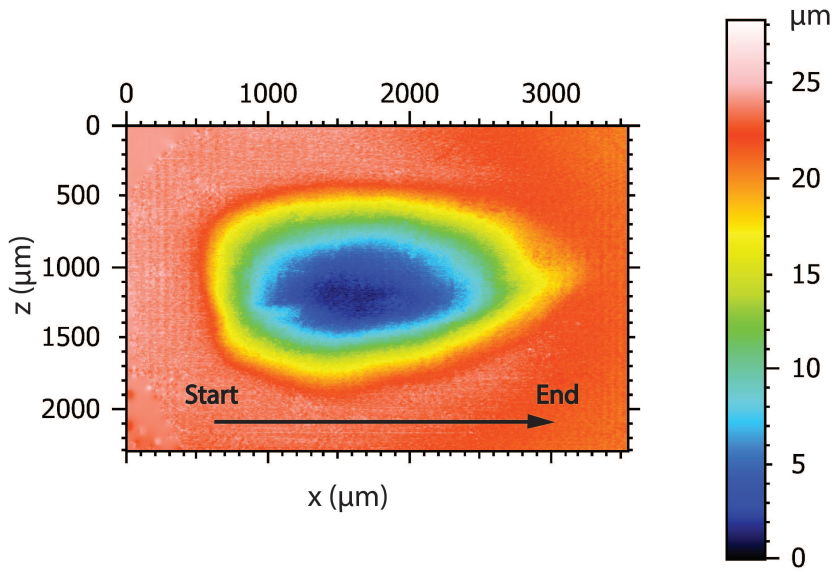

Figure 5.5: Deformation patterns, $\theta = 45°$.

Same measurements have been done for an impact with initial angle, $\theta_i = 70°$. The initial velocity is, $\vec{v}_i = -3.45\ \jmath$ m/s, the normal rebound velocity of the tip of the rod is $v_{fT} = 0.19$ m/s and the coefficient of restitution is $e = 0.05$. The coefficient of friction is measured from the experiment, $\mu = 0.10$.

For this case the scanned profile, Fig. 5.6 of the deformed area shows different trend from the previous cases. In this case the maximum normal permanent deformation happens closer to the end of the impact. The profile shows sliding at the beginning of the impact and sticking or rolling at the end, which developed considerable pile-up in front of the deformation region. The normal permanent deformation and the sliding length are, $\delta_p = 105$ μm and $L_s = 200$ μm respectively (Fig.5.6).

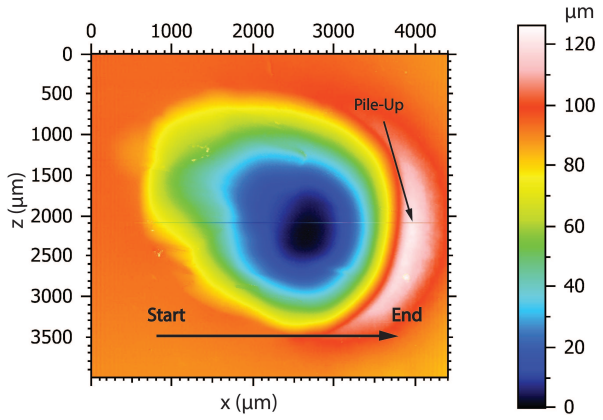

Figure 5.6: Deformation patterns, $\theta = 70°$.

Numerical Solutions

The deformation patterns after the impact has been also calculated by the numerical solutions. Figure 5.7 shows the deformation patterns for the same case as presented in the experimental results with impact angle $\theta = 20°$. The plot shown in Fig. 5.7 is predicted by Ghaednia et al. [34]. As it can be seen, the predictions show circular deformation patters. The predicted patter stays the same for different impact angles and different contact models, this is why only one plot has been provided for the numerical solutions.

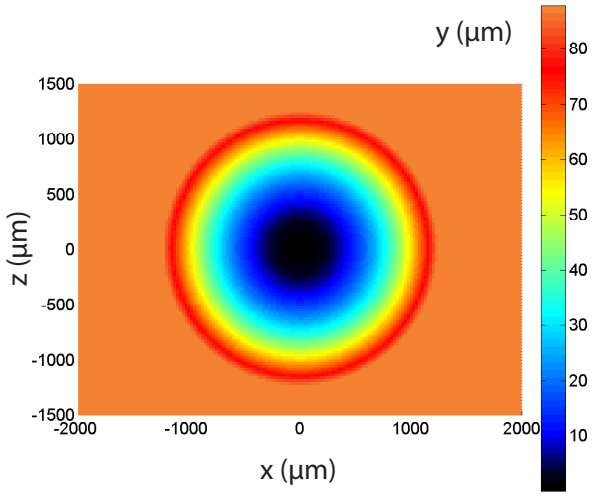

Figure 5.7: Numerical solution for the deformation pattern, $\theta = 20°$.

5.3.2 Average Force and Impact Duration

The main out come of the presented analytical solution is calculating the average force and impact duration using the experimental results for coefficient of restitution and the permanent deformations. Using the results from the experiments and Eq. (5.11), one can calculated the impact duration. By using the calculated impact duration in the following equation (Eq. (5.14)) the average force can be calculated:

$$\int_0^T F dt = \bar{F}T = m(v_{Cf} - v_{Ci}).\hat{j} \tag{5.14}$$

Table. 5.2-5.4 show the comparison between numerical solutions, experimental results and analytical approach for the normal permanent deformation, sliding length, coefficient of restitution, impact duration and average force.

For a drop with impact angle, $\theta = 20°$ and $\vec{v}_i = -1.41\hat{j}$ (the deformation pattern for this case is shown in Fig.5.4) by using the measured coefficient of restitution, permanent deformation and sliding length along with Eq. (5.12),(5.14) the average contact force and impact duration can be calculated. Table. 5.2 show the results for impact duration and average force from experiments and analytical solution.

For the same case, the numerical solution Ghaednia et al. yields to, $e = 0.42$, $\delta_p = -67$ μm, $L_s = -74$ μm, $T = 0.256$ ms and $\bar{F} = 2153$ N. Brake's model shows $e = 0.46$, $\delta_p = -77$ μm, $L_s = -74$ μm, $-T = 0.256$ ms and $\bar{F} = 2153$ N and Kogut-Komvopoulos model predicts $e = 0.43$, $\delta_p = -64$ μm, $L_s = -64$ μm, $T = 0.25$ ms and $\bar{F} = 2568$ N. The results predicted from all of the numerical solution are in a same order of magnitude and approximately the same. Compare to the experimental results it can be seen that the predictions from the numerical solutions for the coefficient of restitution are matching; however, for the impact duration and the average contact force there is a great difference between predictions and the experiments.

Table 5.2: Comparison table for $\theta = 20°$ between experiments Eq. (5.11),(5.14) and numerical simulation results.

	θ_i (deg)	δ_p (μm)	L_s (μm)	e	T (ms)	$\bar{F}$ (N)
Experiments and Eqs. (5.11,5.14)	20	-22	-1400	0.50	4.30	79
Ghaednia et al. [37]	20	-67	-74	0.42	0.25	2571
Brake [14]	20	-77	-75	0.46	0.29	2153
Kogut-Komvopoulos [71]	20	-64	-64	0.43	0.25	2568

Same calculation and numerical solutions have been done for the impact angle $\theta = 45°$. The results from the experiments, analytical solutions and numerical solutions are shown in table. 5.3. Same as previous case with $\theta = 20$ the results for impact duration and average force from the numerical solutions show a great difference comparing to the experiments, even though for the coefficient of restitution, results match the experiments.

For impact angle, $\theta = 70°$ there is contradiction with previous cases with $\theta = 20°,\ 45°$ coefficient of restitution is significantly smaller and impact duration is smaller. Moreover comparing the experiments to the numerical solutions, the normal permanent deformation and the sliding length are of a same order of magnitude however the difference is still significant. For the impact duration and the average force numerical solutions are showing closer results to the experiments.

Table 5.3: Comparison table for $\theta = 45°$ between experiments Eq. (5.11),(5.14) and numerical simulation results.

	θ_i (deg)	δ_p (μm)	L_s (μm)	e	T (ms)	$\bar{F}$ (N)
Experiments and Eqs. (5.11,5.14)	45	-26	-1650	0.49	1.40	595
Ghaednia et al. [37]	45	-67	-74	0.41	0.30	5041
Brake [14]	45	-150	-370	0.41	0.36	4178
Kogut-Komvopoulos [71]	45	-120	-638	0.43	0.30	4805

Table 5.4: Comparison table for $\theta = 70°$ between experiments Eq. (5.11),(5.14) and numerical simulation results.

	θ_i (deg)	δ_p (μm)	L_s (μm)	e	T (ms)	$\bar{F}$ (N)
Experiments and Eqs. (5.11,5.14)	70	-105	-200	0.05	0.10	17672
Ghaednia et al. [37]	70	-251	-544	0.41	0.32	11009
Brake [14]	70	-321	-710	0.36	0.49	9122
Kogut-Komvopoulos [71]	70	-254	-568	0.43	0.40	10029

One should Consider that all of the numerical solutions that have been mentioned here have been validated for normal impacts. Here we are showing that using the contact models for an oblique impact might yield to significant differences in terms of deformations even though that the coefficient of restitution matches. We also provide a solution which is a combination of experiments and analytical solutions to calculate the average contact force and impact duration.

5.3.3 Comparison and Discussion

Sliding length, impact duration and the average impact force are shown to be significantly different from the numerical predictions. One should consider that same numerical simulation has been proven to match the experimental results for coefficient of restitution and the permanent deformation for normal impacts. For smaller angles, $\theta_i = 20°,\ \theta_i = 45°$ numerical simulations and the experimental results match for the coefficient of restitution, but experiments are showing significantly larger values for the sliding length and impact

duration. Experiments also show significantly smaller values for the average impact force. For the larger angles, $\theta_i = 70^\circ$ the comparison is reversed. The deformation patterns predicted by the numerical simulations and measured by the experiments are closer (still not matching); however, the coefficient of restitution is significantly smaller in the experiments. It is interesting that in this case the average impact force is larger and the impact duration is smaller for the experiments which is different from what could be seen for smaller impact angles. A possible reason for this phenomena might be the existence of a relatively large pileup (see Fig. 5.6) in front of the tip of the rod. The pileup can significantly increase the tangential force and therefore decrease the velocity of the tip of the rod.

The reasons behind the difference in the sliding length can be seen in the presented theory (Eq. (5.11)). In Eq. (5.11), α is a positive constant, δ_p and v_i are negative, and T is positive. Therefore the only way for sliding length to increase will be to increase the impact duration. Using Eq. (5.14) for a same coefficient of restitution if the impact duration increases the average impact force should decrease. This shows that the initial condition of the collision specially the impact angle significantly affects the contact force. Therefore considering the force during impact to follow the well-known quasi static contact models for an oblique impact case is not accurate. The experimental results show that the average impact force and the impact duration are significantly different from what we predict with the numerical simulations.

5.4 Conclusion

In this study a new formulation for predicting the mechanics of the oblique impact of a rod with a flat presented. The formulation relates the deformation patterns after the impact to the velocity before the impact, impact duration and the average contact force. It has been shown that the impact duration and the average impact force during the impact can be calculated by measuring the normal permanent deformation, sliding length, velocity before the impact and the coefficient of friction.

Experiments have been performed to measure the velocities before and after the impact and the permanent deformations after the impact. Numerical results have been implemented with a recently developed contact force expression for normal impacts from our previous work. It has been shown that although the numerical simulations are in a good agreement with the experiments for the normal impact, for the oblique impact of a same rod and flat, the results are significantly different from the experimental measurements. The comparison between the experiments and the numerical simulations show that for small impact angles the coefficient of restitution match; however, the deformation patterns are significantly different. This shows the history of the contact force during the impact affects the deformation patterns more than the impulse during the impact.

Finally we showed that our current theories and models of impact problems are not accurate to predict the mechanics behind oblique impact, and further studies in this matter are required. Study of the deformations after the impact can reveal the interaction between the normal and tangential forces during the impact

Chapter 6

Conclusion and contributions

This study was an effort to relate the permanent plastic deformations after collision of metals to the motion of the objects during the collision. To the best of our knowledge this idea is the first of it's kind and we have shown that it can be very useful in understanding the nature of the contact forces during the dynamic loading of elastic-plastic materials both for normal and tangential forces. In this work we study the phenomena in few steps. First we studied the contact force between two deformable objects for a quasi static contact. Second we study the permanent deformation after the normal collision of a round end rod, and compared our predictions with experimental results. Third we expanded the idea for oblique impact of a round end rod with an elastic-plastic flat. We showed that even though the numerical simulations are showing acceptable in predicting the motion of the objects, they do not agree with the experimental results when compared to the plastic deformations. Finally we proposed a new semi analytical semi experimental method that can be used to find the impact duration and average contact force during collision with a better accuracy.

To formulate the contact force, we modeled the contact of a hemisphere with a flat using finite element analysis. Both of the materials were considered elastic-plastic, this was for the first time in field that the deformation on both of the contacting objects was being analyzed simultaneously. We showed the transition from the flattening to indentation contact, and defined a new parameter to, yield strength ratio, to analyze this transition. A comprehensive formulation was developed in order to predict the contact parameters. The predictions showed excellent match with the numerical experiments (FE analysis).

In the next step we used the same contact formulation for the normal impact of a round end rod with an elastic-plastic flat. The equations of motion of the rod during the collision

have been solved numerically using the nonlinear contact force formulation for the compression phase. For the restitution phase we used out experimental profilometeries of the plastic deformation after the collision in order to verify that including the permanent deformations into the numerical solution will yield to better accuracy of the numerical predictions. The work was verified with experimental results in terms of coefficient of restitution.

In the third step the same idea was implemented for the oblique impact of a round end rod and a flat. To only focus on the permanent deformations in normal direction, we used the average coefficient of friction, or traction, measured from the motion measurements in our experiments. Nine different contact models have used to predict the motion and the permanent deformation during the collision, including our proposed model in previous studies. We showed that our models were showing better match with the experiments compare to the other models. However all of the models including ours were showing significantly different results for permanent deformation, which was not ever seen or analyzed before.

Finally we proposed a semi-analytical, semi-experimental method that predicts the impact duration and average normal contact force. We solved the momentum equations during he collision for displacements to relate the displacement in normal and tangential direction to the normal impulse. We assumed that the objects slide throughout the collision with the average coefficient of friction measured from the experiments. Our results show much smaller values for the contact force and significantly larger values for the impact duration. The method we proposed is simple and can be easily used for any application.

Bibliography

[1] G. G. Adams and M. Nosonovsky. Contact modelingforces. *Tribology International*, 33(5):431–442, 2000.

[2] J. Alcalá and D. Esqué-de los Ojos. Reassessing spherical indentation: Contact regimes and mechanical property extractions. *International Journal of Solids and Structures*, 47(20):2714–2732, 2010.

[3] J. Alcala, A. E. Giannakopoulos, and S. Suresh. Continuous measurements of load-penetration curves with spherical microindenters and the estimation of mechanical properties. *Journal of Materials Research*, 13(05):1390–1400, 1998.

[4] J. R. Barber and M. Ciavarella. Contact mechanics. *International Journal of solids and structures*, 37(1):29–43, 2000.

[5] O. Bartier, X. Hernot, and G. Mauvoisin. Theoretical and experimental analysis of contact radius for spherical indentation. *Mechanics of Materials*, 42(6):640–656, 2010.

[6] B. Bhushan. Contact mechanics of rough surfaces in tribology: Single asperity contact. *Applied mechanics reviews*, 49:275–298, 1996.

[7] B. Bhushan. Contact mechanics of rough surfaces in tribology: multiple asperity contact. *Tribology letters*, 4(1):1–35, 1998.

[8] S. Biwa and B. Storåkers. An analysis of fully plastic brinell indentation. *Journal of the Mechanics and Physics of Solids*, 43(8):1303–1333, 1995.

[9] R. M. Brach. Friction, restitution, and energy loss in planar collisions. *Journal of applied mechanics*, 51(1):164–170, 1984.

[10] R. M. Brach. A review of impact models for vehicle collision. Technical report, SAE Technical Paper, 1987.

[11] R. M. Brach. Classical planar impact theory and the tip impact of a slender rod. *international journal of impact engineering*, 13(1):21–33, 1993.

[12] R. M. Brach. *Mechanical impact dynamics: rigid body collisions*. Brach Engineering, LLC, 2007.

[13] M. R. Brake. An analytical elastic-perfectly plastic contact model. *International Journal of Solids and Structures*, 49(22):3129–3141, 2012.

[14] M. R. Brake. An analytical elastic plastic contact model with strain hardening and frictional effects for normal and oblique impacts. *International Journal of Solids and Structures*, 62:104–123, 2015.

[15] J. A. Brinell. Way of determining the hardness of bodies and some applications of the same. *Teknisk Tidskrift*, 5:69, 1900.

[16] V. Brizmer, Y. Zait, Y. Kligerman, and I. Etsion. The effect of contact conditions and material properties on elastic-plastic spherical contact. *Journal of Mechanics of Materials and Structures*, 1(5):865–879, 2006.

[17] H. Brody. That's how the ball bounces. *Physics Teacher*, 22(8):494–97, 1984.

[18] W. R. Chang, I. Etsion, and D. B. Bogy. An elastic-plastic model for the contact of rough surfaces. *Journal of tribology*, 109(2):257–263, 1987.

[19] M. Ciavarella, Y. Xu, and R. L. Jackson. Some closed form results for adhesive rough contacts near complete contact on loading and unloading in the jkr regime. *Journal of Tribology*.

[20] R. Cross. Dynamic properties of tennis balls. *Sports Engineering*, 2:23–34, 1999.

[21] R. Cross. Dynamic properties of tennis balls. *Sports Engineering*, 2:23–34, 1999.

[22] R. Cross. Grip-slip behavior of a bouncing ball. *American Journal of Physics*, 70(11):1093–1102, 2002.

[23] R. Cross. Measurements of the horizontal coefficient of restitution for a superball and a tennis ball. *American Journal of Physics*, 70(5):482–489, 2002.

[24] R. Cross. Oblique impact of a tennis ball on the strings of a tennis racket. *Sports Engineering*, 6(4):235–254, 2003.

[25] R. Cross. Enhancing the bounce of a ball. *The Physics Teacher*, 48(7):450–452, 2010.

[26] R. Cross. Impact behavior of a superball. *American Journal of Physics*, 83(3):238–248, 2015.

[27] R. J. Dignall and S. J. Haake. Analytical modelling of the impact of tennis balls on court surface. In *Tennis science and technology conference*, pages 155–162. Blackwell, 2000.

[28] I. Etsion, Y. Kligerman, and Y. Kadin. Unloading of an elastic–plastic loaded spherical contact. *International Journal of Solids and Structures*, 42(13):3716–3729, 2005.

[29] P. S. Follansbee and G. B. Sinclair. Quasi-static normal indentation of an elasto-plastic half-space by a rigid spherei: Analysis. *International journal of solids and structures*, 20(1):81–91, 1984.

[30] R. Garwin. Kinematics of an ultraelastic rough ball. *American Journal of Physics*, 37(1):88–92, 1969.

[31] H. Ghaednia, O. Cermik, and D. B. Marghitu. Experimental and theoretical study of the oblique impact of a tennis ball with a racket. *Proceedings of the Institution of Mechanical Engineers, Part P: Journal of Sports Engineering and Technology*, 229(3):149–158, 2015.

[32] H. Ghaednia and R. L. Jackson. The effect of nanoparticles on the real area of contact, friction, and wear. *Journal of Tribology*, 135(4):041603, 2013.

[33] H. Ghaednia, R. L. Jackson, and J. M. Khodadadi. Experimental analysis of stable cuo nanoparticle enhanced lubricants. *Journal of Experimental Nanoscience*, 10(1):1–18, 2015.

[34] H. Ghaednia and D. B. Marghitu. Permanent deformation during the oblique impact with friction. *Archive of Applied Mechanics*, 86(1-2):121–134, 2016.

[35] H. Ghaednia, D. B. Marghitu, and R. L. Jackson. Predicting the permanent deformation after the impact of a rod with a flat surface. *Journal of Tribology*, 137(1):011403, 2015.

[36] H. Ghaednia and A. Ohadi. Vibration behavior of flexible rotor system mounted on mr squeeze film damper with thermal growth effect. *Journal of Vibration and Acoustics*, 134(1):011015, 2012.

[37] H. Ghaednia, S. A. Pope, R. L. Jackson, and D. B. Marghitu. A comprehensive study of the elasto-plastic contact of a sphere and a flat. *Tribology International*, 93:78–90, 2016.

[38] H. Ghaednia, A. Rostami, and R. L. Jackson. The influence of thermal expansion and plastic deformation on a thermo-electro mechanical spherical asperity contact. In *Electrical Contacts (Holm), 2012 IEEE 58th Holm Conference on*, pages 1–7. IEEE, 2012.

[39] H. Gheadnia, O. Cermik, and D. B. Marghitu. Experimental and theoretical analysis of the elasto-plastic oblique impact of a rod with a flat. *International Journal of Impact Engineering*, 86:307–317, 2015.

[40] W. Goldsmith. *Impact*. Courier Corporation, 2001.

[41] A. Golgoon, S. Sadik, and A. Yavari. Circumferentially-symmetric finite eigenstrains in incompressible isotropic nonlinear elastic wedges. *International Journal of Non-Linear Mechanics*, 84:116–129, 2016.

[42] A. Golgoon and A. Yavari. Nonlinear elastic inclusions in anisotropic solids. *Journal of Elasticity*, pages 1–31, 2017.

[43] A. Golgoon and A. Yavari. On the stress field of a nonlinear elastic solid torus with a toroidal inclusion. *Journal of Elasticity*, pages 1–31, 2017.

[44] S. R. Goodwill, R. Kirk, and S. J. Haake. Experimental and finite element analysis of a tennis ball impact on a rigid surface. *Sports engineering*, 8(3):145–158, 2005.

[45] I. Green. Poisson ratio effects and critical valus in spherical and cylindrical hertzian contacts. *APPLIED MECHANICS AND ENGINEERING*, 10(3):451, 2005.

[46] S. J. Haake, M. J. Carre, and S. R. Goodwill. The dynamic impact characteristics of tennis balls with tennis rackets. *Journal of sports sciences*, 21(10):839–850, 2003.

[47] C. Hardy, C. N. Baronet, and G. V. Tordion. The elasto-plastic indentation of a half-space by a rigid sphere. *International Journal for numerical methods in engineering*, 3(4):451–462, 1971.

[48] C. Hertz. Über die berührung fester elastischer körper (on the contact of elastic solids). *Journal fur die Reine und Andegwandte Mathematik*, 92:156–171, 1882.

[49] I. M. Hutchings. The contributions of david tabor to the science of indentation hardness. *Journal of Materials Research*, 24(03):581–589, 2009.

[50] A. J. Ishlinsky. The problem of plasticity with the axial symmetry and brinell's test. *Prikl. Mat. Mekh*, 8:201–224, 1944.

[51] R. L. Jackson, I. Chusoipin, and I. Green. A finite element study of the residual stress and strain formation in spherical contacts. *ASME Journal of Tribology*, 60(3):217–229, 2010.

[52] R. L. Jackson, H. Ghaednia, H. Lee, A. Rostami, and X. Wang. Contact mechanics. In *Tribology for Scientists and Engineers*, pages 93–140. Springer, 2013.

[53] R. L. Jackson, H. Ghaednia, and S. A. Pope. A solution of rigid perfectly plastic deep spherical indentation based on slip line theory. *Submitted to Tribology Letter*.

[54] R. L. Jackson and I. Green. A finite element study of elasto-plastic hemispherical contact against a rigid flat. *ASME Journal of Tribology*, 127(2):343–354, 2005.

[55] R. L. Jackson and I. Green. A finite element study of elasto-plastic hemispherical contact against a rigid flat. *Transactions of the ASME-F-Journal of Tribology*, 127(2):343–354, 2005.

[56] R. L. Jackson and I. Green. A statistical model of elasto-plastic asperity contact between rough surfaces. *Tribology International*, 39(9):906–914, 2006.

[57] R. L. Jackson, I. Green, and D. B. Marghitu. Predicting the coefficient of restitution impacting elastic-perfectly plastic spheres. *Journal of Nonlinear Dynamics*, 60(3):217–229, 2010.

[58] R. L. Jackson and L. Kogut. A comparison of flattening and indentation approaches for contact mechanics modeling of single asperity contacts. *Journal of tribology*, 128(1):209–212, 2006.

[59] R. L. Jackson, V. W. Krithivasan, and Everett W. The pressure to cause complete contact between elasticplastic sinusoidal surfaces. *Proceedings of the Institution of Mechanical Engineers, Part J: Journal of Engineering Tribology*, 222(7):857–863, 2008.

[60] R. L. Jackson, D. B. Marghitu, and I. Green. Predicting the coefficient of restitution of impacting elastic-perfectly plastic spheres. In *STLE/ASME 2006 International Joint Tribology Conference*, pages 1449–1450. American Society of Mechanical Engineers, 2006.

[61] R. L. Jackson, Y. Xu, and M. Mahajan. Fundamentals and previous experiments of the squeeze film levitation mechanism. *Proceedings of the National Academy of Sciences*, 113(45):E6906–E6906, 2016.

[62] K. L. Johnson. Experimental determination of the contact stresses between plastically deformed cylinders and spheres. *Engineering Plasticity, Cambridge University Press. Cambridge*, pages 341–361, 1968.

[63] K. L. Johnson. Contact mechanics. pages 154–179. Cambridge, Cambridge University Press, 1985.

[64] T. R. Kane and D. A. Levinson. *Dynamics, theory and applications.* McGraw Hill, 1985.

[65] K. Kardel. *An analytical and experimental study on 3D-printed custom surfaces for benthic algal biofilms.* PhD thesis, Auburn University, 2016.

[66] K. Kardel, H. Ghaednia, A. L. Carrano, and D. B. Marghitu. Experimental and theoretical modeling of behavior of 3d-printed polymers under collision with a rigid rod. *Additive Manufacturing*, 14:87–94, 2017.

[67] A. H. Kharaz and D. A. Gorham. A study of the recitation coefficient in elasic-plastic impactd. *Philosophical Magazine Letters*, 80(8):549–559, 2000.

[68] A. H. Kharaz, D. A. Gorham, and A. D. Salman. Accurate measurement of particle impact parameters. *Measurement Science Technology*, 10:31, 1999.

[69] L. Kogut and I. Etsion. Elastic-plastic contact analysis of a sphere and a rigid flat. *ASME Journal of Applied Mechanics*, 69(5):657–662, 2002.

[70] L. Kogut and I. Etsion. A semi-analytical solution for the sliding inception of a spherical contact. *Journal of tribology*, 125(3):499–506, 2003.

[71] L. Kogut and K. Komvopoulos. Analysis of the spherical indentation cycle for elastic–perfectly plastic solids. *Journal of materials research*, 19(12):3641–3653, 2004.

[72] K. Komvopoulos. Finite element analysis of a layered elastic solid in normal contact with a rigid surface. *Journal of tribology*, 110(3):477–485, 1988.

[73] K. Komvopoulos. Elastic-plastic finite element analysis of indented layered media. *Journal of Tribology*, 111(3):430–439, 1989.

[74] K. Komvopoulos and N. Ye. Three-dimensional contact analysis of elastic-plastic layered media with fractal surface topographies. *Journal of tribology*, 123(3):632–640, 2001.

[75] L. Y. Li, C. Y. Wu, and C. Thornton. A theoretical model for the contact of elasto-plastic bodies. *Journal of Mechanical Engineering Science*, 216(4):421–431, 2002.

[76] C. Maclaurin. Démonstration des loix du choc des corps. Proposé pour l'année mil sept cens vingt-quatre, Jombert, Paris,, 1724.

[77] D. B. Marghitu, D. Cojocaru, and R. L. Jackson. Elasto-plastic impact of a rotating link with a massive surface. *International Journal of Mechanical Sciences*, 53(4):309–315, 2011.

[78] D. B. Marghitu, D. Cojocaru, and R. L. Jackson. Elasto-plastic impact of a rotating link with a massive surface. *International journal of Mechanical Sciences*, 53:309–315, 2011.

[79] T. Mase and A. M. Kersten. Experimental evaluation of a 3-d hyperelastic, rate-dependent golf ball constitutive model. *The engineering of sport*, 5:238–244, 2004.

[80] M. T. Mason and Y. Wang. On the inconsistency of rigid-body frictional planar mechanics. In *Robotics and Automation, 1988. Proceedings., 1988 IEEE International Conference on*, pages 524–528. IEEE, 1988.

[81] N. Maw, J. R. Barber, and J. N. Fawcett. The oblique impact of elastic spheres. *Wear*, 38(1):101–114, 1976.

[82] S. D. Mesarovic and N. A. Fleck. Spherical indentation of elastic–plastic solids. *Proceedings of the Royal Society of London. Series A: Mathematical, Physical and Engineering Sciences*, 455(1987):2707–2728, 1999.

[83] S. D. Mesarovic, D. J. Sinisa, and K. L Johnson. Adhesive contact of elastic-plastic spheres. *Journal of the mechanics and physics of solids*, 48:2009–2033, 2000.

[84] E. Meyer. Investigations of hardness testing and hardness. *Phys. Z*, 9:66, 1908.

[85] I. Newton. *Philosophiae naturalis principia mathematica*, volume 1. excudit G. Brookman; impensis TT et J. Tegg, Londini, 1833.

[86] E. Olsson and P. L. Larsson. A unified model for the contact behaviour between equal and dissimilar elastic–plastic spherical bodies. *International Journal of Solids and Structures*, 81:23–32, 2016.

[87] S. D. Poisson. Traité de mécaniqu. Paris Courcier, 1811.

[88] D. S. Price, R. Jones, A. R. Harland, and V. V. Silberschmidt. Viscoelasticity of multilayer textile reinforced polymer composites used in soccer balls. *Journal of materials science*, 43(8):2833–2843, 2008.

[89] J. Quicksall, R. L. Jackson, and I. Green. Elasto-plastic hemispherical contact models for various mechanical properties. *Proceedings of the Institution of Mechanical Engineers, Part J: Journal of Engineering Tribology*, 218(4):313–322, 2004.

[90] A. Rezaei, R. Verhelst, W. Van Paepegem, and J. Degrieck. Finite element modelling and experimental study of oblique soccer ball bounce. *Journal of sports sciences*, 29(11):1201–1213, 2011.

[91] O. Richmond, H. L. Morrison, and M. L. Devenpeck. Sphere indentation with application to the brinell hardness test. *International Journal of Mechanical Sciences*, 16(1):75–82, 1974.

[92] J. R. Roberts, R. Jones, and S. J. Rothberg. Measurement of contact time in short duration sports ball impacts: an experimental method and correlation with the perceptions of elite golfers. *Sports Engineering*, 4(4):191–203, 2001.

[93] S. A. Rodriguez, J. Alcala, and R. Martins S. Effects of elastic indenter deformation on spherical instrumented indentation tests: the reduced elastic modulus. *Philosophical Magazine*, 91(7-9):1370–1386, 2011.

[94] S. Saha, Y. Xu, and R. L. Jackson. Perfectly elastic axisymmetric sinusoidal surface asperity contact. *Journal of Tribology*, 138(3):031401, 2016.

[95] P. Sahoo, B. Chatterjee, and D. Adhikary. Finite element based elastic-plastic contact behavior of a sphere against a rigid flat-effect of strain hardening. *Int. J. Engg. and Tech*, 2(1):1–6, 2010.

[96] A. Shamloo, A. Golgoon, and E. Ghaffarzadeh. Role of α and β transmembrane domains in integrin clustering. *Actuators*, 4(4):267–280, 2015.

[97] S. Shankar and M. M. Mayuram. Effect of strain hardening in elastic–plastic transition behavior in a hemisphere in contact with a rigid flat. *International Journal of Solids and Structures*, 45(10):3009–3020, 2008.

[98] G. B. Sinclair, P. S. Follansbee, and K. L. Johnson. Quasi-static normal indentation of an elasto-plastic half-space by a rigid sphereii. results. *International Journal of Solids and Structures*, 21(8):865–888, 1985.

[99] W. J. Stronge. Rigid body collisions with friction. *Proceedings of the Royal Society of London*, A431:169–181, 1990.

[100] W. J. Stronge. Friction in collisions: Resolution of a paradox. *Journal of Applied Physics*, 69(2):610–612, 1991.

[101] W. J. Stronge. Unraveling paradoxical theories for rigid body collisions. *ASME Journal of Applied Mechanics*, 59:681–682, 1991.

[102] W. J. Stronge. Energy dissipated in planar collision. *ASME Journal of Applied Mechanic*, 61:605–611, 1992.

[103] W. J. Stronge. Theoretical coefficient of restitution for planar impact of rough elasto-plastic bodies. *Impact, Waves, and Fracture*, pages 351–362, 1995.

[104] W. J. Stronge. Contact problems for elasto-plastic impact in multi-body systems. In *Impacts in Mechanical Systems*, pages 189–234. Springer, 2000.

[105] D. Tabor. A simple theory of static and dynamic hardness. *Proceedings of the Royal Society of London, Series A*, 192:247–274, 1948.

[106] D. Tabor. The hardness of metals. Clarendon Press, Oxford, UK, 1951.

[107] B. Taljat and G. M. Pharr. Development of pile-up during spherical indentation of elastic–plastic solids. *International Journal of Solids and Structures*, 41(14):3891–3904, 2004.

[108] C. Thornton. Coefficient of restitution for collinear collisions of elastic-perfectly plastic spheres. *ASME Journal of Applied Mechanics*, 65:383–354, 1997.

[109] C. Thornton and Z. Ning. Oblique impact of elasto-plastic spheres. *Proc. 1st int. Particle Technology Forum*, 2:14–19, 1994.

[110] S. Wadwalkar, R. L. Jackson, and L. Kogut. A study of the elasticplastic deformation of heavily deformed spherical contacts. *Proceedings of the Institution of Mechanical Engineers, Part J: Journal of Engineering Tribology*, 224(10):1091–1102, 2010.

[111] H. Wang, X. Yin, Q. Deng, B. Yu, Q. Hao, and X. Dong. Experimental and theoretical analyses of elastic-plastic repeated impacts by considering wave effects. *European Journal of Mechanics-A/Solids*, 65:212–222, 2017.

[112] H. Wang, X. Yin, X. Qi, Q. Deng, B. Yu, and Q. Hao. Experimental and theoretical analysis of the elastic-plastic normal repeated impacts of a sphere on a beam. *International Journal of Solids and Structures*, 2017.

[113] X. Wang, Y. Xu, and R. L. Jackson. Elastic–plastic sinusoidal waviness contact under combined normal and tangential loading. *Tribology Letters*, 65(2):45, 2017.

[114] Z. Q. Wang. A compact and easily accepted continuous model for the elastic-plastic contact of a sphere and a flat. *Journal of Applied Mechanics*, 80(1):014506, 2013.

[115] J. S. Weaver, A. Khosravani, A. Castillo, and S. R. Kalidindi. High throughput exploration of process-property linkages in al-6061 using instrumented spherical microindentation and microstructurally graded samples. *Integrating Materials and Manufacturing Innovation*, 5(1):10, 2016.

[116] C. Wu, L. Y. Li, and C. Thornton. Energy dissipation during normal impact of elastic and elastic-plastic spheres. *International Journal of Impact Engineering*, 32(1):593–604, 2005.

[117] R. L. Xu, Y.and Jackson. Periodic contact problems in plane elasticity-the fracture mechanics approach. *Journal of Tribology*.

[118] Y. Xu and R. L. Jackson. Statistical models of nearly complete elastic rough surface contact-comparison with numerical solutions. *Tribology International*, 105:274–291, 2017.

[119] Y. Xu, R. L. Jackson, and D. B. Marghitu. Statistical model of nearly complete elastic rough surface contact. *International Journal of Solids and Structures*, 51(5):1075–1088, 2014.

[120] Y. Xu, A. Rostami, and R. L. Jackson. Elastic contact between a geometrically anisotropic bisinusoidal surface and a rigid base. *Journal of Tribology*, 137(2):021402, 2015.

[121] Y. Yamada, T. Kawai, N. Yoshimura, and T. Sakurai. Analysis of the elastic-plastic problems by the matrix displacement method. In *Proc. Conf. on Matrix methods in structural mechanics, Wright-Patterson Air Force Base, Ohio (October 1968)*, 1968.

[122] N. Ye and K. Komvopoulos. Indentation analysis of elastic-plastic homogeneous and layered media: Criteria for determining the real material hardness. *Journal of Tribology*, 125(4):685–691, 2003.

[123] W. Yu and J. P. Blanchard. An elastic-plastic indentation model and its solutions. *Journal of Materials Research*, 11(09):2358–2367, 1996.

[124] X. Zhang and R. L. Jackson. An analysis of the multiscale structure of surfaces with various finishes. *Tribology Transactions*, 60(1):121–134, 2017.

[125] X. Zhang, Y. Xu, and R. L. Jackson. An analysis of generated fractal and measured rough surfaces in regards to their multi-scale structure and fractal dimension. *Tribology International*, 105:94–101, 2017.

[126] B. Zhao, F. Shen, Y. Cui, Y. Xie, and K. Zhou. Damage analysis for an elastic-plastic body in cylindrical contact with a rigid plane. *Tribology International*, 2017.

[127] Y. Zhao, D. M. Maietta, and L. Chang. An asperity microcontact model incorporating the transition from elastic deformation to fully plastic flow. *Journal of Tribology*, 122(1):86–93, 2000.

[128] O. C. Zienkiewicz and Y. K. Cheung. *The finite element method in structural and continuum mechanics: numerical solution of problems in structural and continuum mechanics*, volume 1. McGraw-Hill London, New York, 1967.

[129] O. C. Zienkiewicz and P. B. Morice. *The finite element method in engineering science*, volume 1977. McGraw-hill London, 1971.